

A THEORETICAL STUDY ON CATALYTIC STEPS OF
HYDROGEN PRODUCTION AND PURIFICATION

by

Aslıhan Sümer

B.S., Chemical Engineering, Boğaziçi University, 2001

M.S., Chemical Engineering, Boğaziçi University, 2004

Submitted to the Institute for Graduate Studies in
Science and Engineering in partial fulfillment of
the requirements for the degree of
Doctor of Philosophy

Graduate Program in Chemical Engineering

Boğaziçi University

2010

ACKNOWLEDGEMENTS

First, I would like to thank my advisor, Erhan Aksoylu, for giving me the freedom to pursue my own academic interests while still providing his precious time when his guidance is needed. Character traits of him, such as tolerance, humor and patience, are most acknowledged. I am also indebted to my thesis committee: Canan Atılgan, Mahir Arıkol, Zeynep Ilsen Onsan and Ramazan Yıldırım, who reviewed my work on a very short notice and gave insightful comments, and to rest of the Department of Chemical Engineering for their valuable support.

I worked as a research assistant in the office of the rector of Boğaziçi University for 6 years. I especially thank Ayşe Soysal, Gülen Aktaş and Cem Behar, for facilitating my research by granting me total freedom in my work schedule throughout the period I worked with them. It was indeed a privilege. A special thanks to a bunch of nice people from the South Campus: Nilüfer, Sevgi, Tülay, Fadime, Selver, Betül, İpek for their kind friendship, and Şermin Abdullah, for her valuable guidance.

I would like to thank all the people who, in some way or another, contributed to the completion of this thesis. The names of only a few could be stated here, gratitude towards the rest will also be hidden in my heart for the rest of my life.

Finally, I thank my family: my parents, Selcuk and Remziye Sümer, for their unconditional love and support, my brother Selim Sümer, and all the rest of my family, especially Çiğdem Kurdoğlu, Ayla Kurdoğlu, Ülkü Duran, Semra Sayın, all these industrious, strong and kind women, whose presence inspired me to pursue a career in life.

Financial support provided by the Boğaziçi University Research Fund through project 05M109, The Scientific and Technological Research Council of Turkey (TUBITAK) through project 105M282 and Turkish State Planning Organization (DPT) through projects DPT-07K120630 and DPT-03K120250 is gratefully acknowledged.

ABSTRACT

A THEORETICAL STUDY ON CATALYTIC STEPS OF HYDROGEN PRODUCTION AND PURIFICATION

The aim of this thesis is to obtain information on catalytic activity of transition metals used in different steps of hydrogen production and purification. Density functional theory calculations with periodic slabs have been utilized on energetically stable Pt-Sn and Pt-Ni bimetallic alloys, to analyze the electronic structure and reactivity in specific reactions, namely methane oxidative steam reforming (OSR) in the case of Pt-Ni and CO oxidation in the case of Pt-Sn. The studies performed within the framework of the current thesis can be briefly summarized as follows: (i) Oxygen chemisorption on Pt-Ni surface alloy has been studied aiming to shed light on the decreased oxidation tendency of the Ni surface after Pt doping. The results showed that oxygen chemisorption is weakened on surface alloys, compared with monometallic Pt and Ni surfaces and bulk Ni₃Pt alloy. (ii) Methane dehydrogenation is one of the most important steps of OSR mechanism. Methane dehydrogenation reaction was studied on Pt-Ni surface alloy and it was found that methane dehydrogenation proceeds on Pt-sites during OSR. (iii) Experimental studies confirmed that Pt₃Sn is the main active phase of Pt-Sn system supported on nitric acid oxidized activated carbon. The strength of CO adsorption on Pt₃Sn alloy has pronounced effects on the activity and performance stability characteristics of the catalyst. In the current study, CO adsorption on Pt(111) and on Pt₃Sn(111) were analyzed for CO surface coverages ranging between 0-0.5 ML. The effect of CO surface coverage on electronic reconstruction of free sites, extent of adsorbate-adsorbate and adsorbate-surface interactions, and adsorption structure of CO were parametrically studied. It was found that adsorbed CO molecules form clusters on Pt(111) surface, which hinder oxygen chemisorption and prevent CO oxidation reaction. (iv) In the final part of the study, the adsorptive properties of the Pt₃Sn alloy were investigated; here the results of the previous part were extended further to coadsorption of CO and O on Pt₃Sn(111), aiming to analyze the changes in the binding strength of O and CO on the surface led by coadsorption. Electronic structure analysis is performed throughout the calculations to bring an explanation to the results.

ÖZET

HİDROJEN ÜRETİMİ VE SAFLAŞTIRILMASI AŞAMALARINDA KULLANILAN KATALİTİK SİSTEMLERİN KURAMSAL OLARAK İNCELENMESİ

Bu tezin amacı hidrojen üretimi ve saflaştırılması sürecinde kullanılan katalitik tepkimelerin kuantum mekaniksel yöntemler ile incelenmesidir. Hidrokarbonların oksijenli ortamda buhar reformasyonunda kullanılan Pt-Ni ve karbonmonoksitin yakılmasında kullanılan Pt-Sn alaşımları incelenmiştir. Özet olarak bu sistemler üzerinde şu çalışmalar gerçekleştirildi: (i) Pt-Ni yüzey alaşımları üzerinde oksijen adsorpsiyon kuvvetleri incelenmiş ve sonuçlar Pt, Ni ve Ni₃Pt alaşımı için bulunan sonuçlar ile kıyaslanmıştır. Oksijen adsorpsiyonunun yüzey alaşımları üzerindeki kuvvetinin diğer metal ve alaşımlar üzerindeki kıyasla daha düşük olduğu bulundu. Sonuçlar, Pt-Ni yüzey alaşımlarının hidrokarbon reformasyonunda oksijen gazı altında oksitlenme özelliklerinin daha düşük olduğunu desteklemektedir. (ii) Pt-Ni yüzey alaşımı üzerinde metan reformasyon tepkimesi incelendi. Sonuçlar, tepkimenin tercihen yüzeyde Pt merkezleri üzerinde gerçekleştiğini göstermektedir. (iii) Deneysel çalışmalar, aktif karbon üzerinde nitrik asit oksidasyonu ile elde edilen Pt₃Sn alaşımının karbonmonoksit oksidasyonu sırasında etkin bir merkez oluşturduğunu göstermektedir. Tepkime sırasında karbonmonoksitin bağlanma gücü ve şeklinin tepkimenin hızı açısından büyük öneme sahip olduğu bilinmektedir. Bu sebepten bu çalışmada, Pt(111) ve Pt₃Sn(111) yüzeyleri üzerinde karbonmonoksit bağlanması incelenmiştir. Sonuçlar, Pt(111) üzerinde bağlanmış karbonmonoksit moleküllerinin kümeler oluşturduğunu, bunların oksijen adsorpsiyonunu engelleyerek reaksiyonu yavaşlattığını göstermektedir. (iv) Son olarak, bir önceki çalışmanın devamı olarak Pt₃Sn alaşımı üzerinde karbonmonoksit ve oksijen eşzamanlı adsorpsiyonuna bakılarak, oksijen ve karbonmonoksit arasındaki etkileşimlerin bağlanma kuvveti üzerindeki etkileri incelenmiştir.

TABLE OF CONTENTS

ACKNOWLEDGEMENTS.....	iii
ABSTRACT.....	iv
ÖZET.....	v
TABLE OF CONTENTS	vi
LIST OF FIGURES.....	ix
LIST OF TABLES	xv
LIST OF SYMBOLS/ABBREVIATIONS.....	xvii
1. INTRODUCTION.....	1
2. LITERATURE SURVEY.....	7
2.1. Catalytic Hydrogen Production from Hydrocarbon Fuels	7
2.1.1. Hydrogen as an Energy Source.....	7
2.1.2. Fuel Processors	9
2.2. Catalytically Active Bimetallic Alloys: General Information.....	16
2.2.1. Electronic Properties of Bimetallic Catalysts and Their Effect on Surface Stability, Adsorption and Reactivity.....	19
2.2.2. Electronic Reconstruction during Alloying.....	20
2.2.3. Adsorption versus Surface Stress.....	21
3. METHODOLOGY	27
3.1. Theory behind Computational Methods: Quantum Chemical Models.....	27
3.1.1. Schrödinger Equation.....	28
3.1.2. Many-body Problem.....	29
3.1.3. Born-Oppenheimer Approximation	29
3.1.4. Electron-electron Interactions.....	30
3.1.5. Density Functional Models.....	31
3.1.6. Periodic Supercells.....	34
3.1.7. Bloch's Theorem.....	35
3.1.8. Plane-Wave Basis Set.....	35
3.1.9. Electron-Ion Interactions (Pseudopotential Theory).....	37
3.2. Materials Studio Software.....	38
3.2.1. MS Visualizer	38

3.2.2. MS CASTEP	40
3.2.3. MS DMol3	40
3.3. Parameters for Optimization	44
3.4. Calculating the Properties	45
3.4.1. LDOS Charts	45
3.4.2. Mulliken Charges	45
4. RESULTS AND DISCUSSION	47
4.1. Effect of Pt Incorporation on the Electronic and Oxygen Chemisorption	
Properties of Ni Surface	47
4.1.1. Computational Parameters	48
4.1.2. Pt-Ni Surface Alloy Formation and the Electronic Reconstruction at the	
Surface due to Pt-Ni Interaction	49
4.1.3. Structure of Stable Surface Alloys	52
4.1.4. Oxygen Adsorption	56
4.1.5. Stress-induced Oxygen Adsorption	61
4.1.6. Summary	63
4.2. Oxidative Steam Reforming Reaction on Pt-Ni Surface Alloy: A Comparison	
with Monometallic Ni	64
4.2.1. Computational Parameters	64
4.2.2. Pt-Ni Surface Alloy Formation	65
4.2.3. Adsorption of Reactants and Products	68
4.2.4. Dehydrogenation of Methane	72
4.2.5. Summary	75
4.3. Adsorption Induced Surface Electronic Reconstruction of Pt and Pt-Sn Alloys	
During CO Adsorption	75
4.3.1. Computational Parameters	77
4.3.2. CO Adsorption on Pt(111)	78
4.3.3. CO Adsorption on Pt ₃ Sn(111)	85
4.3.4. Summary	88
4.4. CO and O Coadsorption on Pt ₃ Sn: Changes in the Adsorptive Properties of the	
Surface with Alloying and Coverage	89
4.4.1. Computational Parameters	91
4.4.2. Adsorption of CO and O	92

4.4.3. Coadsorption of CO+O	97
4.4.4. Effect of Surface Coverage on Coadsorption	100
4.4.5. Summary.....	103
5. CONCLUSIONS AND RECOMMENDATIONS.....	105
5.1. Conclusions	105
5.2. Recommendations	107
APPENDIX A: TRANSITION STATE SEARCH FOR CH ₄ DEHYDROGENATION	110
APPENDIX B: RELATIVISTIC EFFECTS ON CO ADSORPTION.....	113
REFERENCES.....	115

LIST OF FIGURES

Figure 1.1. Designing efficient bimetallic catalysts	4
Figure 2.1. Fuel processors.....	10
Figure 2.2. Types of bimetallics	17
Figure 2.3. Electronic distribution at the valance states of Ni, Pt and Sn.....	19
Figure 2.4. Bimetallic alloy surface formed by diffusion at the metal-metal interfaces. If the two metals have similar electronic structures, then their mixing mainly causes a strain effect due to the difference in their atomic sizes.	20
Figure 2.5. Changes in Pd and Cu valance band during alloy formation (d-band only). The top panel corresponds to pure metals; central panel correspond to bulk alloys; bottom panel surface alloys. Solid lines stand for Pd atoms and dashed lines for Cu atoms. Thick lines represent surface atoms and thin lines bulk atoms [58].	22
Figure 2.6. Simplified rectangular model to define the changes in the structure of the d-band of Pt atoms that are under the effect of strain	25
Figure 3.1. The Pt_3Sn unit cell. Dark and light balls represent Sn and Pt, respectively.....	38
Figure 3.2. (a) Cleaving a Pt unit cell in (111) direction (b) Top view of $Pt_3Sn(111)$ surface after cleaving. Dark and light balls represent Sn and Pt, respectively.....	39
Figure 3.3. Three dimensional slab after creating the vacuum above the surface. The sysytem is composed of repeating units in x,y and z dimensions. Thus,	

the vacuum should be thick enough to prevent interactions with the repeating cell in z-direction.	40
Figure 3.4. Adsorption sites: three-fold, bridge and linear from left to right.....	41
Figure 3.5. A sample energy curve obtained after LST/QST algorithm.	43
Figure 4.1. Ni-Pt atom exchange. Ni surface atom is substituted by (a) the Pt adatom adsorbed on the Ni substrate (b) one of the Pt atoms from the Pt cluster on the Ni substrate. The energy of Pt-Ni atom exchange is also given. Dark balls represent Pt, gray ones represent Ni atoms.....	50
Figure 4.2. Schematic presentation of alloy formation steps. Dark balls represent Pt, gray ones represent Ni atoms.....	51
Figure 4.3. Surface energy (E_{surf}) and stress (in absolute value) changes: Pt concentration at layer I (topmost surface layer) increases from 0 (monometallic Ni surface) to 100 per cent (pseudomorphic Pt layer over Ni).	54
Figure 4.4. Pt protrusion from Ni(111) surface. Dark balls represent Pt, gray ones represent Ni atoms.....	56
Figure 4.5. LDOS at (a) surface Pt atom (b) surface Ni atom. Surface structures are monometallic Ni(111), monometallic Pt(111), and Pt-Ni surface alloys with Pt concentration at the topmost layer ranging from 25 to 75 per cent.	58
Figure 4.6. Possible oxygen chemisorption sites formed after Pt deposition onto Ni substrate: Pt cluster over Ni, pure Ni site near Pt neighbors, Pt-Ni mixed site, site with Pt atoms in second layer. Dark balls represent Pt, gray ones represent Ni atoms.....	60

Figure 4.7. The change in oxygen chemisorption energy with the total charge transferred from metal surface to O atom (q). Adsorbate surfaces are monometallic Ni(111), monometallic Pt(111), bulk Ni ₃ Pt alloy, and Pt-Ni surface alloys (SA) with Pt concentration at the topmost layer ranging from 25 to 100 per cent.....	62
Figure 4.8. LDOS at surface Pt and Ni atoms of Pt-Ni surface alloy. Calculations are performed with two different basis sets: (i) including relativistic effects (AER) and (ii) excluding relativistic effects (AE).....	68
Figure 4.9. LDOS at C of CH ₃ molecule adsorbed on Pt-Ni surface alloy and Ni(111). Calculations are performed with two different basis sets: (i) including relativistic effects (AER) and excluding relativistic effects (AE). Calculations for Ni(111) are performed only with AER.	71
Figure 4.10. Reaction pathway for CH ₄ dehydrogenation, initial adsorption state, transition state and the product in series from left to right, on (a) Ni(111) (b) 11%Pt-Ni(111)	74
Figure 4.11. Ball model of Pt(111) and various CO adsorption sites available on the surface. Gray balls represent Pt. Sites are labeled as T(atop), B _{Pt} (bridge), H _{hcp} (hollow hcp) and H _{fcc} (hollow fcc).	79
Figure 4.12. CO at (a) 0.11 ML, (b) 0.25 ML - p(2x2) and (c) 0.33 ML - ($\sqrt{3}\times\sqrt{3}$)R30° LEED pattern.....	81
Figure 4.13. Changes in LDOS with coverage increasing from 0.11 to 0.33 ML at (a) CO-coordinated Pt atom (b) C of adsorbed CO molecule (c) bare Pt atoms at the topmost surface layer which are neighbors of adsorption site. Pt-close and Pt-far denote the first and second nearest neighbors, respectively, at 0.11 ML.....	82
Figure 4.14. Shift of metal LDOS at bare surface Pt atoms to lower values as a result of CO adsorption at 0.11 ML.....	83

Figure 4.15. CO at 0.5 ML with (a) T-B structure at c(4x2) cell (b) T-H _{fcc} structure at c(4x2) cell (CO diffuses from site B to H _{fcc}) (c) T-B structure at p(2x2) cell (d) T-T structure at p(2x2) cell.....	84
Figure 4.16. LDOS at C atom at 0.25 ML and 0.5 ML with CO adsorbed only linearly and half-linear and half- bridge type (T-B)	85
Figure 4.17. Ball model of Pt ₃ Sn(111) and stable CO adsorption sites on the surface. Bigger grey and blue balls represent Sn and Pt, respectively. Sites are labeled as T(atop), B _{Pt} (bridge on Pt), B _{Sn} (bridge on Sn), H _{hcp} (hollow hcp) and H _{fcc} (hollow fcc).....	87
Figure 4.18. Effect of CO adsorption on bare Pt atoms of Pt ₃ Sn(111) surface. Pt-close, Pt-second and Pt-far denote the first, second and farthest neighbors, with respect to the distance to the CO adsorption site at 0.125 ML.....	88
Figure 4.19. Ball model of Pt ₃ Sn(111) surface from top and CO adsorption sites available on the surface. Small gray-over-black balls represent CO. Bigger dark and light balls at the sublayer represent Sn and Pt, respectively.....	93
Figure 4.20. Ball model of Pt ₃ Sn(111) surface from top and O adsorption sites available on the surface. Small black balls represent O. Bigger dark and light balls at the sublayer represent Sn and Pt, respectively.....	94
Figure 4.21. LDOS at (a) O adsorbed on three different adsorption sites on Pt ₃ Sn(111) and Pt(111), and (b) Sn before and after O adsorption on site fcc Pt ₂ Sn on Pt ₃ Sn(111).	96
Figure 4.22. Changes in LDOS profiles at Pt atom of (a) fcc Pt ₃ site on Pt(111) and (b) fcc Pt ₂ Sn site on Pt ₃ Sn(111), after O adsorption on site.	97

- Figure 4.23. Ball model of $\text{Pt}_3\text{Sn}(111)$ surface from top and stable O+CO coadsorption sites. Small black and gray-over-black balls represent O and CO, respectively. Bigger dark and light balls at the sublayer represent Sn and Pt, respectively. 98
- Figure 4.24. Surface structure at CO-atop Pt/O-fcc Pt_2Sn coadsorption on $\text{Pt}_3\text{Sn}(111)$. The lines indicate the positions of the Pt atom under CO and Sn atom under O with respect to other two Pt atoms. 101
- Figure 4.25. CO-atop Pt/O-fcc Pt_2Sn coadsorption structure at a total surface coverage of (a) 0.25 ML (CO+O) (b) 0.375 ML (CO+2O) Small black and gray-over-black balls represent O and CO, respectively. Bigger dark and light balls at the sublayer represent Sn and Pt, respectively. 102
- Figure 4.26. The adsorption energy of CO as a function of total coverage (CO+O) 103
- Figure A.1. (a) Initial guess for the reactant structure (b) the calculated transition state after the first LST calculation (c) Initial guess for the product structure. 110
- Figure A.2. The calculated energy versus reaction coordinate after the first LST/QST calculation. 111
- Figure A.3. The optimized reaction path by “TS Confirmation” tool. The energy minimum between the reactant structure and the product structure designates the fact that the reactant structure is not directly connected to the transition state and there is a need for a second LST/QST calculation. 111
- Figure A.4. The calculated energy versus reaction coordinate after the second LST/QST calculation. A new guess for the reactant structure is entered based on the results of TS Confirmation calculation. 112
- Figure A.5. The final optimized reaction path: (a) reactant structure (b) transition state (c) product structure 112

Figure B.1. LDOS at surface Pt atom of the Pt(111) system. Electron distribution obtained with AER calculations is concentrated at lower energy values, compared with those obtained with AE calculations.	113
Figure B.2. LDOS at C atom for the CO/Pt(111) system. C molecular orbitals are at lower energy values for AER calculations, compared with those obtained with AE calculations.	114
Figure B.3. LDOS at surface Pt atom of the Pt(111) system. Electron distribution obtained with AER calculations is concentrated at lower energy values, compared with those obtained with plane-wave basis sets and ultrasoft pseudopotentials.	114

LIST OF TABLES

Table 4.1.	Energy required for the exchange between a Ni substrate atom and a Pt adatom. All values are given in J/m^2	52
Table 4.2.	Charge distribution at valance orbitals of surface metal atoms and changes during surface alloy (SA) formation.....	52
Table 4.3.	Surface energy (E_{Surf}) and surface stress (S) of Ni(111) and Pt-Ni surface alloys with different Pt concentrations at surface layer I (topmost surface layer) and layer II (second layer). First column gives the top view of stable surface structures: Dark, big balls represent Pt, small, grey ones represent Ni atoms.....	53
Table 4.4.	Oxygen adsorption energy (E_{ads}) of the most stable three-fold (fcc) hollow site of surfaces with different Pt concentrations, charge transferred to O during chemisorption, (q) the final stress after chemisorption (S') and related oxygen-metal (O-M) bond lengths (r) at adsorption structure.....	59
Table 4.5.	Surface energy (E_{Surf}) Ni(111), Pt(111) and Pt-Ni surface alloys with 25 per cent Pt concentration at topmost surface layer. Calculations are performed with two different basis sets: (i) including relativistic effects (AER) and excluding relativistic effects (AE). First column gives the top view of stable surface structures: Dark, big balls represent Pt, small, grey ones represent Ni atoms.....	66
Table 4.6.	Charge distribution at valance orbitals of surface metal atoms and changes during surface alloy formation. Calculations are performed with two different basis sets: (i) including relativistic effects (AER) and excluding relativistic effects (AE).	67

Table 4.7.	Energy of CH ₃ and H adsorption and CH ₃ +H coadsorption on Ni(111) and Pt-Ni surface alloy (SA).....	69
Table 4.8.	The activation energy (E_{ads}), heat of reaction (ΔE_{rxn}) and bond lengths (r) at the transition state.....	74
Table 4.9.	Energy of CO adsorption on Pt(111). The values correspond to total adsorption energy per unit cell. Adsorption energy of single CO molecule, in case there is more than one per each cell, is given in brackets where appropriate. Sites are labeled as T(atop), B _{Pt} (bridge), H _{hcp} (hollow hcp) and H _{fcc} (hollow fcc). T-B _{Pt} is for half-atop and half-bridge, and T-H _{fcc} is for half-atop and half-hollow fcc type adsorption. ...	79
Table 4.10.	Energy of CO adsorption on Pt ₃ Sn(111). Although saturation coverage (θ) is below 0.5 ML on Pt-Sn alloy, the structures at this coverage were tested to analyze deeply the stability-electronic structure interaction. Sites are labeled as T(atop), B _{Pt} (bridge on Pt), B _{Sn} (bridge on Sn), H _{hcp} (hollow hcp) and H _{fcc} (hollow fcc).	86
Table 4.11.	Calculated CO adsorption energies and bond lengths on Pt ₃ Sn(111).....	93
Table 4.12.	Calculated O adsorption energies and bond lengths on Pt ₃ Sn(111).....	95
Table 4.13.	Calculated CO adsorption energies on O precovered surface and changes in the adsorption energy upon O+CO coadsorption on Pt ₃ Sn(111) (total surface coverage is 0.5 ML)	99
Table 4.14.	Calculated CO and O adsorption energies as a function of surface coverage (θ)	103

LIST OF SYMBOLS/ABBREVIATIONS

AE	All-electron core treatment
AER	All-electron relativistic core treatment
AES	Auger electron spectroscopy
CI	Configuration interaction model
DFT	Density functional theory
DNP	Double-numeric quality basis set with polarization functions
EELS	Electron energy loss spectroscopy
EXAFS	Extended x-ray absorption fine structure
eV	Electronvolt
fcc	Face-centered cubic
FP	Fuel processor
GGA	Generalized-gradient approximation
Ha	Hartree
hcp	Hexagonal-centered cubic
HOMO	Highest occupied molecular orbital
HREELS	High resolution electron energy loss spectroscopy
HTS	High temperature shift
LTS	Low temperature shift
IRP	Intrinsic reaction path
LDA	Local-density approximation
LST	Linear synchronous transit maximization
LEED	Low energy electron diffraction
LEIS	Low energy ion scattering spectroscopy
LDOS	Local density of states
LUMO	Lowest unoccupied molecular orbital
ML	Monolayer
MP	Møller-Plesset model
MP2	Second-order Møller-Plesset model
NEB	Nudged elastic band
OSR	Oxidative steam reforming

PBE	Perdew-Burke-Ernzerhof functional
PEMFC	Polymer electrolyte membrane fuel cell
ppm	Particle per million
PROX	Preferential oxidation of carbonmonoxide
QST	Quadratic synchronous transit maximization
RAIRS	Reflection absorption infra red spectroscopy
RDS	Rate determining step
RPBE	Revised Perdew-Burke-Ernzerhof functional
SR	Steam reforming
STM	Scanning tunneling microscopy
TS	Transition state
WGS	Water-gas shift
XANES	X-ray absorption near edge structure
XPS	X-ray photoelectron spectroscopy
XRD	X-ray diffraction

1. INTRODUCTION

The world's energy demand in the form of electricity is expected to grow at a rate of 2.4% between now and 2030 [1]. New energy production technologies will be needed in the long-term imposed by the energy policies aiming to reduce the emission of greenhouse gases (CO_2 , SO_x and NO_x) to the environment. In this respect, fuel cell is one of the promising technologies for satisfying a portion of the future energy demand. The low temperature fuel cell technology, polymer electrolyte membrane fuel cell (PEMFC), which has been designed for mobile and small-scale immobile applications, is based on an electrochemical reaction during which oxygen and hydrogen combine to form water. As water is the only product when pure hydrogen is used as the feed, fuel cells have an advantage over internal combustion systems in terms of limited production of harmful pollutants. The lack of hydrogen distribution network and technological obstacles in storing it at low pressure levels impose production of hydrogen from hydrocarbons having available distribution network and safe storage possibilities. Thus, producing pure hydrogen from hydrocarbons, like LPG (various combinations of propane and butane) or methane, on site, either for mobile or immobile uses, is of great scientific interest. The device called "fuel processor (FP)" converts hydrocarbon feeds to pure hydrogen. Even when hydrogen fuel is generated from hydrocarbons via using fuel processors that are combined with PEMFC systems, the emissions can be limited to only CO_2 , and small amounts of hydrocarbons generated during start up. In general, due to the relatively low operating temperatures in fuel processing on active catalysts compared to the internal combustion systems, pollutants such as NO_x and particulates can be avoided. Another advantage of fuel cells is their high efficiency; as a result of the intensive research that has been focused in this area for the last decades, the current efficiency of fuel cell based electricity production has reached as high as 50-60 per cent, which is over the efficiency of an internal combustion engine, which can reach 45 per cent at maximum [2-4].

FP's have reforming, water-gas shift (WGS) and preferential oxidation (PROX) units in series. Steam reforming (SR) is the main reforming route applied in industry to convert a hydrocarbon fuel into hydrogen. Due to its abundancy in nature and economical advantage, Ni is the active metal used in commercial steam reforming catalysts. The final product

stream of the SR unit consists of hydrogen, carbon monoxide and carbon dioxide. As the reaction is highly endothermic, SR of hydrocarbons requires an external heat source. An alternative reforming route, which is especially suitable for transportation and small scale immobile applications, is oxidative steam reforming (OSR) for which the heat needed for SR is produced by the partial catalytic oxidation of the hydrocarbon feed. OSR process has limited commercial experience, but on the other hand, it has theoretically many advantages compared to traditional SR, and has a great potential to be used in future commercial systems.

WGS and PROX units of FP can be classified as the “enriching and purification” sections: In the WGS unit, CO concentration in the stream coming from the reformer is decreased through an equilibrium reaction between the water vapor and CO, while the stream is enriched by the additional hydrogen produced from water. Since WGS is an equilibrium reaction, more than one WGS reactors – typically a high temperature reactor ($>350\text{ }^{\circ}\text{C}$) and low temperature reactor ($210\text{--}330\text{ }^{\circ}\text{C}$) – are generally used in series; the high temperature reactor has fast kinetics, but the conversion level that can be reached is limited by thermodynamics. The low temperature reactor, on the other hand, is used to convert the carbon monoxide to levels down below 1-2 per cent. An efficient FP must produce hydrogen having the purity specs imposed by the PEMFC. Since the Pt anode of a commercial PEMFC can operate stable only at CO levels below 10-40 ppm, PROX unit following the WGS unit should decrease CO concentration in hydrogen rich stream down to that level. In the PROX unit, CO should be eliminated via selective catalytic oxidation of CO in the presence of water vapor, oxygen, carbon dioxide and excess amounts of hydrogen. Among the catalysts tested, noble metal based, especially Pt-based catalysts show the highest activity especially at low temperatures, which favor CO oxidation in the presence of hydrogen while maintaining high selectivity and stability.

As for all catalytic systems, for the reactors of an FP unit, catalyst design is a key element to improve the efficiency of the performance of each individual reactor and the overall process, as well. Experimental studies have proven that alloying offers the opportunity to obtain new catalysts with enhanced selectivity, activity and stability. OSR activity of monometallic Ni catalysts can be improved by alloying Ni with another noble metal, like Pt. Similarly, alloying Pt with another metal element like Sn results in an

increased performance of the catalyst used for the PROX reaction. Surface sensitive techniques and other catalyst characterization methods provide important information on the surface properties of the bimetallic catalysts, and give clues about the reasons of their enhanced activity. Experiments with these techniques revealed that the surfaces of bimetallic catalysts often show structural and chemical properties that are distinctly different from those of the parent metals. In the case of Pt-Ni OSR catalyst, substitutional Pt-Ni surface alloy formation is confirmed by surface science experiments, and it was found that oxygen affinity of this bimetallic surface is lower than monometallic Ni, even when the Pt mixing is at trace amounts. For this reason, Pt incorporation into Ni supports the surface to preserve its metallic form in the presence of oxygen, which at the end results in a bi-functional catalyst that is efficient in both SR and oxidation reactions. In the case of Pt-Sn alloys, presence of Pt and Sn atoms together on the surface at atomic distances allows formation of distinct adsorption sites for each of the reactants, CO and O, and eliminates the adsorption competition between these two species. Separation of the adsorption structures of the reactants eventually leads to new reaction pathways for the CO oxidation reaction to proceed at reduced temperatures.

As a consequence of improved catalytic properties and novel surface chemistry of bimetallic systems, the number of experimental studies on bimetallic surfaces has increased rapidly during the last two decades. Recent developments in computer technology have also provided another path to the researchers for analyzing the surface at atomistic level and obtain knowledge that is either impossible or time consuming with the experimental methods. The ultimate aim of computational studies is to fill in the knowledge gap at the fundamental level that relates the catalytic activity to the chemistry of a surface and, in this way, provide information to tailor the surface properties of a catalyst and enhance its efficiency (Figure 1.1). In the case of the bimetallic catalysts, this fundamental knowledge will make it possible to know a priori how the chemical properties of a metal surface would be affected after alloying and what would be the effect of these changes on the catalytic activity.

The aim of this thesis is to obtain information on catalytic activity of transition metals used in different steps of hydrogen production and purification by analyzing the electronic structure and chemistry of the metal surface and its relation with the adsorbates.

Density functional theory (DFT) calculations have been utilized on Pt-Sn and Pt-Ni bimetallic alloys, to analyze the electronic structure for their energetically most stable configuration, and their reactivity in specific reactions, namely methane OSR in the case of Pt-Ni and CO oxidation in the case of Pt-Sn. The studies performed within the framework of this the current thesis can be categorized into four parts: (i) Structure of stable Pt-Ni surface alloys and their oxygen chemisorption properties, (ii) Methane dehydrogenation over Pt-Ni surface alloys, (iii) CO adsorption on Pt(111) and Pt₃Sn(111) surfaces, and (iv) Oxygen adsorption and CO and O coadsorption on Pt₃Sn(111) surface.

The initial part of the study is focused on oxygen chemisorption on Pt-Ni surface alloys, because oxygen is one of the reactants in OSR. Oxygen chemisorption on Pt-Ni surface alloy has been studied aiming to shed light on the decreased oxidation tendency of the Ni surface after Pt doping. To model the Pt-Ni surface alloy structures, surface Ni atoms in periodic cells were substituted by Pt atoms. The stabilities of these surface alloy structures were compared based on their surface energies and the changes in the surface energies were explained based on the electronic structure of the surface atoms and the corresponding surface stress. Oxygen adsorption energy was calculated on these surface alloys and compared with the results found for monometallic Pt and Ni surfaces and bulk Ni₃Pt alloy. The results confirmed that Pt-Ni mixing at the surface layer forms stable structures at low energy values and oxygen chemisorption is weakened on these surface alloy structures.

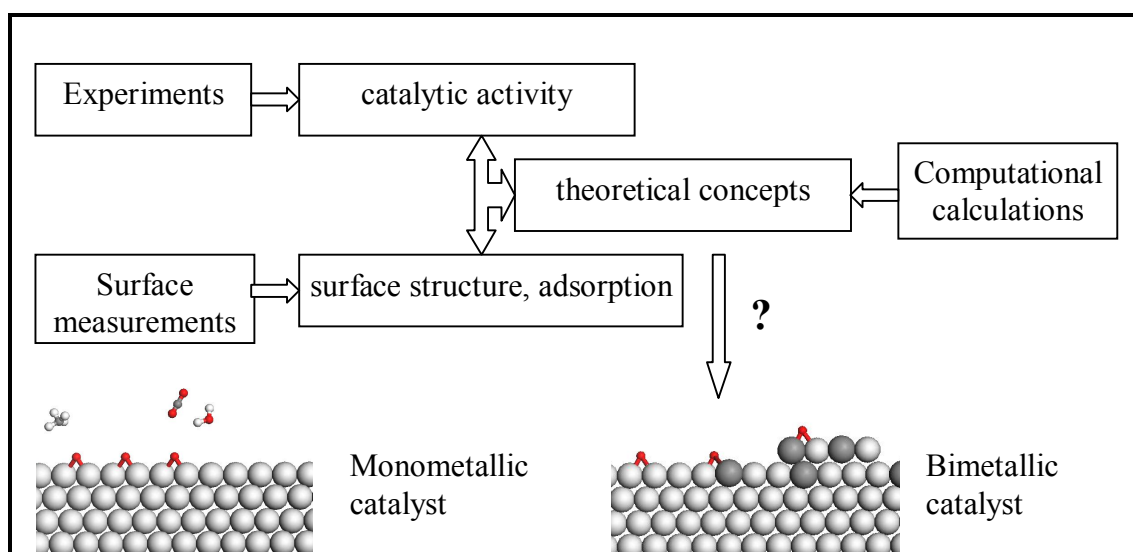


Figure 1.1. Designing efficient bimetallic catalysts

The elementary reaction step of methane dehydrogenation is one of the most important steps of OSR mechanism. In the second part of the work, methane dehydrogenation reaction was studied on Pt-Ni surface alloys and the reaction kinetics was compared with that on monometallic Ni. The energetically favorable reaction mechanisms were found for monometallic Ni(111) and Pt-Ni surface alloy having trace amounts of Pt substituted into Ni(111) surface. The activation energy and the heat of reaction were computed and the results were analyzed based on the electronic structure of the surface and the calculated adsorption energy of the products, CH_3 and H , for both surfaces.

The next part of the work is related to CO oxidation reaction of PROX unit, which is carried on monometallic Pt and Pt-Sn bimetallic alloy catalysts. Experimental studies confirmed that Pt_3Sn is the main active phase of Pt-Sn system supported on nitric acid oxidized activated carbon. The strength of CO adsorption on Pt_3Sn alloy has pronounced effects on the activity and performance stability characteristics of the catalyst. In this study, CO adsorption on Pt(111) and on $\text{Pt}_3\text{Sn}(111)$ were analyzed for CO surface coverages ranging between 0-0.5 ML via using quantum mechanical simulations. Considering that a correct description of CO site preference on the metal surface is crucial and that DFT-AER calculations have been proven to give the correct site preference for CO adsorption on Pt(111), DFT-AER was used in this study to analyze CO adsorption on both pure Pt and Pt-Sn alloy. The effect of CO surface coverage on (i) electronic reconstruction of free sites; (ii) extent of adsorbate-adsorbate and adsorbate-surface interactions (iii) adsorption structure of CO were parametrically studied. The local density of states (LDOS) profiles were used as the tool in analyzing the changes in the electronic structures of the free and occupied states of surface metal atoms, as well as that of adsorbed CO. The adsorbate-adsorbate interaction was studied by analyzing both the equilibrium geometric structures and LDOS profiles in a combined fashion. Based on LDOS, the parameters that may cause changes in the occupation of sites with varying coverages and the differences between pure Pt and Pt-Sn alloy surface, in this respect, were tried to be explained.

In the final part of the study, the adsorptive properties of the Pt_3Sn alloy were investigated for CO and O coadsorption; here the results of the previous part were extended further to cover the changes in the binding strength of O and CO on the metal

surface led by coadsorption. The study also includes a parametric investigation on the relation between relative surface concentrations of CO and O and their adsorption energies.

In this thesis; Chapter 2 contains a detailed literature survey on fuel processing, specifically, the catalytic steps of FP's and problems related to the activity of the catalysts used. Chapter 3 presents the background of DFT and the computational methodology used in this study. The results obtained are presented and discussed in Chapter 4. Chapter 5 consists of the conclusions drawn from the present study and recommendations for future work.

2. LITERATURE SURVEY

2.1. Catalytic Hydrogen Production from Hydrocarbon Fuels

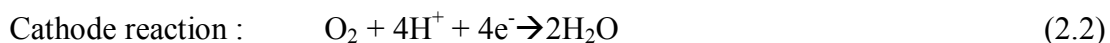
2.1.1. Hydrogen as an Energy Source

According to the International Energy Outlook report, demand for liquid fuels, including both conventional petroleum products and unconventional nonpetroleum liquids such as biofuels, increases from 85.0 million barrels per day in 2006 to 106.6 million barrels per day in 2030 [5]. The transportation sector is second to the industrial sector in terms of current world energy use. However in the long run, it is expected that the increasing cost-competitiveness of other energy sources would cause the industrial sector to switch to other fuels, and as a result, the transportation share of total liquids consumption would increase. Over the next 25 years, world demand for liquids fuels is expected to increase more rapidly in the transportation sector than in any other end-use sector.

According to the same report, emissions from the combustion of liquid fuels made up an estimated 39 percent of the world total energy-related carbon dioxide emissions in 2006. CO₂ is responsible for global warming through the greenhouse effect. Other pollutants emitted by internal combustion engines, such as carbon monoxide, nitrogen oxides, volatile hydrocarbons and particulate matter are all toxic to human health.

New energy production technologies will be needed in the long term imposed by the energy policies aiming to reduce the emission of greenhouse gases and other pollutants to the environment. In this respect, fuel cell is one of the promising technologies for satisfying a portion of the future energy demand. As a result of the intensive research that has been focused on this area for the last decades, the current efficiency of fuel cell based electricity production has reached as high as 50-60 per cent, which is over the efficiency of an internal combustion engines, which can reach 45 per cent at maximum [2-4]. Among the several fuel cell types, PEMFC's are especially suitable for vehicular and small-scale immobile applications due to their low operating temperatures [6].

PEMFC's convert the chemical energy released from the reaction between hydrogen and oxygen into electrical energy. They use H_2 at the anode and O_2 at the cathode as fuels. At the anode, hydrogen is oxidized to protons and electrons. Protons migrate through the proton conducting polymer membrane. Electrons reach the cathode side over an external circuit where power can be drawn. With these electrons, oxygen is reduced at the cathode. The net reaction generates H_2O and electricity. As water is the only product when pure hydrogen is used as the feed, fuel cells have an advantage over internal combustion systems in terms of limited production of harmful pollutants.



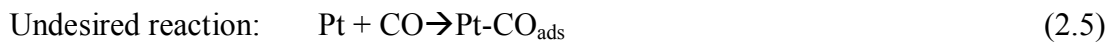
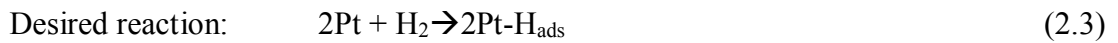
Free hydrogen does not occur naturally and it must be generated. In this respect, hydrogen is just an energy carrier, not a primary energy source. Hydrogen production methods involve electrolysis of water and hydrocarbon reforming. Electrolysis requires too much electrical power, which may be supplied from renewable energy sources as the efficiency of such energy production technologies increases in the long run. Current cost effective method of hydrogen production is hydrocarbon reforming.

The hydrogen feed of a PEMFC can be produced by catalytic conversion of hydrocarbons, such as methane or LPG (a combination of propane and butane). The device called "fuel processor (FP)" converts hydrocarbon feeds to high purity hydrogen. Even when hydrogen fuel is generated from hydrocarbons via using fuel processors, the emission of a combined FP-PEMFC system can be limited to only CO_2 and small amounts of hydrocarbons generated during start up. In general, due to the relatively low operating temperatures of fuel processing on active catalysts compared to the internal combustion systems, pollutants such as NO_x and particulates are avoided. Additionally, significant reduction in carbon dioxide emission is possible if carbon capture or carbon sequestration methods were utilized at the site of hydrogen production. Even if carbon sequestration is not used, according to the reports, a fuel cell vehicle powered by an FP-PEMFC system using natural gas as the fuel, will reduce fuel consumption and CO_2 emission by at least 50

per cent compared to a conventional vehicle with a gasoline internal combustion engine on a well-to-wheels basis by 2020 [7].

The main disadvantage of PEMFC's is that they are very sensitive to impurities in hydrogen, which may be produced during hydrogen production by FP's. The major contaminant is carbon monoxide. In a PEMFC, a polymeric membrane is used between the anode and the cathode; the dehydration of polymeric membrane at higher temperatures limits the working temperature of fuel cell ca. 80-90 °C to prevent the condensation of water which acts as a transporter between the two electrodes. The most efficient anode catalyst for H₂ electrochemical oxidation is platinum. However, the Pt anode catalyst is known to deactivate by even trace levels of carbon monoxide in the H₂ fuel, especially below 100 °C. Carbon monoxide blocks a large number of free sites that could be used for H₂ adsorption and this causes a significant decrease in the stability in power production of the fuel cell.

In the presence of carbon monoxide, there are two competing reactions at the anode:



The solution to alleviate the deactivation problem of Pt anode catalyst is to deliver clean H₂ to the anode electrode. The hydrogen-rich stream generated by hydrocarbon reforming always contains some amount of carbon monoxide, typically around 0.5–2 per cent CO, and the most suitable way to remove this carbon monoxide is the selective catalytic oxidation of CO to CO₂.

2.1.2. Fuel Processors

A fuel processor (FP) is a catalytic device used for producing CO-free hydrogen feed to be used in a PEMFC, and has at least three units: reforming, WGS and PROX (Figure

2.1). To improve the overall efficiency of an FP and to reduce its cost, the focus of catalysis research is now on the design of new FP catalysts that are very active, poison-resistant and stable. Additionally, the catalysts should have performance that would reduce the required catalytic volumes and shorten the start-up times.

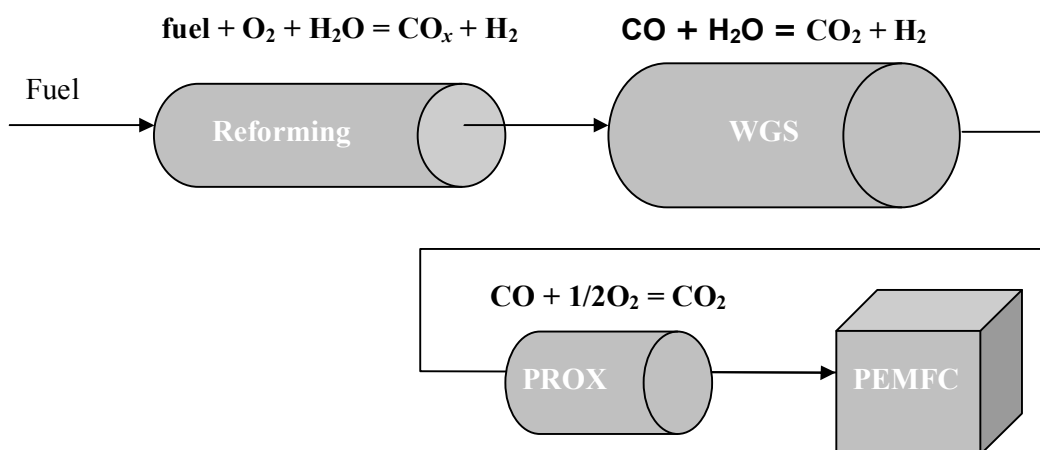


Figure 2.1. Fuel processors

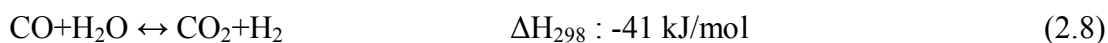
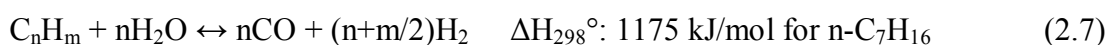
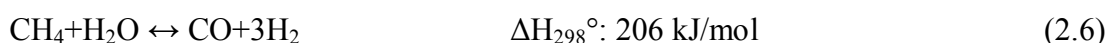
SR is the main reforming route applied in industry to convert a hydrocarbon fuel into hydrogen. The final product stream of the SR unit consists of hydrogen, carbon monoxide and carbon dioxide. The reaction was first studied in Germany in the beginning of the century and introduced to industry in the 1930s as natural gas became available as a low-cost feedstock.

The importance of the SR process comes from the facts that this process is the first step in a number of very important large scale chemical processes and it can use methane, which is an abundant hydrocarbon in the world, as the feed. SR is a way to produce large amounts of hydrogen used in many different areas of industry and especially in the refineries. It is the first step in the synthesis of ammonia where the hydrogen is reacted with nitrogen from air over an iron catalyst. It is also the first step in the production of methanol which is synthesized from a mixture of H_2 , CO , and CO_2 over a copper/zinc oxide/alumina catalyst.

SR reaction is strongly endothermic and it is favorable to run the reaction at relatively high temperatures (700–1100 °C), and high steam-to-hydrocarbon ratio in order to achieve maximum conversion. The pressures of 20–40 bar typically applied in industrial

reforming units are dictated by the high pressures in the synthesis loops, the necessity of high throughput and low pressure drop on one side and the reduced conversion and increasing cost of using high pressures on the other side. Traditionally, SR reaction is performed in a tubular design where vertical tubes are loaded with the catalyst and furnaces are built around them. Natural gas is used to heat the tubes by simple combustion.

These reactions occur in SR unit:



An alternative reforming route is oxidative steam reforming (OSR). In OSR, the heat needed for SR is produced by the partial catalytic oxidation of the hydrocarbon feed [8]. OSR is practical for mobile and small size immobile applications because it reduces the size and heat limitation of the steam reformer with less coking and with faster start-up. OSR process has limited commercial experience, but on the other hand, it has theoretically many advantages compared to traditional SR and a great potential to be used in future commercial systems.

In the case of heavier hydrocarbon feedstock rather than methane, a low-temperature, fixed bed adiabatic pre-reformer is inserted into the reactor [9] prior to the primary steam reformer to prevent the risk of carbon formation. In the adiabatic pre-reformer, the higher hydrocarbons are completely converted into C1 fragments (CH_4 , CO and CO_2). This is quite similar to the process taking place in conventional reforming, but the relatively low temperatures (350–550 °C) in the pre-reformer eliminate the potential for carbon formation. Moreover, the pre-reformer allows for higher inlet temperatures in the primary reformer, thereby reducing its size.

Catalysis is a key element in the reforming reactions. The catalysts can be divided into two types: non-precious metal (Ni-based) and precious metal based catalysts, which

especially have late transition metals like Pd, Pt, Ru, Rh, and Ir. Among the latter, some of the metals like Ru and Rh are more active than others, however because of the cost considerations, Ni-based catalysts are preferred in the industrial applications. Another reason is that, due to mass and heat transfer limitations, the effectiveness factor of the catalyst in a conventional steam reformer is typically less than 5 per cent and thus, kinetics and the activity of the catalyst are rarely the limiting factors, so using a precious metal rather than Ni has no advantage.

The usage of monometallic Ni catalyst in SR catalyst has four main challenges: activity, sulfur poisoning, carbon formation, and sintering [10]. Activity is especially important in the adiabatic pre-reformer, where the effective activity determines the temperature profile in the reactor and thereby the reactor volume needed to equilibrate the gas mixture. Sulfur adsorption on the catalyst is a problem as sulfur blocks the active sites on Ni catalyst. Carbon formation may block the active sites in a similar way, crushing the catalyst pellet and causing a pressure drop. Finally, sintering, which is the grow in Ni particle size as a result of the high operating temperature and pressure of the reaction conditions, may lead to deactivation and strengthen the effects of the first three factors. A number of possible solutions proposed for the above mentioned problems will be summarized below.

In the case of activity, it is known by experimental kinetic studies that CH_4 dissociation is the rate controlling step at SR of methane on Ni and thus, plays a crucial role [11]. The studies showed that the activation energy of methane dissociation on Ni catalyst ranges from 0.77 to 1.05 eV [11-13]. The reaction is a structure sensitive reaction on Ni and as the size of the Ni particles grows, activation energy required for dissociation also grows [13]. One of the reasons for the variations in activation energy obtained from experiments may be this relation between the size of Ni particles and the activation energy. Computational studies also confirmed that reaction is easier at step sites and the activation energy on these step sites is lower than that on close-packed surface structures [14]. However, it was also proposed that these sites also act as nucleation centers for graphite formation and thus, due to carbon deactivation, the reaction, in the long run, is performed at flat sites [14,15].

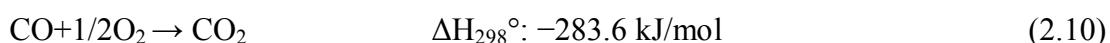
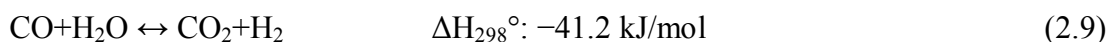
In the case of carbon formation problem, one of the most popular solutions proposed is to mix Ni with another metal, like Sn. Kinetic studies has shown that Sn displaces Ni atoms from the under-coordinated sites on Ni particles and shifts the critical reaction channels from these step sites to flat surface sites. Sn addition also increases carbon resistance and prevents deactivation compared to monometallic Ni due to the Sn-induced lowering in the binding energy of carbon on low-coordinate sites, which serve as carbon nucleation centers [11].

Additional to the mentioned problems of Ni usage in conventional SR catalysts, in the case of OSR, Ni has the disadvantage of having high oxygen affinity and the tendency to be easily oxidized during the reaction conditions. A high operating temperature is required to keep Ni in its metallic state and to preserve its activity. In previous studies, to alleviate this oxygenation problem, Pt-doping into Ni has been proposed as a possible solution [10,16,17]. Recent studies have shown that Pt-Ni bimetallic catalyst has better performance in OSR compared to monometallic Ni especially at lower temperatures. Pt-doping into Ni catalyst decreases the oxidation tendency of the catalyst and supports the surface to stay in reduced metallic form. By this way, the separation of endothermic and exothermic reaction zones, which is caused by the decreased reforming activity of oxidized zone (especially the reactor inlet), is prevented and thus a flat temperature profile along the catalyst bed is obtained.

The units following SR, WGS and PROX units of FP, can be classified as the “enriching and purification” sections: In WGS unit, CO concentration in the stream coming from the reformer part is decreased through an equilibrium WGS reaction between water vapor and CO. In addition to reducing CO concentration in the reformat stream, H₂ concentration is also increased. Since WGS is an equilibrium reaction, more than one WGS reactors – typically a high temperature reactor (>350 °C) and low temperature reactor (210–330 °C) – are generally used in series; the high temperature reactor has fast kinetics, but the conversion level that can be reached is limited by thermodynamics [18]. The low temperature reactor, on the other hand, is used to convert the carbon monoxide to levels down below 1-2 per cent. Fe–Cr oxide and Cu–ZnO–Al₂O₃ are the classical catalysts employed for HTS and LTS units, respectively. WGS shift reactors are the bulkiest components of the fuel processing system; WGS reactors loaded with classical catalysts

occupy ca. 30–50 per cent of the total catalyst volume and weight of the FP [19]. Thus, new catalyst formulations are being sought which would increase the efficiency and reduce the size of WGS unit.

WGS and PROX reactions:



An efficient FP must produce hydrogen having the purity specs imposed by the PEMFC. Since the Pt-based anode of a commercial PEMFC can operate stable only at CO levels below 10-100 ppm [20], the PROX unit following the WGS unit should decrease CO concentration in hydrogen rich stream down to that level. In the PROX unit, CO should be eliminated via selective catalytic oxidation of CO in the presence of water vapor, oxygen, carbon dioxide and excess amount of hydrogen. Among the catalysts tested, noble metal-based, especially Pt-based catalysts show the highest activity especially at low temperatures, which favor CO oxidation in the presence of hydrogen while maintaining high selectivity and stability [21]. The disadvantage of monometallic Pt catalyst in PROX is that Pt shows significant activity only above 150 °C. At that temperature region reverse WGS starts, which consumes hydrogen and thus decreases the selectivity [22]. Additionally, because PEMFC is usually operated below 100 °C, it becomes crucial to keep the operating temperature of PROX unit low in order to have a better heat integration between the two units.

The common temperature-related problems of Pt catalyst in PROX stem from the strong CO adsorption on Pt, especially at low temperatures. The oxidation of carbon monoxide follows Langmuir–Hinshelwood mechanism with an adsorbed oxygen species formed by dissociative chemisorption. In the case of single-phase platinum, carbon monoxide blankets the metal surface, displacing the weakly chemisorbed oxygen species, and prevents the reaction unless the temperature is high enough to desorb some of the carbon monoxide on the catalyst surface. As a result, the rate-determining step of carbon

monoxide oxidation is desorption of carbon monoxide from the catalyst surface followed by oxygen adsorption.

Due to the above mentioned importance of CO adsorption in determining the overall PROX reactivity of the Pt catalyst, there are a vast number of research papers, both experimental [23-26] and theoretical [27-32], published in this area. Additionally, CO adsorption on transition metal surfaces is considered a good model system for studying the details of the bonding process of gas molecules on the metal substrates. Surface science studies showed that CO adsorption occurs only linearly on Pt(111) at the low surface coverage. These atop-adsorbed CO forms a structure with a $(\sqrt{3} \times \sqrt{3})R30^\circ$ pattern starting from coverages as low as 0.17 ML till 0.33 ML. The maximum coverage obtainable with only linearly-adsorbed CO on the surface is 0.33 ML; bridge-type occupation has been reported to be observed above 0.25 ML coverage. A $c(4 \times 2)$ structure starts to form at 0.35 ML and becomes uniform at 0.5 ML, for which half of the CO are adsorbed atop while the rest are adsorbed on bridge sites. No three-fold adsorption has been observed at any coverage. Theoretical studies also provide valuable information in general for the adsorption structure of reactants on metal surfaces. Still, it should be noted that there are a number of problems to be overcome before we can truly rely our conclusions obtained from these tools, especially in the case of CO adsorption on Pt(111) surface. In a bulk number of previous studies performed with DFT, the adsorption structure of CO on Pt(111) was falsely predicted and different reason and solutions have been proposed to alleviate computational problem [30,31].

Recent studies in heterogeneous catalysis have shown that bimetallic alloy surfaces have high catalytic activities in PROX, especially when compared to monometallic catalysts like supported Pt. Several groups have reported enhanced PROX activities at lower temperatures after the addition of a second metals, like Fe [33,34], Sn [35,36], Ce [37], Co [38,39]. Addition of alkali metals, such as Mg and Na may also increase the catalytic activity of Pt [40,41]. Experimental and theoretical calculations showed that this enhancement in the activity of bimetallic alloys in CO oxidation is through a combination of so-called “bifunctional” and “electronic effects”. In the former, the existence of a second metal at the bimetallic alloy surface creates highly favorable sites for oxygen adsorption and thus eliminates the previously mentioned competition between CO and O

during adsorption. For example, it was found that alloying Pt with Fe creates additional Fe-based sites on the surface special for O adsorption [33,34]. In the case of electronic effect, electronic modification of the primary surface metal atom Pt, due to alloying leads to a weakening in CO adsorption strength and thus, the surface CO coverage is decreased and the surface becomes more active for the reaction to proceed. For example, it has been proven that CO adsorption on Pt-Sn alloy is weaker than that on monometallic Pt [42,43]. Additionally, CO adsorption structure is different: On Pt₃Sn(111), presence of multicoordinated CO adsorption sites are observed starting from very low CO coverages, whereas on monometallic Pt, only linear adsorption is possible unless the surface coverage of CO is very high. On the alloy surface, atop adsorption is still the most favorable structure, similar to that on monometallic Pt, but apart from bridge sites, adsorption on threefold hollow sites is also possible whereas hollow adsorption structure is not observed at any coverage on monometallic Pt [44]. Similar to that on Pt-Fe alloys, on Pt-Sn, CO adsorbs on Pt sites, whereas oxygen is adsorbed on both Pt and Sn sites [45,46].

The type of catalyst support is another variable affecting the nature of catalytically active sites of Pt-Sn bimetallic alloy and thus, its performance in PROX. Experimental studies by Aksoylu et al. [35,36] showed that CO oxidation performance of activated-carbon supported bimetallic Pt-Sn catalyst is dependent directly on the ratio of the number of the metallic Pt sites to those of the Pt₃Sn alloy sites and that the optimal ratio guarantees very high level of activity with long-term stability. The studies indicate that the types and relative abundance of active sites can be modified by altering surface chemistry when activated carbon is used as the catalyst support. For example, the oxidized form of AC, especially the HNO₃-oxidized form, which is rich in carboxylic acid groups, favors formation of the Pt₃Sn alloy, in addition to formation of metallic Pt centers. The surface chemical properties of AC supports, on the other hand, can be modified with different oxidative pretreatment methods.

2.2. Catalytically Active Bimetallic Alloys: General Information

Bimetallic catalysts in general have a wide range of application in areas such as, hydrogenation of olefins, carbon monoxide hydrogenation, ammonia synthesis, hydrocarbon and alcohol dehydrogenation [47] and thus, a great number of experimental

studies have been conducted on these systems. Supported bimetallic alloys are generally prepared by impregnation or coprecipitation of salts on the support. This prepared mixture is then exposed to specific pretreatment procedures, such as heat pretreatment (calcination), to increase the degree of interaction and structure stability and reduction, to reduce metallic species to their zero valance states. The active sites formed on fresh catalyst upon those pretreatments can be categorized as monometallic, bulk alloy and surface alloys (Figure 2.2). Bulk alloys are either random substitutional alloys or ordered compounds with specific lattice constants and crystal structures. On the other hand, alloying extends only to the surface region in the case of surface alloys and is composed of either single atomic layers or multilayer surface alloys (epitaxial alloys) which is several atomic layers thick structures.

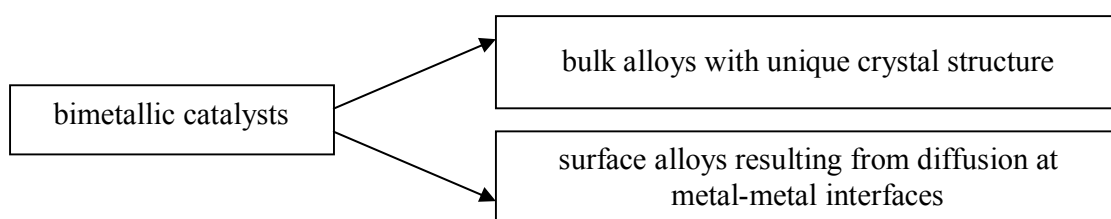


Figure 2.2. Types of bimetallics

Determination of the structure and composition of a catalyst surface and its active centers is an essential part for understanding the underlying reasons of the activity and selectivity of a catalyst. Catalyst characterization methods such as x-ray diffraction (XRD), Auger electron spectroscopy (AES) and x-ray photoelectron spectroscopy (XPS) are useful to identify the phases which are present in a catalyst and to obtain local electronic and structural properties of the catalyst surface. Among these, XRD is utilized to study the type and abundance of bulk crystals on catalyst surface; AES is used to analyze the surface concentrations; and XPS is used for finding the types of metallic species present on the catalyst surface and their oxidation states. Additionally, surface crystallographic techniques, such as low energy electron diffraction (LEED), scanning tunneling microscopy (STM), low and high energy ion scattering spectroscopy (LEIS and HEIS) can be used to determine the local crystal formations, surface defects and atomic coordinates of the species present within the first few layers of the surface. Among the x-ray absorption techniques, extended x-ray absorption fine structure (EXAFS) can be used to determine the atomic number, distance and coordination number of the atoms surrounding an element

present in the surface layer and x-ray absorption near edge structure (XANES) can provide information about vacant orbitals, electronic configuration and site symmetry of the absorbing atom. The adsorption site and structure of gas molecules on the surface can be determined by electron energy loss spectroscopy (EELS) or reflection absorption infra red spectroscopy (RAIRS) from the vibrations of adsorbed molecules on surfaces. These studies are performed under ultra-high vacuum whenever the methodology involves charged particles, either electrons or ions, sent to the metal surface considering the fact that they should not be hindered by any obstacles during the propagation. In other cases, the characterization methodologies are performed *in-situ* in order to provide the exact structure of the catalyst surface during the operating conditions. Additionally, some of these techniques have recently been used for real time imaging of reactions taking place on surfaces. A list of alloy structures reported in the literature using these methods are given by Bardi [48].

Chemical properties of alloys may strongly deviate from the properties of its constituent metals. It is difficult to know a priori how the chemical and electronic properties of a particular bimetallic surface will be modified during alloying relative to the pristine metals. The catalyst characterization methods are in general difficult to apply to alloys or the process is extremely time consuming. Calculations based on atomistic models, in this respect, are also very useful to define the stable composition and structures of alloys. These models, such as ‘embedded atom method’ and ‘effective medium theory’ are semi-empirical tools which define the total energy of a metal as the sum of a pair potential and an atomic energy. In addition to these, recent developments in computational infrastructure and computer technology yielding extremely high computational power has enabled the density functional (DFT) methods which had only limited usage previously in the area of alloys, due to the requirement of excessive number of atoms to model the alloy system to be characterized by its surface structure and catalytic activity. DFT calculations alleviate the major problems in semi-empirical methods by self-consistent solution of charge density and they give better description of many surface properties [49]. Although their accuracy is not yet perfect, still these calculations can be used to define general concepts when they are used with experimental studies in combined fashion.

2.2.1. Electronic Properties of Bimetallic Catalysts and Their Effect on Surface Stability, Adsorption and Reactivity

According to the results of the studies performed on bimetallic alloys, there are two possible reasons of the variations in the electronic and chemical properties of a bimetallic surface with respect to its pristine metals. First, is the so-called ligand or electronic effect, through which the heterogeneous bonds and charge transfer through these bonds between different types of metal atoms cause a reconstruction in the electronic structure of surface atoms and change their adsorptive properties. Second is the so-called strain effect through which the average metal bond lengths change due to the differences between the equilibrium radii of two metals. Although those two effects are interrelated, depending on the alloying metals, the relative influence of the two effects can be arranged. For instance, during alloy formation by mixing of two metals located far apart in the periodic table, as in the case of Pt_3Sn alloy (Figure 2.3), the modified properties can be best explained by direct electronic interaction. However, especially in the case of surface alloys formed by mixing of two transition metals of the same column of the periodic table, like Ni, Pd or Pt, the stress induced due to the changes in metal-metal bond lengths is more dominant than the changes between the nature of these bonds (Figure 2.4). Thus, understanding these two factors is important to tailor their catalytic properties of the alloys in a desired way. DFT is a powerful tool to create artificial systems through which we can analyze the importance of different factors affecting the alloy properties separately, whenever needed.

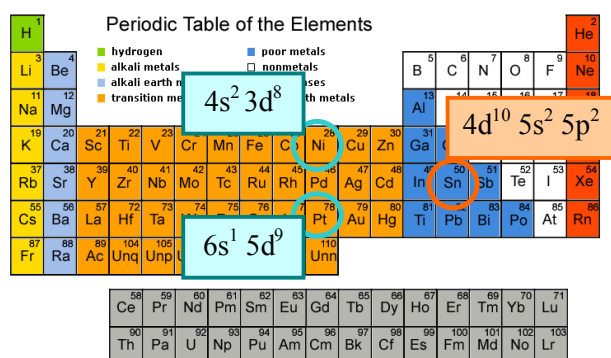


Figure 2.3. Electronic distribution at the valance states of Ni, Pt and Sn

In addition to the ligand and strain effects, presence of a second metal at the catalyst surface may in some cases change the adsorption site preference of some reactants which

sometimes eliminates the adsorption competition between the adsorbates and resultantly may create alternative reaction pathways that are not observed on monometallic surfaces. Pt-Sn, Pt-Fe and Pd-Au alloys in CO oxidation reaction can be cited as examples [33,34,45,46,50]. The creation of possibility of new reaction pathways by changing the sequence of adsorption-site preference of reactants in this way is called as “bifunctional effect”.

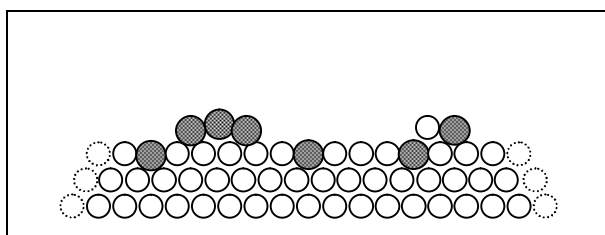


Figure 2.4. Bimetallic alloy surface formed by diffusion at the metal-metal interfaces. If the two metals have similar electronic structures, then their mixing mainly causes a strain effect due to the difference in their atomic sizes.

2.2.2. Electronic Reconstruction during Alloying

In order to monitor the changes in the catalytic properties of a surface atom during the alloying process, specific parameters defining the electronic structure should be analyzed first. However, finding such a unique parameter that would explain the major chemical and catalytic properties by itself, even for a monometallic surface, is a difficult task. When metals are tried to be categorized, the primary parameter that would be used is the atomic mass and electron configuration, as in the periodic table. However, the periodic table is only useful to categorize the properties of metals in bulk; in the case of surface, which dominantly defines the catalytic activity of a metal, both the electronic configuration and chemical properties may show large deviations even for metals at the same column of the periodic table.

Through utilizing DFT methods, researchers have made a few attempts to define such parameters. Norskov group has published several papers on the relation between the electronic structure and catalytic reactivity since 90's [51-58] and their proposed model has become one of the most widely used one. According to the so-called d-band model [55,56] the d-band center, which is the first moment of the d-band density of states, or in other

words, the average energy of the d-band is a critical factor that dominantly determines the adsorption strength of many simple adsorbates on the surface atoms. Since the sp bands of the transition metals are broad and structureless, whereas the d-bands are narrow, small changes in the environment can change the d-states and their interaction with adsorbate states significantly. In this way, the changes in d-band center, which is the simplest possible measure for the position of the d-states, affect the changes in the adsorption strength. In practice, the model predicts that as the center of the d-band shifts to lower energies, adsorption energies are increased (i.e., the bonds grow weaker). This relation can be explained through the downward shift of the d-band, which causes antibonding orbitals that previously resided above the Fermi level to shift below it, and hence become occupied by electrons. This occupation of previously empty anti-bonding orbitals causes a corresponding destabilization of the adsorbate bond. Based on this model, alloying and the accompanying interaction between the atoms cause a shift in the d-band of the surface metal atoms and eventually affect the adsorption process and chemical reactivity [57]. An example is given in Figure 2.5. The major problems with the model is its deviations from experimental studies for various adsorbent-adsorbate combinations and the fact that it neglects the changes in surface metal-metal bonds and claimed to be oversimplified as it excludes the role of s and p orbitals.

2.2.3. Adsorption versus Surface Stress

Deposition of a layer of metal onto a substrate metal with larger or smaller radius causes compressively stressed or tensile strained layers, with lateral metal-metal bonds contracted or expanded. Although the interaction between the atoms of two different species having different electronic configurations would eventually create a difference in the chemical properties of the surface, the influence of this ligand effect may be, in some cases, of secondary importance compared to the effect created during the contraction or expansion of the surface. A good example is the alloying of two metals, from the same column in the periodic table, both of which have similar electronic configurations at the valence band at some degree but different metallic radii due to the difference in their atomic weights, such as Pt and Ni [59].

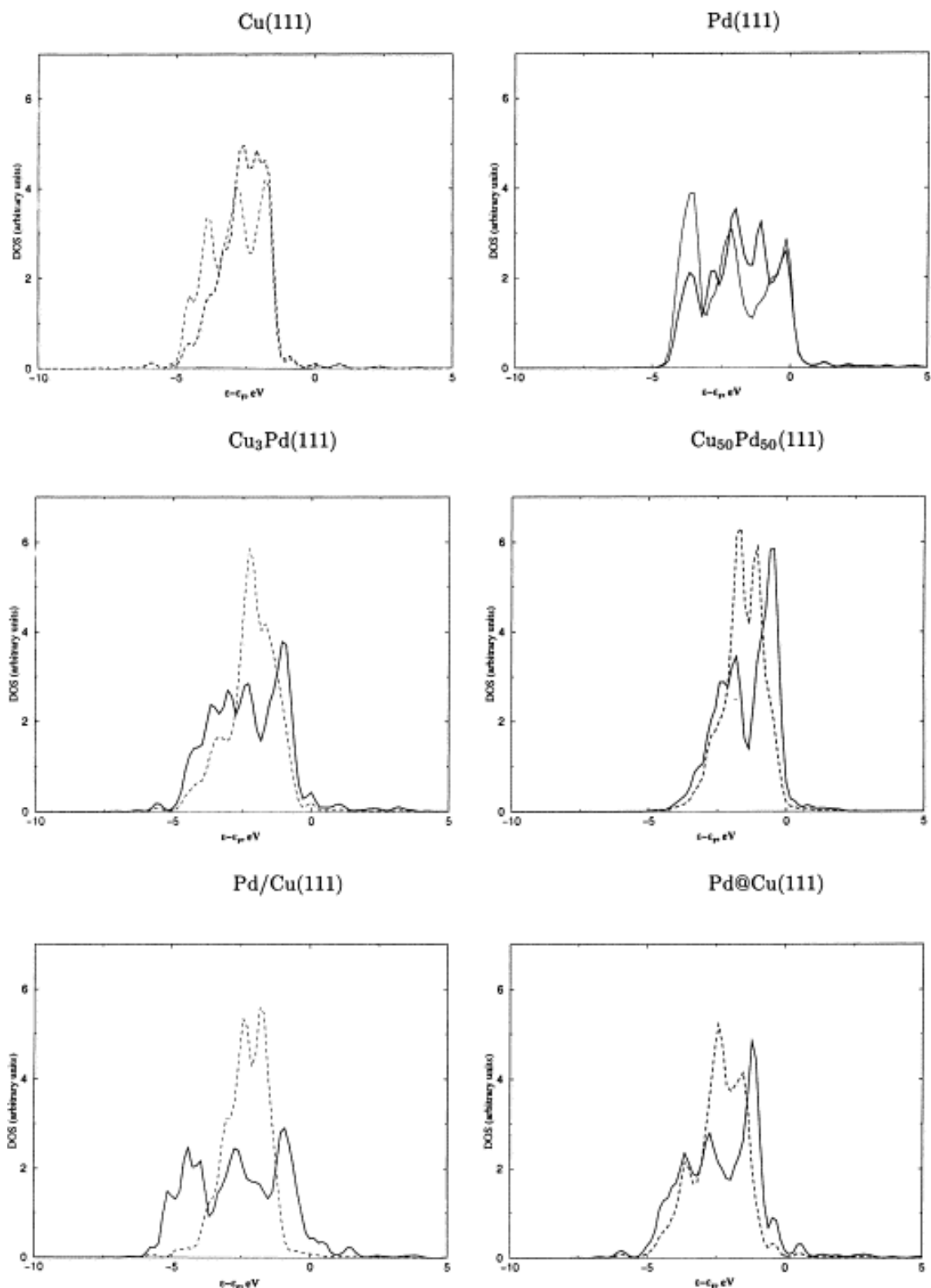


Figure 2.5. Changes in Pd and Cu valance band during alloy formation (d-band only). The top panel corresponds to pure metals; central panel correspond to bulk alloys; bottom panel surface alloys. Solid lines stand for Pd atoms and dashed lines for Cu atoms. Thick lines represent surface atoms and thin lines bulk atoms [58].

Surface stress was first introduced by Gibbs at the beginning of the 19th century [60,61]. It has become a topic of interest in surface science, since it is intricately related to the surface electronic structure and bonding, and thus the catalytic activity [59]. Additionally, it is influential on the surface stability and surface reconstruction. A deeply defined theory of the concept and a summary of its applications in materials science can be found at the paper by Haiss [61]. Experimental studies can not measure the stress of a surface directly. Instead, these studies are used to measure the change caused by adsorbates or reconstruction. Therefore, theoretical studies of surface stress are of a great importance.

In one of the earliest ab-initio studies on surface stress, Fiorentini et al. has found the impact of stress on the tendency of 5d metal surfaces to reconstruct [62]. According to his model, there is a large tensile stress effective on late transition metal surfaces because relativistic effects on these heavy atoms cause charge depletion in d-states of surface metal atoms and filling of s orbitals, which are contracted and reduce their energy to a value closer to d-states. Metal-metal bonding, according to his model is explained by the equilibrium between delocalized, repulsive s and p electrons, and localized attractive d electrons. However, this trend is reversed in late transition metals: sp electrons now bind the crystal whereas the nearly full d-band weakens the bonds between the metals. Thus, charge depletion in anti-bonding d-states increases metal-metal bond strength and cause a large stress in 5d metals, whereas it is not such large in 4d metals which are under less relativistic effects. As a result, Ir, Pt, and Au have a tendency at (001) surface terminations to reconstruct to a close-packed quasihexagonal structure, whereas stress is not large enough for 4d metals to overcome the substrate resistance to reconstruction. In variance with the study of Fiorentini et al., Kollar and Vitos proposed a different model for the reason of large tensile stress on 5d metals [63]. By again using ab-initio calculations, they found the total charge density of the surface metals decrease, whereas d-states are slightly more occupied. The stress increase which goes in parallel with these changes, is explained based on the model for which the equilibrium bond length is determined by the interaction between repulsive and delocalized s and p electrons, and localized attractive d electrons.

Using DFT calculations, Umeno et al. calculated the change in electron chemical potential or workfunction in Au slabs under strain to find a correlation with the surface stress response to surface charge, thus elucidating the requirement of explicit introduction

of an excess charge into the calculations [64]. When the electron chemical potential grows with an increasing strain in the plane, the resultant workfunction response to strain has a slope with negative sign. This proves, in a qualitative way, that positively charged Au surfaces tend to expand laterally and vice versa.

The stress change during oxygen and hydrogen adsorption on Pt(111) was calculated by Feibelman in order to analyze the adsorption induced stress [65]. The difference between the two adsorbates is that O is an electron acceptor while H is an electron donor. Thus H adsorption leads to a decrease in work function while O adsorption leads to an increase. Accordingly, the stress change due to the adsorption of these two species would act oppositely. However it was found that tensile stress on Pt(111) is relieved by the adsorption of both oxygen and hydrogen. The reason is as follows: Adsorption weakens the bonds between the first neighbors of the adsorbate, the adatoms allow the remaining bonds to contract, and relieves their tensile stress. As an example, it was found that Co adatoms on Au(001) surface reduce the local tensile stress and lead to an inhomogeneous stress distribution [66].

Some researchers had analyzed the changes in the adsorption energy due to strain on the surface. During CO adsorption on Au(001), adsorption energy increases (adsorption weakens) when a compressive lateral strain is applied and the opposite occurs when expansion is applied. This is true for the three fold site which is the most favorable adsorption site. However, the opposite is true for the top site [67].

In a paper by Mavrikakis et al., it was shown how tensile stress applied to Ru(0001) surface by means of a stretch in the lattice constant, changes the reactivity of the surface [68]. It was proven that there is nearly a perfect linear relationship between the changes in the adsorption strength of O or CO and the change in the lattice constant. The dependence is more emphasized for the O adsorption. The electronic interference was that tensile stress decreases the width of the d-band of the Ru(0001) surface, which in consequence shifts the center of d-band to upper values in energy and thus affects adsorption. The opposite relation was reported for compressed Pt(111) [69].

In bimetallic systems, it is very difficult to separate whether electronic interaction or strain effects influence the reactivity of a surface more, due to the fact that those two are closely related. Pt atoms in interaction with 3d transition metals in bulk are studied with DFT within slabs having dimensions corresponding to pure Pt, i.e. without any lateral strain exposed to Pt [52]. For every 3d metal replacing Pt, it was found that d-band of the topmost surface Pt atoms widens. However, this widening does not cause any significant change in the band occupation ratio. Instead, to keep the area under the density of states curve constant, the intensity of the curve decreases while its width increases (Figure 2.6). This decrease in the height of the curve causes a natural shift in the d-band center. The findings indicated that the density of states at the Fermi level, the d-band center for the total density of states and the width of the d-band are all correlated.

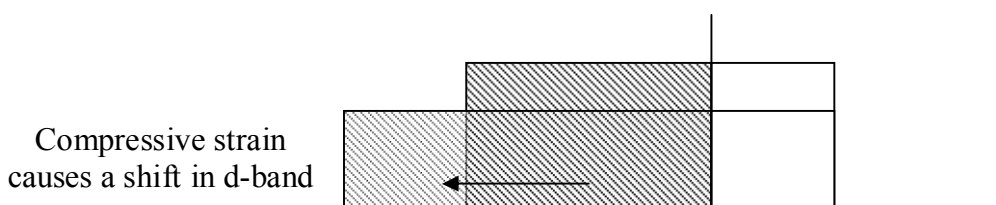


Figure 2.6. Simplified rectangular model to define the changes in the structure of the d-band of Pt atoms that are under the effect of strain

In a following paper, they further extended their analysis to bimetallic systems under the influence of both strain and ligand effects. There is a similar linear relationship between the d-band width and the matrix element of the surface layer stretched, due to lattice mismatch between the underlying substrate metal, such as Ni/Pt surface alloys. As the charge transfer between the metals is small, i.e. change in d-band filling is negligible, changes in the band width causes a shift in the d-band center, similar to above mentioned Pt/metal/Pt sandwich systems [70]. This change in d-band center affects the chemical properties of the surface.

In Pd–Au bimetallic systems, incorporation of larger Au atoms into Pd substrate may introduce two opposite influences on the catalytic activity of the Pd surface [50]. The tensile strain caused by the incorporation of the larger Au atoms into the Pd lattice shifts the d-band center upwards relative to the Fermi level; as a consequence, it will strengthen

the interaction between the adsorbates and the metal surface. At the same time, the ligand effect of Au results in a downshift of the d-band center, thus weakening the binding of the adsorbates and metal surface. It should be noted that this weakening in the adsorption of the reactants is generally thought to imply a lower activation energy and an easier reaction. Hence, the adverse strain effect and the advantageous ligand effect are competitive in the case of Au on Pd bimetallic system.

A similar situation is reported for Pt clusters over Ni(111) [71]. The reduction of the Pt–Pt bond length leads to a shift of the island d-band to lower energies. And the lower coordination of the island atoms leads to a shift of the d-band to higher energies.

3. METHODOLOGY

3.1. Theory behind Computational Methods: Quantum Chemical Models

Theoretical models that have been developed to calculate molecular structure and energetics are divided into two categories; quantum chemical models and molecular mechanics models.

Quantum chemical models all ultimately stem from the Schrödinger equation. It treats molecules as collections of nuclei and electrons, without any reference to chemical bonds. However, approximations are needed to be made to solve the Schrödinger equation for more than one electron systems. Quantum chemical models differ in the nature of these approximations. Actually, a so-called quantum chemical model is defined as a set of approximations to Schrödinger equation.

The first one of these is the Hartree-Fock approximation that provides the foundation for the so-called Hartree-Fock molecular orbital models, or simply molecular orbital models. The Hartree-Fock approximation assumes that electrons move essentially as independent particles, without interacting with each other. The instantaneous interactions between individual electrons in this model are replaced by interactions between a particular electron and the average field created by all the other electrons. The failures of Hartree-Fock models can be traced to an incomplete description of “electron correlation” or simply stated, the way in which the motion of one electron affects the motions of all the other electrons. The electrons are in reality further away from each other than predicted by Hartree-Fock approximation. Two fundamentally different approaches for improvement of Hartree-Fock models have emerged.

One approach is to construct a more flexible description of electron motions in terms of a combination of Hartree-Fock descriptions for ground and excited states. Configuration interaction (CI) and Møller-Plesset (MP) models are the two of the most commonly used models of this type. The so-called second-order Møller-Plesset model (MP2) is the most practical and widely employed model.

An alternative approach to improve Hartree-Fock models involves using an additional explicit term to account for the way in which electron motions affect each other. In practice, this account is based on an “exact” solution for an idealized system, and is introduced using empirical parameters. The resulting models are referred to as density functional models.

The Hartree-Fock approximation also provided the basis for what are called semi-empirical models. These introduce additional approximations as well as empirical parameters to greatly simplify the calculations, with minimal adverse effect on the results. While this goal has yet to be fully realized, several useful schemes have resulted, including the popular AM1 and PM3 models.

The alternative to quantum chemical models is so-called molecular mechanics models. These do not start from an “exact-theory” (the Schrödinger equation), but rather from a simple but chemically reasonable picture of molecular structure. In this picture, the molecules are made up of atoms and bonds (as opposed to nuclei and electrons), and atom positions are adjusted to best match known structural data (bond lengths and angles), as well as to accommodate non-bonded interactions. This is much simpler than solving the Schrödinger equation for electron motions, but requires an explicit description of chemical bonding, and a large amount of information about the structures of molecules, as well. The use and extent of those information distinguishes different molecular mechanics models [72].

3.1.1. Schrödinger Equation

All quantum mechanical models ultimately trace back to Schrödinger equation, which written for the special case of the hydrogen atom is as follows:

$$\left[-\frac{1}{2}\nabla^2 - \frac{Z}{r} \right] \psi(r) = E\psi(r). \quad (3.1)$$

Here, the quantity in square brackets represents the kinetic energy and potential energy of an electron at a distance r from a nucleus of charge Z . E is the electronic energy and ψ , a

function of the electronic coordinates, Ψ , is a wave function describing the motion of the electron. Wavefunctions for the hydrogen atom are the familiar s,p,d... atomic orbitals.

3.1.2. Many-body Problem

For a multinuclear, multielectron system, the Schrödinger equation is written as such:

$$\hat{H}\Psi = E\Psi. \quad (3.2)$$

Here, Ψ is a many-electron wavefunction and \hat{H} is the so-called Hamiltonian operator (or more simply the Hamiltonian).

$$\hat{H} = -\frac{1}{2} \sum_i^{\text{electrons}} \nabla_i^2 - \frac{1}{2} \sum_A^{\text{nuclei}} \frac{1}{M_A} \nabla_A^2 - \sum_i^{\text{electrons}} \sum_A^{\text{nuclei}} \frac{Z_A}{r_{i,A}} + \sum_{i < j}^{\text{electrons}} \frac{1}{r_{ij}} + \sum_{A < B}^{\text{nuclei}} \frac{Z_A Z_B}{R_{AB}} \quad (3.3)$$

Z is the nuclear charge, M_A is the ratio of mass of nucleus A to the mass of an electron, R_{AB} is the distance between nucleus A and nucleus B, r_{ij} is the distance between electrons i and j, and r_{iA} is the distance between electron i and nucleus A.

The many-electron Schrödinger equation can not be solved exactly, so approximations are introduced to provide practical models. The first one of them is the Born-Oppenheimer approximation. Its validity, with regard to the calculation of molecular structure and relative energetics, has been proven to be true.

3.1.3. Born-Oppenheimer Approximation

Because of the large difference in mass between the electrons and the nuclei, the motion of nuclei is slow compared to the electrons (which have a motion at the speed of light); thus, it is assumed the nuclei do not move. This is called the Born-Oppenheimer approximation and leads to the separation of electronic and nuclear coordinates in the many-body wave function.

The ‘electronic’ Schrödinger equation can be written as $\hat{H}^{\text{el}}\Psi^{\text{el}} = E^{\text{el}}\Psi^{\text{el}}$, where

$$\hat{H}^{\text{el}} = -\frac{1}{2} \sum_i^{\text{electrons}} \nabla_i^2 - \sum_i^{\text{electrons}} \sum_A^{\text{nuclei}} \frac{Z_A}{r_{i,A}} + \sum_{i<j}^{\text{electrons}} \frac{1}{r_{ij}}. \quad (3.4)$$

The nuclear-nuclear Coulomb interaction is a constant and is added to the electronic energy, E^{el} , to yield the total energy E .

$$E = E^{\text{el}} + \sum_{A<B}^{\text{nuclei}} \frac{Z_A Z_B}{R_{AB}}. \quad (3.5)$$

Even with this simplification, the many-body problem remains formidable. Further simplifications, however, can be introduced to allow total-energy calculations to be performed accurately and efficiently. These include density-functional theory to model the electron-electron interactions, pseudopotential theory to model the electron-ion interactions, supercells to model systems with periodic geometries, and iterative minimization techniques to relax the electronic coordinates [73].

3.1.4. Electron-electron Interactions

The most difficult problem in any electronic structure calculation is posed by the need to take the effects of the electron-electron interactions into account. Most first-principles approaches recast the problem from one where electron interactions are explicit to one where the interactions are represented by an effective potential acting on apparently independent electrons. The interactions are hidden in the effective potential, and one deals with one electron at a time. The result is a set of one-electron Schrödinger-like equations :

$$H\Psi_n = \left(-\frac{1}{2} \nabla^2 + V_{\text{ext}} + V_{\text{eff}} \right) \Psi_n = \epsilon_n \Psi_n. \quad (3.6)$$

Here, ψ_n are the one-electron wavefunctions, V_{ext} is the external potential of the nuclei and V_{eff} is the effective potential. An early approach for V_{eff} was developed by Hartree. He set

V_{eff} to the average of the Coulomb potential between an electron and all the others in the system, giving what is now called the Hartree potential. An electron experiencing this potential is said to move in the mean field of the other electrons.

The missing point in the Hartree approach is that it neglects the exchange and correlation effects. The wave function of a many-electron system must be antisymmetric under exchange of any two electrons since the electrons are fermions. The antisymmetry of the wave function produces a spatial separation between electrons that have the same spin and thus reduces the Coulomb energy of the electronic system. The reduction in the energy of the electronic system due to the antisymmetry of the wave function is called the exchange energy.

Hartree-Fock approach treats the exchange interaction properly. The effective potential is now non-local, and arises from the demand that the total wavefunction be antisymmetric upon exchange of any two electrons. However, the method remains inherently approximate since it neglects the correlation.

Electrons repel each other due to the Coulomb interaction between their charges. In the Hartree-Fock approximation, the electrons get in each others way to a greater extent than they should. This leads to overestimation of the electron-electron repulsion energy and to too high total energy. If electrons that have opposite spins are also spatially separated, the Coulomb energy of a system of electrons can be reduced but this has to be balanced against the kinetic energy cost of deforming the electronic wave functions in order to separate the electrons. Electron correlation, as it is termed, accounts for coupling or “correlation” of electron motions, and leads to a lessening of the electron-electron repulsion energy.

3.1.5. Density Functional Models

One approach to the treatment of electron correlation is DFT. DFT is “ab-initio” in the sense that it is derived from first-principles and does not require adjustable parameters. Its advantages are: (i). Both exchange and correlation effects are included in DFT (ii). DFT is not as computationally demanding as the other ab-initio methods, such as CI or MP2.

Density functional models have at their heart the electron density, as opposed to the many-electron wavefunction, $\Psi(r_1, r_2, \dots)$. Hohenberg and Kohn [74] proved that the total energy, including exchange and correlation, of an electron gas (even in the presence of a static external potential) is a unique functional of the electron density. If the true exchange-correlation functional can be used, DFT theoretically would give the exact solution, however the exact exchange-correlation functional required for this purpose is unknown. The minimum value of the total-energy functional is the ground-state energy of the system, and the density that yields this minimum value is the exact single-particle ground-state density. Kohn and Sham [75] then extended the theory to practice by showing how the energy can be partitioned into kinetic energy, potential energy and electron-electron repulsion terms and showed how it is possible, formally, to replace the many-electron problem by an exactly equivalent set of self-consistent one-electron equations. The energy is written as

$$E = E_T + E_V + E_J + E_{xc} \quad (3.7)$$

Here, E_J is the Hartree Coulomb term for electron-electron interaction, which does not include exchange and correlation effects and E_V is the electron-nuclear interaction energy. The electron energy is given by E_T . E_{XC} is the exchange and correlation energy. Except from E_T , all others depend on the total electron density, $\rho(r)$.

$$\rho(r) = 2 \sum_i^{\text{orbitals}} |\psi_i(r)|^2. \quad (3.8)$$

Here ψ_i are the so-called Kohn-Sham orbitals and the summation is carried over pairs of electrons.

Within a finite basis set, the energy components may be written as follows [72]:

$$E_T = \sum_{\mu} \sum_{\nu}^{\text{basisfunctions}} \int \phi_{\mu}(r) \left[-\frac{1}{2} \nabla^2 \right] \phi_{\nu}(r) dr, \quad (3.9)$$

$$E_v = \sum_{\mu}^{\text{basisfunctions}} \sum_{\nu} P_{\mu\nu} \sum_A^{\text{nuclei}} \int \phi_{\mu}(\mathbf{r}) \left| \frac{Z_A}{|\mathbf{r} - \mathbf{R}_A|} \right| \phi_{\nu}(\mathbf{r}) d\mathbf{r}, \quad (3.10)$$

$$E_J = \frac{1}{2} \sum_{\mu}^{\text{basisfunctions}} \sum_{\nu} \sum_{\lambda} \sum_{\sigma} P_{\mu\nu} P_{\lambda\sigma} (\mu\nu | \lambda\sigma), \quad (3.11)$$

$$E_{xc} = \int f(\rho(\mathbf{r}), \nabla\rho(\mathbf{r}), \dots) d\mathbf{r}. \quad (3.12)$$

Here, Z is the nuclear charge, $\mathbf{R}-\mathbf{r}$ is the distance between the nucleus and the electron, P is the so-called density matrix, the elements of which involve a product of two molecular coefficients summed over all occupied molecular orbitals, and $(\mu\nu | \lambda\sigma)$ are two-electron integrals, f is an exchange/correlation functional, which depends on the electronic density and perhaps the gradient of the density as well.

Only the minimum value of the Kohn-Sham energy functional has physical meaning. At the minimum, the Kohn-Sham energy functional is equal to the ground-state energy of the system of electrons. Minimizing E with respect to the unknown orbital coefficients yields a set of matrix equations, the “Kohn-Sham equations”. These are n Schrödinger-like equations for n non-interacting electrons moving in an effective potential. In the KS equations, the effective potential is the Kohn-Sham potential, which is defined as the functional derivative

$$V_{\text{KS}}(\mathbf{r}) = \frac{\delta}{\delta\rho(\mathbf{r})} (E_J[\rho(\mathbf{r})] + E_{\text{xc}}[\rho(\mathbf{r})]) = V_{\text{H}}(\mathbf{r}) + \frac{\delta E_{\text{xc}}[\rho(\mathbf{r})]}{\delta\rho(\mathbf{r})}. \quad (3.13)$$

Defining the exchange-correlation potential, V_{xc} , formally by the functional derivative,

$$V_{\text{xc}}(\mathbf{r}) = \frac{\delta E_{\text{xc}}[\rho(\mathbf{r})]}{\delta\rho(\mathbf{r})}. \quad (3.14)$$

Then, the following is obtained, where ψ_i is the wave function of electronic state i , ϵ_i is the Kohn-Sham eigenvalue, and V_H is the Hartree potential of the electrons:

$$\left[-\frac{1}{2}\nabla^2 + V_{\text{ion}}(\mathbf{r}) + V_H(\mathbf{r}) + V_{\text{XC}}(\mathbf{r}) \right] \psi_i(\mathbf{r}) = \epsilon_i \psi_i(\mathbf{r}). \quad (3.15)$$

Finding a functional E_{XC} that handles the complexity of interacting electrons remains the great challenge in DFT. There are two major approximations to solve this problem. The most widely used is the local-density approximation (LDA), which was introduced by Kohn and Sham along with KS equations. The LDA states that E_{XC} can be given by assuming that the exchange-correlation energy is that of a uniform electron gas of density $\rho=\rho(\mathbf{r})$. Then,

$$E_{\text{XC}} = \int d\mathbf{r} \rho(\mathbf{r}) \epsilon_{\text{XC}}(\rho(\mathbf{r})), \quad (3.16)$$

where $\epsilon_{\text{xc}}(\rho)$ is the exchange-correlation energy per electron in a uniform gas of density ρ . However in reality, the charge density is highly non-uniform around the atoms. Functionals that have been developed that include dependence on the gradient of the density are called generalized-gradient approximation (GGA).

The set of wave functions that minimize the Kohn-Sham energy functional are given by the self-consistent solutions to the Kohn-Sham equations. The Kohn-Sham equations must be solved self-consistently so that the occupied electronic states generate a charge density that produces the electronic potential that was used to construct the equations. At the process, the first step is to estimate a V_{KS} . Then this potential is used in Equation 3.15 to solve for the wave function, ψ_i . The found wave functions are used to calculate the density via Equation 3.8. Finally, the density is used to calculate a new V_{KS} . The iteration continues until V_{KS} and density converge.

3.1.6. Periodic Supercells

The supercell approximation allows one to deal with two problems: an infinite number of electrons in the system each for which a wave function must be calculated, and

since each electronic wave function extends over entire solid, an infinite basis set is required to expand each wave function. Both problems can be surmounted by performing calculations on periodic systems and applying Bloch's theorem to the electronic wavefunctions.

3.1.7. Bloch's Theorem

The main advantage of imposing periodic boundary conditions relates to Bloch's theorem, which states that in a periodic system each electronic wave function can be written as a product of a cell-periodic part (f term) and a wavelike part (exponential term). The following may be termed as Bloch's wavefunction:

$$\psi_i(\mathbf{r}) = \exp[i\mathbf{k} \cdot \mathbf{r}] f_i(\mathbf{r}). \quad (3.17)$$

Note that $\exp(i\mathbf{k} \cdot \mathbf{r})$ equals to $\cos(\mathbf{k} \cdot \mathbf{r}) + i \sin(\mathbf{k} \cdot \mathbf{r})$. The Bloch theorem changes the problem of calculating an infinite number of electronic wave functions to one of calculating a finite number of wave functions at an infinite number of k-points. The occupied states at each k-point contribute to the electronic potential, so that in principle an infinite number of calculations are needed. However, the electronic wave functions at k-points that are very close together will be almost identical. Hence, it is possible to represent the electronic wave functions over a region of k space by the wave functions at a single k point. This suggests that the DFT expressions that contain a sum over k-points (or, equivalently, an integral over the Brillouin zone) can be efficiently evaluated using a numerical scheme that performs summation over a small number of special points in the Brillouin zone. In addition, symmetry considerations suggest that only k-points within the irreducible segment of the Brillouin zone should be taken into account.

3.1.8. Plane-Wave Basis Set

Two main choices for the cell periodic part can be used in Bloch's wavefunction, amounting to a choice of basis set function: The first one is the traditional localised orbitals based on atomic orbital functions (as in DMOL3). This has the advantage of molecular orbital type interpretation, but is difficult to implement. The second one is to expand the

cell periodic part using a basis set consisting of a discrete set of plane waves, as in the form of Fourier transformations, whose wave vectors are reciprocal lattice vectors of the crystal:

$$f_i(\mathbf{r}) = \sum_{\mathbf{G}} c_{i,\mathbf{G}} \exp[i\mathbf{G} \cdot \mathbf{r}] \quad (3.18)$$

where the reciprocal lattice vectors \mathbf{G} are defined by $\mathbf{G} \cdot \mathbf{l} = 2\pi m$ for all \mathbf{l} where \mathbf{l} is a lattice vector of the crystal and m is an integer. Therefore each electronic wave function can be written as a sum of plane waves,

$$\psi_i(\mathbf{r}) = \sum_{\mathbf{G}} c_{i,\mathbf{k}+\mathbf{G}} \exp[i(\mathbf{k} + \mathbf{G}) \cdot \mathbf{r}]. \quad (3.19)$$

In principle, an infinite number of plane waves are required to expand electronic wave functions at each \mathbf{k} -point. However, the coefficients, $C_{i,\mathbf{k}+\mathbf{G}}$, for the plane waves with small kinetic energy, $(1/2)|\mathbf{k}+\mathbf{G}|^2$, are more important than those with large kinetic energies. Thus, the plane wave basis set can be truncated to include only plane waves that have kinetic energies that are smaller than some particular cutoff energy. If a continuum of plane-wave basis states were required to expand each electronic wave function, the basis set would be infinitely large no matter how small the cut-off energy is. Application of the Bloch theorem allows the electronic wave functions to be expanded in terms of a discrete set of plane waves. Introduction of an energy cutoff to the discrete plane-wave basis set produces a finite basis set.

When plane waves are used as a basis set for the electronic wave functions, the Kohn-Sham equations assume a particularly simple form.

$$\sum_{\mathbf{G}} \left[\frac{1}{2} |\mathbf{k} + \mathbf{G}|^2 \delta_{\mathbf{G}\mathbf{G}'} + V_{\text{ion}}(\mathbf{G} - \mathbf{G}') + V_{\text{H}}(\mathbf{G} - \mathbf{G}') + V_{\text{xc}}(\mathbf{G} - \mathbf{G}') \right] c_{i,\mathbf{k}+\mathbf{G}} = \epsilon_i c_{i,\mathbf{k}+\mathbf{G}} \quad (3.20)$$

In this form, the kinetic energy is diagonal, and the various potentials (electron-ion, Hartree, exchange-correlation) are described in terms of their Fourier transforms.

Another advantage of the plane wave basis set is the ease of calculating derivatives of the total energy with respect to atomic displacements, i.e. stresses and forces are computationally cheap in this approach, so that efficient geometry optimization and molecular dynamics schemes can be implemented. It is also straightforward to study and improve convergence of plane-wave basis set calculations, owing to the fact that there is a systematic way of adding more basis functions.

However, there is an additional cost to using the super cell approach for systems that lack periodicity in three dimensions inherently (isolated molecules, defects in solids, surfaces, etc.). In a study of a single defect, for example, the properties of an infinite array of defects would always be calculated. Therefore, it is essential to introduce enough separation between artificial images of such nonperiodic objects to ensure that there is no appreciable interaction between them. The situation is similar for surface calculations that are carried out in slab geometry. The vacuum layer should be sufficiently thick to eliminate artificial interactions between the slabs.

3.1.9. Electron-Ion Interactions (Pseudopotential Theory)

The major disadvantage of planewaves is the slow convergence because of the Coulomb singularities and the rapidly varying density due to the inner electrons. A very large number of plane waves are needed to expand the tightly bound core orbitals and to follow the rapid oscillations of the wave functions of the valence electrons in the core region. The pseudopotential approximation allows the electronic wave functions to be expanded using a much smaller number of plane-wave basis set.

It is well known that most physical properties of solids are dependent on the valence electrons to a much greater extent than on the core electrons. Pseudopotential theory allows one to replace the strong electron ion potential with a much weaker potential – a pseudopotential- that describes all the salient features of a valence electron moving through the solid, including relativistic effects. Thus, the original solid is now replaced by pseudo valence electrons and pseudo-ion cores. These pseudoelectrons experience exactly the same potential outside the core region as the original electrons but have a much weaker potential inside the core region. The fact that the potential is weaker is crucial, however,

because it makes the solution of the Schrödinger equation much simpler by allowing expansion of the wave functions in a relatively small set of plane waves.

3.2. Materials Studio Software

3.2.1. MS Visualizer

DFT calculations in this study are carried out in a repeated slab geometry. Periodic boundary conditions generate a pair of two-dimensionally infinite surfaces, separated by a substantial slab of material in one direction and on the other by a vacuum region. This is performed by Materials Studio (MS) of Accelrys Inc. The core product of MS is the Materials Visualizer. It is used to construct and manipulate graphical models of molecules, surfaces, and layered structures.

In order to construct a surface with MS Visualizer, the first step is to optimize the bulk structure of the material. The bulk crystal structure of a material can be imported from MS library if the material is monometallic, or can be prepared manually depending on the experimental data if the material is not involved in the database. For instance, the ordered Pt_3Sn alloy has the L_{12} structure with tin atoms on the corners of the face-centered cubic unit cell and platinum atoms on the center of faces. Based on this information, the unit cell was drawn using the MS Visualizer. The ball-and-stick model is given in Figure 3.1.

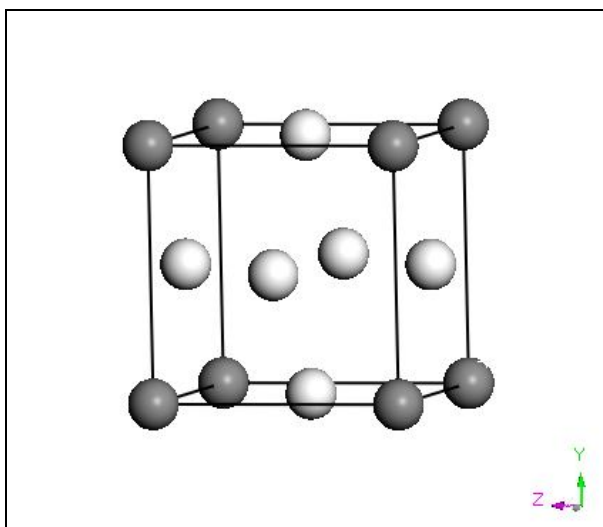


Figure 3.1. The Pt_3Sn unit cell. Dark and light balls represent Sn and Pt, respectively.

Creating the surface, or in other words, building the slab, is a two step process. The first step is to cleave the bulk metal (Figure 3.2-a). In this way, a two dimensional surface is obtained with the desired surface termination (Figure 3.2-b). The cleaving is done by entering the Miller indices of the surface into the specific dialog box and then, specifying the depth of the slab, that is the number of atomic layers in the slab. The second step is to create a vacuum slab over the surface (Figure 3.3). At this step, the thickness of the vacuum layer separating the two surfaces is determined. The slab has to include a sufficiently thick vacuum layer above the adsorbent surface, so that there is not any attraction between the adsorbent surface and the underside of the following slab in z-direction. However, because the computational time needed is directly proportional to the thickness of the slab, one must be careful to choose the appropriate values. In order to keep the computational time at the minimum, while relaxing the surface layers of the slab, the bottom layers are generally kept at their bulk positions.

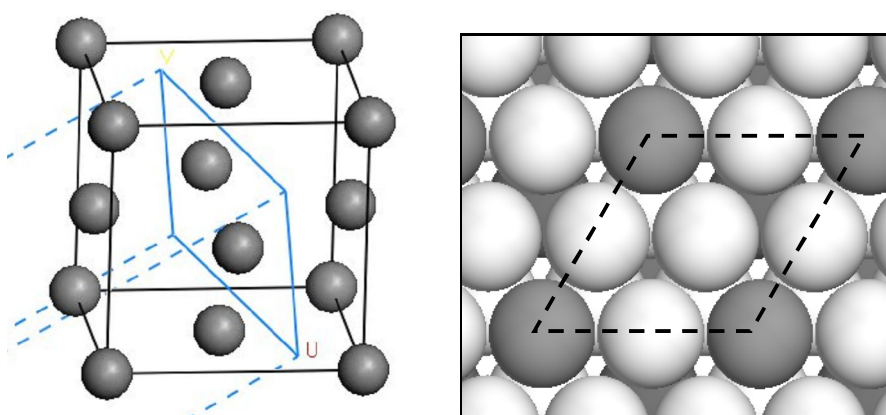


Figure 3.2. (a) Cleaving a Pt unit cell in (111) direction (b) Top view of $\text{Pt}_3\text{Sn}(111)$ surface after cleaving. Dark and light balls represent Sn and Pt, respectively.

After the three-dimensional slab is created, the adsorbates are added at different locations over the surface (Figure 3.4). To check whether the initial guess for the position of the adsorbates are true or not, geometry optimization is performed. During the geometry optimization, the position of atoms are arranged in order to minimize the total energy. For this purpose, MS Visualizer is integrated with special DFT codes, like CASTEP and DMol3 for energy calculations. The total energy of a molecule or a crystal refers to the energy of a specific arrangement of atoms. The zero of the energy is taken to be the infinite separation of all electrons and nuclei, so the total energy is generally negative.

3.2.2. MS CASTEP

CASTEP [76] is a state of the art quantum mechanics based program designed specifically for solid state materials science. CASTEP employs a total energy plane-wave pseudopotential method. In the mathematical model of the material it replaces ionic potentials with effective potentials acting only on the valence electrons in the system. Electronic wavefunctions are expanded through a plane-wave basis set, and exchange and correlation effects in electron-electron interactions can be included within either LDA or GGA approximations. Combining the use of pseudopotentials and plane wave basis sets makes it extremely easy to calculate the forces on the atoms. This enables efficient optimization of ionic configurations of molecules, solids, surfaces, and interfaces. Electronic relaxation in CASTEP is performed with density mixing algorithm, by default. For metallic systems, the valance band occupation is smeared with a typical smearing width.

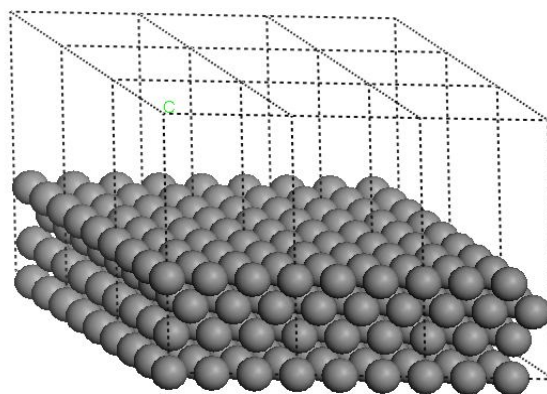


Figure 3.3. Three dimensional slab after creating the vacuum above the surface. The system is composed of repeating units in x,y and z dimensions. Thus, the vacuum should be thick enough to prevent interactions with the repeating cell in z-direction.

3.2.3. MS DMol3

Dmol3 [77,78] is a DFT quantum mechanical code implemented in MS. DMol3 uses numerical orbitals for the basis functions, each function corresponding to an atomic orbital. The basis functions are given numerically as values on an atomic centered spherical-polar mesh, rather than analytical Gaussian orbitals. The angular portion of each function is the

appropriate spherical harmonic and the radial portion is obtained by solving the atomic DFT equations numerically. The possible optimization algorithms like steepest gradient, conjugate gradient or Newton-Raphson are not under user control and is determined automatically depending on the system under study.

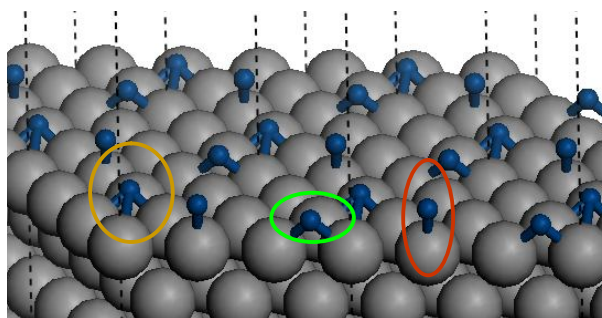


Figure 3.4. Adsorption sites: three-fold, bridge and linear from left to right.

DMol3 offers different ways to treat the core electrons. One of these methods is "All Electron (AE)" which provides no special treatment of cores and includes all electrons explicitly in the calculations. Another one is "All Electron Relativistic (AER)" which includes all electrons explicitly and introduces some scalar relativistic effects into the core. One of the important features of DMol3 is this possibility to explicitly involve or exclude scalar relativistic effects from the calculations. In this way, the influence of scalar relativity on certain properties of the metals, such as the electronic structure, surface stability and adsorptive properties can be investigated. Although the inclusion of scalar relativistic effects in the calculations increases the computational time, the accuracy of the calculations, especially for metals with $Z > 50$, can also be increased in this way.

Relativistic effects are introduced into the Schrödinger equation by Dirac equation [79]. According to the theory, the inner electrons of these heavy elements feel such a large nuclear charge that in order to maintain balance with the strong electrostatic field, they must acquire speeds that are comparable with that of light [80]. If their speed is v and that of light is c , their mass m is increased relative to their rest mass m_0 according to the equation:

$$m = m_0 / (1 - (v/c)^2)^{1/2}. \quad (3.21)$$

Due to that mass increase, the s orbitals and additionally the p electrons at a lesser extent, shrunk; d and f orbitals, on the other hand, increase in energy and move outwards radially, as their effective potentials are screened more efficiently due to the relative contractions of the s and p shells.

Dmol3 is an efficient and fast algorithm and it is especially very useful in transition state search. During the course of chemical reaction, the total energy naturally changes. Starting from the reactants, the energy increases to a maximum and then decreases to the energy of the products. The maximum energy along the reaction pathway is known as the activation energy; the structure corresponding to this energy is called the transition state (TS). A TS is a stationary point (i.e., one in which the forces on the atoms are zero) for which the energy is maximum in one direction (the direction of the reaction coordinate) and is minimum in all other directions.

In this study, synchronous transit methods implemented in DMol3 were used for locating the TS. Starting from reactants and products, the synchronous transit methods interpolate a reaction pathway to find a TS. The method begins by performing an LST/Optimization calculation (Figure 3.5). The Linear Synchronous Transit (LST) [81] method performs a single interpolation to a maximum energy. An idealized set of structures connecting reactant and product is obtained by linearly interpolating the distances between pairs of atoms in the reactant and product according to

$$r_{ab}^i(f) = (1 - f)r_{ab}^R + fr_{ab}^P, \quad (3.22)$$

where r represents the inter-nuclear distances between the pair of atoms a and b and f is an interpolation parameter which varies between 0 and 1. For the calculation of the actual LST path, a modified version of the equation is used for periodic systems.

The TS approximation obtained with LST is used to perform a Quadratic Synchronous Transit (QST) maximization. QST method alternates searches for an energy maximum with constrained minimizations in order to refine the TS to a high degree. From that point, another conjugate gradient minimization is performed. The cycle is repeated until a stationary point is located or the number of allowed QST steps is exhausted. The

result of each of these calculations is a trajectory document. A detailed review of the method can be found elsewhere [82].

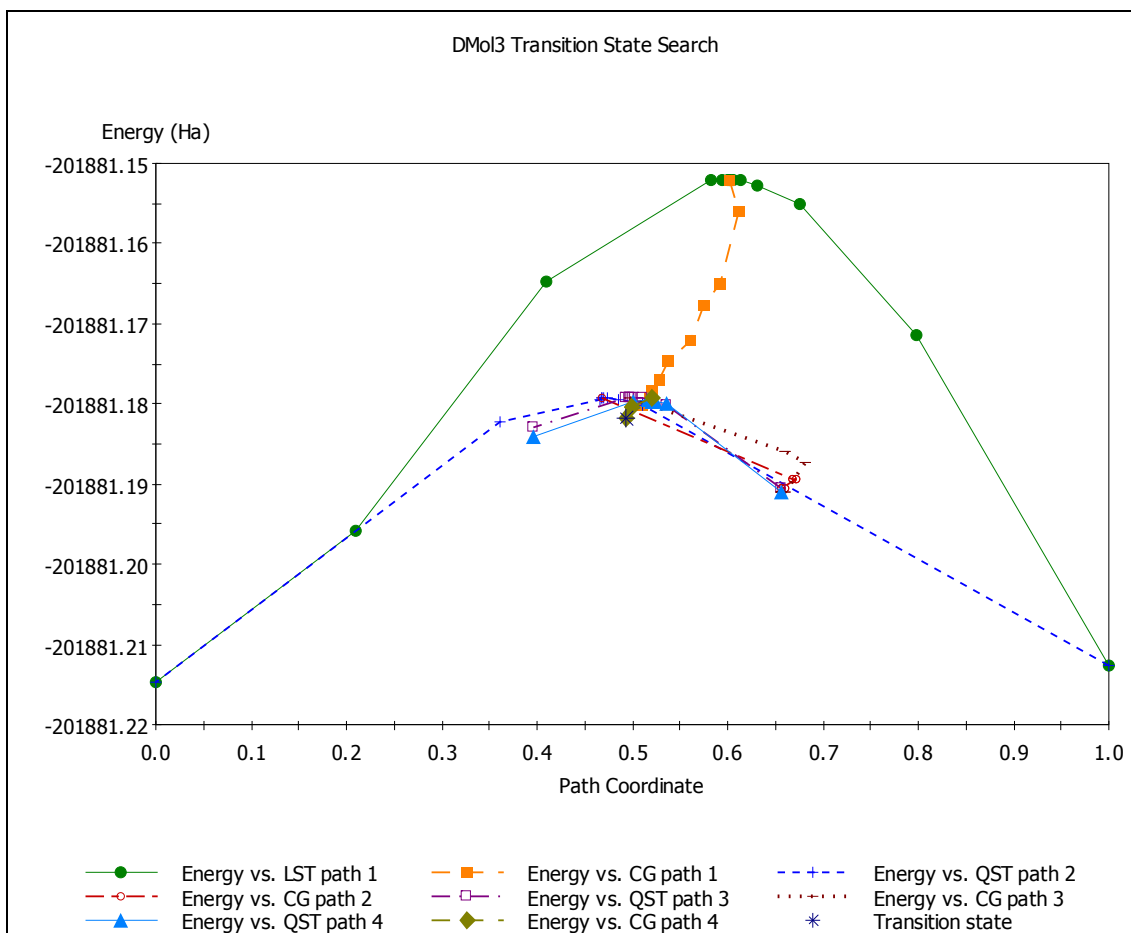


Figure 3.5. A sample energy curve obtained after LST/QST algorithm.

After the TS is determined, TS Confirmation tool can be used to verify that the TS calculated by an LST or QST search connects the reactant and product as expected. MS Modeling automatically determines the reactant, TS and product from the given LST or QST trajectory document. Then, TS optimization determines the stationary points between the TS and the reactant/product, if there are any. The output of a TS confirmation calculation is another trajectory document. This one follows the Intrinsic Reaction Path (IRP). Nudged elastic band (NEB) [83] method is used for minimum energy path calculations. NEB introduces a fictitious spring force that connects neighboring points on the path to ensure continuity of the band. The NEB method implemented in Dmol3 is different from the conventional NEB method in that it does not start from the reactant and the product, but instead starts from the TS and instead of giving the entire reaction

pathway, it only provides the minima in the direction of the reactant and the product. If no minima is found on the IRP other than the estimated reactant and product, then the TS confirmation calculation verifies that the TS does indeed connect the presumed reactant and product. On the other hand, any other minima located by the TS confirmation are the structures that are actually connected by the TS. Then, it is necessary to perform a geometry optimization to refine the geometry of these minima.

3.3. Parameters for Optimization

During the DFT calculations with CASTEP and DMol3, sampling of the Brillouin zones were achieved by summation over Monkhorst-Pack [84] meshes of dimensions 4x4x1 on a (2x2) cell (k-point separation close to 0.025 1/Å) and adjusted accordingly with changes in slab dimensions. Exchange and correlation were included through the use of GGA along with the Perdew-Burke-Ernzerhof (PBE) functional [85].

In CASTEP, electron-ion interaction was included through the use of ultrasoft pseudopotentials. A smearing range of 0.1 eV was applied at the Fermi level and 4 empty bands were introduced to speed up the convergence. Pulay's density mixing scheme was used for the self-consistent field (SCF) electronic minimization. The convergence criteria for structure optimizations were 2.0×10^{-6} eV/atom for SCF, 2.0×10^{-5} eV/atom for energy, 0.05 eV/Å for maximum force, and 2.0×10^{-3} Å for maximum displacement.

In DMol3, AER calculations are performed with double-numeric quality basis set and polarization functions (DNP). DNP basis set includes one atomic orbital for each occupied atomic orbital and a second set of valance orbitals, along with polarization d and p function on all non-hydrogen atoms. A Fermi smearing of 0.002 Ha was used. The smearing option allows the fractional orbital occupancy and improves SCF convergence. The convergence criteria for structure optimizations were 1.0×10^{-5} Ha/atom for SCF, 2.0×10^{-5} Ha for energy, 0.004 Ha for maximum force, and 0.005 Å for maximum displacement. During the TS calculations, the geometry optimization convergence thresholds for the rms forces on the atoms were 0.01 Ha/ Å

3.4. Calculating the Properties

3.4.1. LDOS Charts

Local density of states (LDOS) is a useful semi-qualitative tool for analyzing the electronic structure. LDOS shows which atoms in the system contribute electronic states to various parts of the energy spectrum.

CASTEP uses a simplified linear interpolation scheme for LDOS calculations. This method is based on linear interpolation in parallelepipeds formed by the points of the Monkhorst-Pack set, followed by the histogram sampling of the resultant set of band energies. Smearing method is employed with a width of 0.2 eV. Charts are produced by plotting the LDOS data (electrons/eV) versus energy (eV).

3.4.2. Mulliken Charges

As a result of the numerical basis set of DMol3, molecules can be dissociated accurately to their constituent atoms and thus, basis set superposition effects are minimized. In CASTEP, on the other hand, due to the delocalized nature of plane wave basis set, no information is obtained regarding the localization of the electrons in the system. Population analysis in CASTEP is performed using a projection of the plane wave states onto a localized basis. In both codes, the resulting states are then used to provide the atomic populations with a technique performed using the Mulliken formalism [86]. In the Mulliken analysis, the charge is determined for a given atom A by

$$Q(A) = \sum_k w_k \sum_{\mu}^{\text{onA}} \sum_v P_{\mu v}(k) S_{v\mu}(k), \quad (3.23)$$

where S and P are the overlap and population matrices, respectively and they are defined as,

$$S_{v\mu}(k) = \langle \phi_{\mu}(k) | \phi_v(k) \rangle, \quad (3.24)$$

$$P_{\nu\mu}(\mathbf{k}) = \left\langle \varphi^{\mu}(\mathbf{k}) | \rho(\mathbf{k}) | \varphi^{\nu}(\mathbf{k}) \right\rangle, \quad (3.25)$$

and w is the weight associated with the \mathbf{k} -points in the Brillouin zone.

4. RESULTS AND DISCUSSION

4.1. Effect of Pt Incorporation on the Electronic and Oxygen Chemisorption Properties of Ni Surface

Recent studies has shown that Pt-Ni bimetallic catalyst has better performance in OSR, compared to monometallic Ni [17,87-89], which is mostly related to the oxygen adsorption properties of the active surfaces. Monometallic Ni catalyst is easily oxidized and loses its reforming activity in OSR conditions due the high affinity of Ni towards oxygen. Small amounts of Pt-doping into the Ni catalyst, on the other hand, decreases the tendency of the active sites to be oxidized and supports the surface to stay in the reduced metallic form. As a result, the separation of endothermic and exothermic reaction zones, which is caused by the decreased reforming activity of oxidized zone (especially the reactor inlet), is prevented and a flat temperature profile along the catalyst bed is attained.

Depending on the miscibility of the elements into each other, Pt doping into Ni may result in the formation of separate Pt and Ni phases, random Pt-Ni substitutional alloys or ordered alloys with specific bulk stoichiometry. XRD analysis of Pt-Ni bimetallic OSR catalyst did not indicate any bulk alloy-like formation on the catalyst surface. Instead, changes in Pt:Ni surface ratio was observed with energy dispersive x-ray (EDX) analysis, especially at the close neighborhood of the Pt sites, which may be an indication of the random Pt-Ni surface alloy formation [87]. It should be noted that in those bimetallic catalysts, Ni:Pt ratio changed between 35 and 75 by weight and the catalyst samples were prepared by sequential impregnation, during which Ni was impregnated first and Pt was impregnated onto Ni. In a recent study of Shu et al., it was proven that the sequence of impregnation has a direct influence of the rate of surface alloy formation between Pt and Ni and that the alloy formation is favored when Pt is impregnated onto Ni, rather than Ni impregnated onto Pt [10]. Comparison of co-impregnation and sequential impregnation methods also showed that surface alloy formation is favored at the catalyst prepared with Pt deposition onto Ni and that there is a direct relation between the surface alloy formation and catalytic activity in OSR along a flat temperature profile [17].

In this part of the study, oxygen chemisorption on Pt-Ni surface alloy has been studied with DFT, aiming to shed light on the decreased oxidation tendency of the Ni surface after Pt doping. Varying number of surface Ni atoms were substituted by Pt to model the Pt-Ni surface alloy structures with different stoichiometry. The stabilities of these surface alloy structures were compared based on their surface energies and the changes in the surface energies were explained based on the electronic structure of the surface atoms and the corresponding surface stress. Oxygen adsorption energy was calculated on these surface alloys and compared with the results found for monometallic Pt and Ni surfaces and bulk Ni₃Pt alloy.

4.1.1. Computational Parameters

Spin-polarized density-functional theory calculations were carried out with the program packages CASTEP and DMol3. The surfaces were modeled as five-layer slabs. The uppermost two layers of the slabs were allowed to relax out of plane together with the adsorbate until all the relevant atomic forces were below threshold. The remaining bottom three substrate layers were fixed in their bulk positions. The vacuum thickness between slabs was taken as 14 Å.

Surface energies and oxygen adsorption energies were found with CASTEP, whereas DMol3 was used for analyzing the changes in charge distributions of the atoms. In CASTEP, the electronic wave functions involved were expanded in a basis set of plane waves, up to a kinetic energy cutoff of 300 eV. In order to test the accuracy of cutoff value, 340 eV cutoff value was also used and it was seen that its effect on the oxygen adsorption energy and the surface energy is below 0.02 eV and 0.004 J/m², respectively. In DMol3, a real-space cutoff of 4.5 Å were used.

Ni single crystal surface was modeled by the (111) termination. Surface alloys with different Pt concentrations were created by substituting different number of Ni atoms from the topmost and second layers of the Ni surface by Pt. The pseudomorphic Pt layer over Ni was created by replacing all the topmost surface Ni atoms with Pt. Throughout these studies, the slab dimensions were kept unchanged. The stability of the surfaces were

compared based on their surface energy for both monometallic surfaces and bimetallic surfaces. The surface energy (E_{surf}) was calculated according to the following formula:

$$E_{\text{surf}} = \frac{E^{\text{slab}} - N_{\text{Pt}} E_{\text{Pt}}^{\text{bulk}} - N_{\text{Ni}} E_{\text{Ni}}^{\text{bulk}}}{2A}. \quad (4.1)$$

In the formula, A is the surface area of the unit cell of the slab, E^{slab} is the total energy per unit cell of the slab, E^{bulk} is the total energy per unit cell of the bulk crystal of metal and N is the number of atoms in the unit cell of the slab. The factor 2 reflects the presence of two surfaces in the slab. To calculate oxygen adsorption energy, the following basic formula was used, where E^{O} represents the energy of atomic oxygen:

$$E_{\text{ads}} = E^{\text{slab+adsorbate}} - E^{\text{slab}} - E^{\text{O}}. \quad (4.2)$$

Stress calculations were directly performed with CASTEP. In order to calculate surface stress, stress tensor data was extracted from the output file of CASTEP. Stress tensor has components in x, y and z direction. Since the atoms were free to expand in the z direction through the vacuum, only the data in x and y direction were taken into consideration for this study, and stress was defined as the average value of the two diagonal elements for each surface.

4.1.2. Pt-Ni Surface Alloy Formation and the Electronic Reconstruction at the Surface due to Pt-Ni Interaction

Pt atoms impregnated onto Ni(111) have a tendency to diffuse into the Ni substrate and form Pt-Ni surface alloys: According to DMol3 calculations, there is an energy decrease during the position exchange between a Pt adatom and a surface Ni atom in a (3x3) cell by 0.29 J/m² (Figure 4.1). The magnitude of this exchange energy increases to 0.34 J/m² if the size of Pt clusters over Ni substrate grows to three Pt atoms.

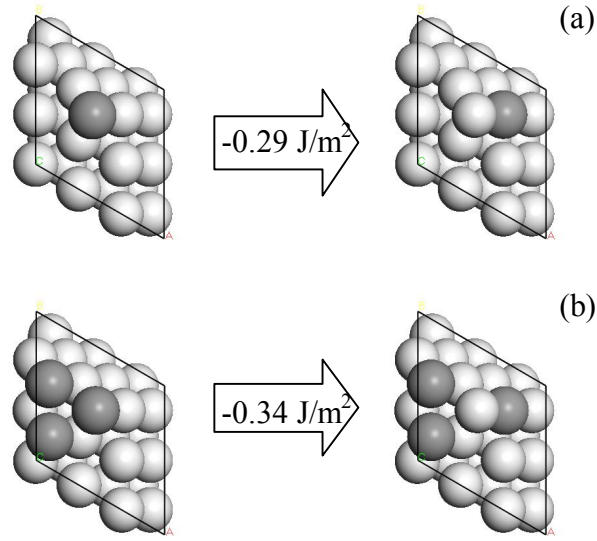


Figure 4.1. Ni-Pt atom exchange. Ni surface atom is substituted by (a) the Pt adatom adsorbed on the Ni substrate (b) one of the Pt atoms from the Pt cluster on the Ni substrate.

The energy of Pt-Ni atom exchange is also given. Dark balls represent Pt, gray ones represent Ni atoms.

In order to keep track the changes in total energy during Pt-Ni atom exchange, the process may be divided into a number of components, as depicted in Figure 4.2. One can write:

$$E_{\text{ads}}(\text{Pt}) = E_{\text{Pt/Ni}}^{\text{slab}} - (E_{\text{Ni}}^{\text{slab}} + E_{\text{Pt}}^{\text{bulk}}), \quad (4.3)$$

$$E_{\text{ads}}(\text{Ni}) = E_{\text{Ni/Pt-Ni}}^{\text{slab}} - (E_{\text{Pt-Ni}}^{\text{slab}} + E_{\text{Ni}}^{\text{bulk}}). \quad (4.4)$$

Subtracting equation (4.3) from equation (4.4),

$$E_{\text{Ni/Pt-Ni}}^{\text{slab}} - E_{\text{Pt/Ni}}^{\text{slab}} = (E_{\text{ads}}(\text{Ni}) - E_{\text{ads}}(\text{Pt})) + ((E_{\text{Pt-Ni}}^{\text{slab}} + E_{\text{Ni}}^{\text{bulk}}) - (E_{\text{Ni}}^{\text{slab}} + E_{\text{Pt}}^{\text{bulk}})), \quad (4.5)$$

where, $E_{\text{ads}}(\text{Pt})$ and $E_{\text{ads}}(\text{Ni})$ are the adsorption energy of Pt and Ni atoms, respectively.

$E_{\text{Pt/Ni}}^{\text{slab}}$ and $E_{\text{Ni/Pt-Ni}}^{\text{slab}}$ are the total energy per unit cell of the slab including the adatom and the substrate. $E_{\text{Ni}}^{\text{slab}}$ and $E_{\text{Pt-Ni}}^{\text{slab}}$ are the energy per unit cell of substrate without the adatom. It

should be noted that the last term in equation (4.5) gives the formation energy of the Pt-Ni substrate from monometallic Ni substrate. Thus,

$$\Delta E = \Delta E_{\text{ads}} + \Delta H_{\text{substrate}}. \quad (4.6)$$

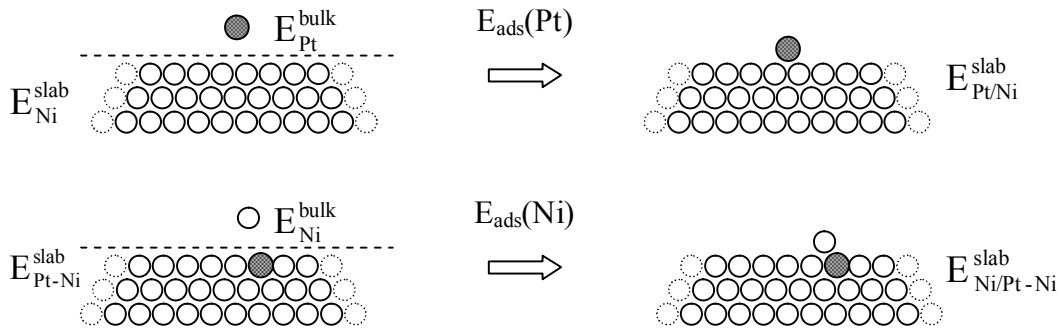


Figure 4.2. Schematic presentation of alloy formation steps. Dark balls represent Pt, gray ones represent Ni atoms.

As seen in Table 4.1, the major part of the exchange energy comes from the term $\Delta H_{\text{substrate}}$, which equals to -0.15 J/m^2 for both of the cases depicted in Figure 4.1. The negative value of $\Delta H_{\text{substrate}}$ means that the substrate is stabilized after the surface Ni atom is substituted by Pt. In order to analyze the reasons of the stabilization in the substrate as a result of Pt substitution, electronic charges of the valance orbitals of surface atoms were analyzed. As given in Table 4.2, Mulliken population analysis shows that Ni valance orbitals donate electrons to Pt valance orbitals during the surface alloy formation. As Pt and Ni are both located at the right hand side of the periodic table and have d-bands more than half of which are full, the s and p orbitals form the bonding orbitals between these metal atoms [62]. Thus, with Ni atoms losing electrons and Pt atoms gaining electrons at the s and p orbitals, one can conclude that Ni-Ni bonding orbitals are weakened at the surface, whereas Pt-Ni bonding orbitals are strengthened. It is known that the strength of lateral metal-metal bonds at the surface of transition metals has a direct influence on surface stress [61,65]. Electronic charges, which are homogeneously distributed in the bulk, are instead concentrated at the lateral bonds of the surface layer and the high electronic population causes an increase in the strength of the lateral metal-metal bonds. Consequently, these bonds tend to contract in x and y directions and a high tensile stress is

produced. On Pt-Ni surface alloys, both the weakened surface Ni-Ni bonds and the strong surface Pt-Ni bonds change the surface stress and affect the stability. This will be further analyzed in the following chapter.

Table 4.1. Energy required for the exchange between a Ni substrate atom and a Pt adatom.

All values are given in J/m^2 .

Structure	$\Delta E_{\text{ads}}(\text{J/m}^2)$	$\Delta H_{\text{substrate}}(\text{J/m}^2)$	$\Delta E(\text{J/m}^2)$
(Pt/Ni \rightarrow Ni/Pt-Ni) ; Figure 4.1 (a)	-0.14	-0.15	-0.29
(3Pt/Ni \rightarrow 2Pt-1Ni/Pt-Ni) ; Figure 4.1 (b)	-0.19	-0.15	-0.34

The energy decrease accompanying the atom exchange is affected by the size of Pt clusters over the Ni substrate. This is depicted in Table 4.1: As the size of Pt ensembles grows on Ni(111), the stability of these clusters decreases. This is related to the size mismatch between Ni and Pt; Pt atoms are compressed compared to their bulk equilibrium dimensions when they are adsorbed over the Ni substrate and Pt-Pt bonds are contracted. This compression increases both the magnitude of energy release during atom exchange and the tendency to form surface alloys between Ni and Pt.

Table 4.2. Charge distribution at valance orbitals of surface metal atoms and changes during surface alloy (SA) formation

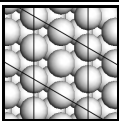
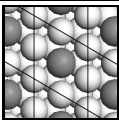
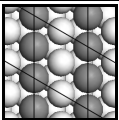
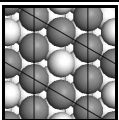
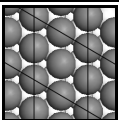
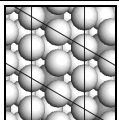
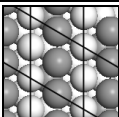
Structure	s	p	d
Ni at surface of Pt_1Ni_8 SA	0.71	0.47	8.72
Ni at surface of Ni(111)	0.76	0.48	8.74
Charge difference at Ni orbitals	-0.05	-0.01	-0.02
Pt at surface of Pt_1Ni_8 SA	1.09	0.77	8.78
Pt at surface of Pt(111)	0.87	0.60	8.53
Charge difference at Pt orbitals	0.22	0.17	0.25

4.1.3. Structure of Stable Surface Alloys

The stability of surface alloys with different Pt concentrations at the surface layers can be compared based on their surface energies. The surface energy values of the structures calculated according to Formula 4.1 and using the energy values obtained with

CASTEP are given in Table 4.3. They are additionally depicted in Figure 4.3. The surface energy of monometallic Ni(111) slab is 1.89 J/m^2 . In previous studies, the surface energy of Ni(111) was reported as 1.77 J/m^2 as calculated with spin polarized DFT [90] and 2.03 J/m^2 as calculated with modified embedded atom method [91]. In this respect, the results of these studies are in agreement with the current results.

Table 4.3. Surface energy (E_{Surf}) and surface stress (S) of Ni(111) and Pt-Ni surface alloys with different Pt concentrations at surface layer I (topmost surface layer) and layer II (second layer). First column gives the top view of stable surface structures: Dark balls represent Pt, light grey ones represent Ni atoms.

	Surface structure	$E_{\text{Surf}} (\text{J/m}^2)$	S (N/m)
	Ni(111)	1.89	1.78
	Ni _{25%Pt-I}	1.70	0.28
	Ni _{50%Pt-I}	1.71	-2.00
	Ni _{75%Pt-I}	1.89	-5.67
	Ni _{100%Pt-I}	2.28	-10.82
	Ni _{25%Pt-II}	1.89	-0.06
	Ni _{50%Pt-I+25%Pt-II}	1.78	-3.38

The results show that the surface energy of a substitutional alloy depends on the Pt concentration at the topmost surface layer. When one single Ni atom is substituted by Pt in a (2x2) cell, resulting in a Pt concentration of 25 per cent at the topmost layer (surface Ni_{25%Pt-I}), surface energy becomes 1.70 J/m^2 . Incorporation of a second Pt to increase the surface concentration to 50 per cent at the topmost layer (surface Ni_{50%Pt-I}) slightly

increases surface energy to 1.71 J/m^2 . An increase in the Pt concentration above 50 per cent further increases the surface energy. Surface energy of one-layer pseudomorphic Pt on Ni(111) is 2.28 J/m^2 (surface $\text{Ni}_{100\%\text{Pt-I}}$), and is higher than the surface energy of both monometallic Ni(111) and Pt(111). To check whether there might be a possibility of a stacking fault at the Pt-Ni interface of the pseudomorphic layer, both fcc and hcp stackings are tested and it is seen that fcc stacking is preferred by 0.01 J/m^2 . Among the possible structures considered in this study, surface $\text{Ni}_{25\%\text{Pt-I}}$ was found to be the most stable one, even when compared to monometallic metals, due to its minimum surface energy.

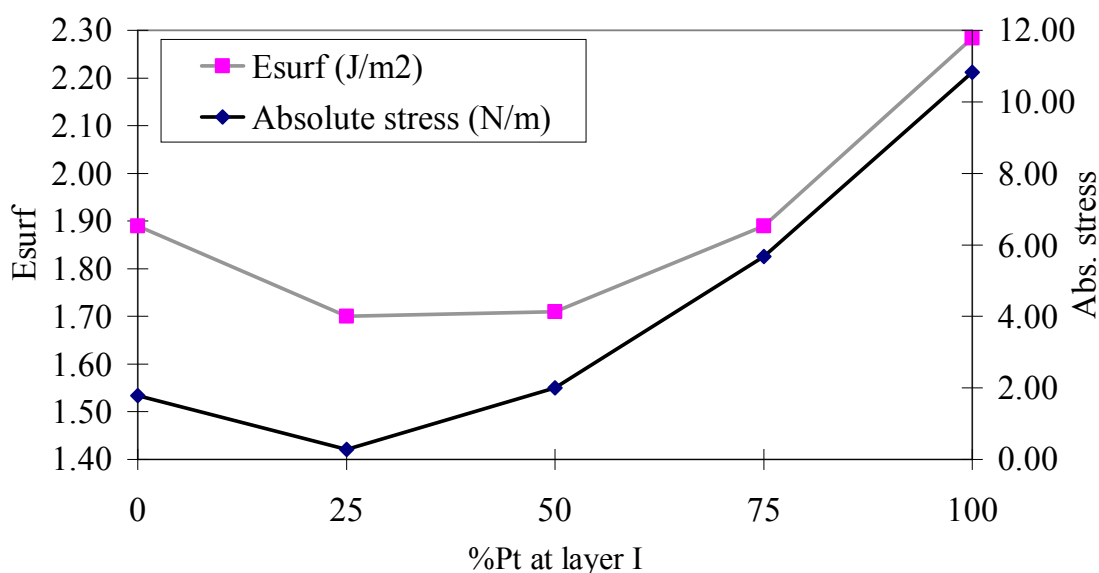


Figure 4.3. Surface energy (E_{Surf}) and stress (in absolute value) changes: Pt concentration at layer I (topmost surface layer) increases from 0 (monometallic Ni surface) to 100 per cent (pseudomorphic Pt layer over Ni).

As proposed before, the electronic reconstruction at the surface changes the surface stress and this is believed to be one of the reasons for the low surface energy and high stability of Pt-Ni surface alloys. In order to prove this, the surface stress values of all structures are calculated and correlated with the surface energy values (Figure 4.3). The surface stress on Ni(111) was found to be 1.78 N/m , the positive value meaning that the surface is indeed under tensile stress (Table 4.3). Surface $\text{Ni}_{25\%\text{Pt-I}}$ has a tensile stress with a value corresponding to 0.28 N/m . Considering that the surface stress effective on surface $\text{Ni}_{25\%\text{Pt-I}}$ is nearly zero and that this alloy structure has also the minimum surface energy among all the alloy structures tested in this study, it was concluded that the stability of the

structures are affected by stress changes on the surface. Beyond 25 per cent Pt concentration, Pt incorporation leads to compression and thus the stress value turns into negative. A full pseudomorphic layer of Pt on Ni(111) is found to be under an excessive compressive stress with a magnitude of -10.82 N/m. This leads to a surface reconstruction during which some of the Pt atoms protrude slightly up from the surface layer thus reducing the compression.

The dependence of surface stress on the difference between the radii of the elements in bimetallic systems was previously shown by DFT calculations on a variety of metals [92]. Substitute atoms with a larger metallic radii than the substrate reduce the tensile stress, whereas the opposite was shown in the case of smaller Cu atoms alloying larger W(100) surface atoms. In this respect, the decrease in the tensile stress of Ni substrate when alloyed with Pt is logical: The equilibrium lattice constants of Ni and Pt are 3.55 and 4.00 Å, respectively, and the corresponding metal-metal bond lengths are 2.51 and 2.83 Å for the two metals in bulk. When Ni is alloyed with Pt, the compression caused by the difference in the equilibrium bond lengths requires a rearrangement during which Pt-Ni bonds are lengthened by pushing the Pt atoms out of the surface plane and causing a surface rumpling (Figure 4.4). In the case of surface Ni_{25%Pt-I}, Pt atoms protrude out of the surface by 0.13 Å with respect to the other surface Ni atoms and this results in a Pt-Ni bond length equal to 2.52 Å, which is slightly longer than the equilibrium Ni-Ni bond length on pure Ni(111).

The probability of Pt dissolution into the Ni bulk and stability of subsurface Pt in Ni substrate are also checked by analyzing the surface energy of Pt-Ni surface alloys with Pt atoms substituting the second layer Ni atoms. It was found that at low Pt concentrations, Pt atoms prefer to reside in the topmost surface layer: The surface energy of Ni_{25%Pt-I} and Ni_{25%Pt-II} is 1.70 and 1.89 J/m², respectively, as seen in Table 4.3. However, as Pt concentrations increase, the excessive compression on the surface layer may result in the dissolution of some Pt atoms in the bulk. The surface energies of Ni_{75%Pt-I} and Ni_{50%Pt-I+25%Pt-II} 1.89 and 1.78 J/m², respectively. That means when the surface Pt concentration reaches 75 per cent, some of the Pt atoms tend to diffuse to the second layer, decreasing the surface Pt concentration. This diffusion relieves compression at the same time and

surface stress increases from -5.67 to -3.38 N/m. Apart from the excessive compression in the surface layer, there is no driving force that may lead to Pt dissolving in Ni substrate.

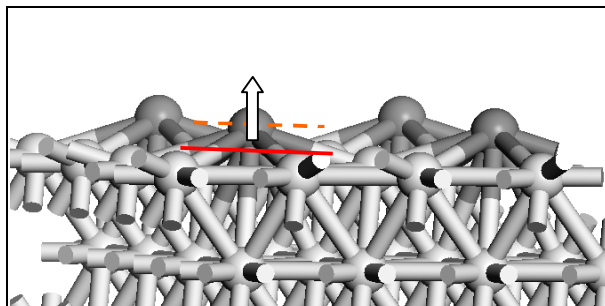


Figure 4.4. Pt protrusion from Ni(111) surface. Dark balls represent Pt, gray ones represent Ni atoms.

As a final remark, as a part of our forthcoming study, Pt substitution into the stepped Ni(211) substrate was analyzed and it was found that the surface energy decreases by an amount as high as 0.14 J/m^2 with Pt-Ni surface alloy formation. It was proposed that the reforming reaction proceeds mainly on step sites and the step density dominates the reaction rate [93]. DFT calculations on Ni(111) and Ni(211) also showed that activation barriers at the step sites of Ni(211) surface are lower than those on the flat (111) surface termination, suggesting that step sites may be the dominant active sites in the reforming reaction [14]. By means of an energy decrease, Pt-Ni mixing favors the formation of stepped structures, which might have a positive effect in the catalytic activity in OSR. However, the involvement of Pt presence in the reaction mechanism should be carefully scrutinized before making a decision at that point.

4.1.4. Oxygen Adsorption

The most stable sites for oxygen adsorption on different surface structures are reported in Table 4.4. It was found that oxygen adsorption is most stable on fcc_{Ni3} site of Ni(111), with an adsorption energy of -5.03 eV. The other possible three-fold adsorption site, hcp_{Ni3} , although not shown in Table 4.4, has a close adsorption energy but still higher than the most stable site by 0.10 eV. The experimentally calculated O adsorption energy on Ni(111) was reported as -4.87 eV [94], which is close to what has been calculated here. The calculated O-Ni bond length is also close to what had been determined experimentally

[95]. The calculated adsorption energy on fcc_{Ni3} site of monometallic Pt(111) surface, on the other hand, is -3.82 eV, higher by 1.21 eV than that on Ni(111).

The reason of difference between Pt and Ni adsorption properties is related to the chemical nature of O bonding. The bond between O and substrate metal constitutes of an ionic and a covalent part [96]. Ionic bond is essentially an electrostatic interaction and based on the charge transfer from metal to O. The higher work function of Pt causes a decrease in electron transfer rate from metal to oxygen [97] and decreases the adsorption energy. Mulliken population analysis shows that the total negative charge on O adatom is 0.48 and 0.54 e on Pt(111) and Ni(111), respectively (Table 4.4), which confirms the theory. According to Hammer and Norskov [56], the covalent bond strength is dependent on the d-band structure of the surface metal atom. The d-band extension at Pt is wider than at Ni and the center of d-band is at a lower energy value for Pt compared to Ni (Figure 4.5). This results in an increased interaction of oxygen orbitals with metal d-band at Pt and correspondingly, an increased rate in filling of the anti-bonding states between the metal and oxygen orbitals, which thus decreases O binding energy on Pt compared to that on Ni.

Adsorption on surface alloys is studied on a number of different available surface sites (Figure 4.6). The most available site, based on the assumption that Ni content is higher at the catalyst than Pt, is Ni sites, which constitute only Ni atoms in the neighborhood of Pt. The second possible option is mixed Pt-Ni sites, on which O is bonded to both Ni and Pt atoms. The availability of these mixed sites is higher in the case of larger Pt content or better dissolution of Pt in Ni. Additionally, these sites may play a more active role when the surface oxygen coverage is increased on the surface. For the regions at which Pt atoms form clusters over Ni substrate, adsorption site only constitutes Pt atoms over Ni substrate. Finally, there is the possibility of a presence of Pt at the second layer, under the adsorption site.

The results showed that O adsorption is weakened due to surface alloy formation even when adsorption occurs on Ni sites and Pt is not directly involved in the bonding. The adsorption energy on fcc_{Ni3} of surface $\text{Ni}_{25\%}\text{Pt-I}$ is -4.61, that is 0.42 eV higher than the adsorption energy on monometallic Ni(111). Mulliken population analysis showed that the charge transferred from the metal to O adatom is decreased, as shown in Table 4.4 and

Figure 4.7. Similar to that on Ni sites, it was also found for Pt-Ni mixed sites that as the charge transfer rate decreases, the adsorption energy gets higher. Results indicated that as a general rule for all adsorption sites, there is an almost perfect linear relation between the amount of electrons donated from the surface to oxygen adatom and the adsorption energy, which proves the influence of ionic interaction on the adsorption strength.

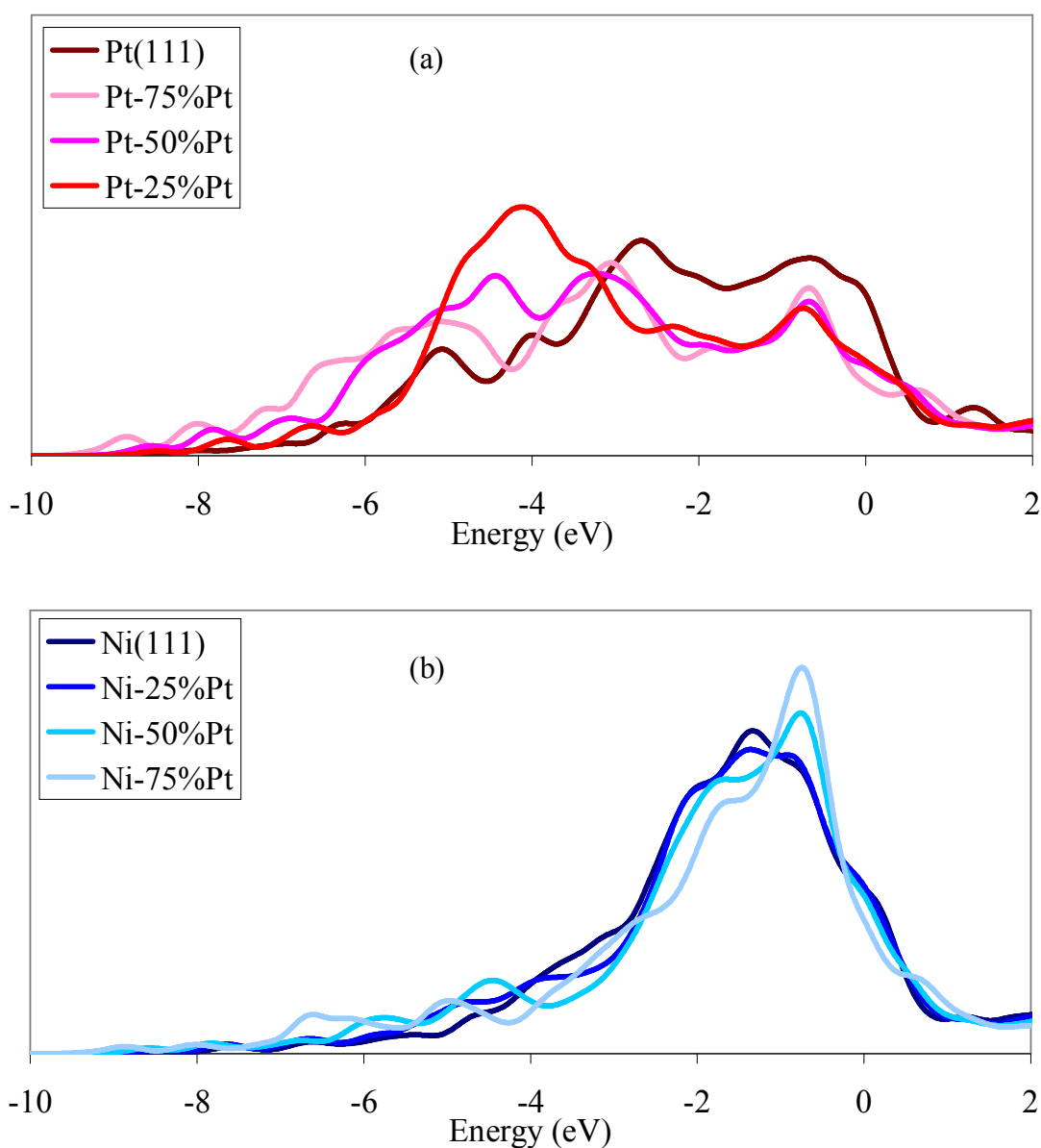
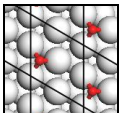
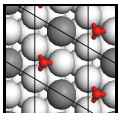
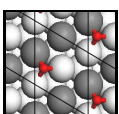
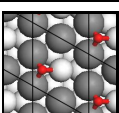
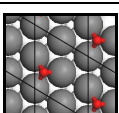
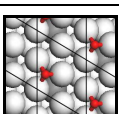
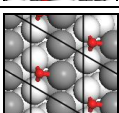
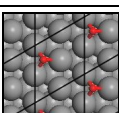
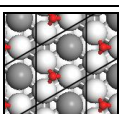


Figure 4.5. LDOS at (a) surface Pt atom (b) surface Ni atom. Surface structures are monometallic Ni(111), monometallic Pt(111), and Pt-Ni surface alloys with Pt concentration at the topmost layer ranging from 25 to 75 per cent.

Table 4.4. Oxygen adsorption energy (E_{ads}) of the most stable three-fold (fcc) hollow site of surfaces with different Pt concentrations, charge transferred to O during chemisorption, (q) the final stress after chemisorption (S') and related oxygen-metal (O-M) bond lengths (r) at adsorption structure

	adsorption site	E_{ads} (eV)	q(O)	S' (N/m)	$r_{\text{O-M(Ni,Pt)}}(\text{\AA})$
	$\text{fcc}_{\text{Ni3}} - \text{Ni}(111)$	-5.03	0.54	0.93	1.85;1.85;1.85
	$\text{fcc}_{\text{Ni3}} - \text{surface Ni}_{25\%}\text{Pt-I}$	-4.61	0.52	-0.76	1.86;1.86;1.86
	$\text{fcc}_{\text{Ni2Pt}} - \text{surface Ni}_{50\%}\text{Pt-I}$	-3.83	0.50	-3.29	1.88;1.87;2.09
	$\text{fcc}_{\text{NiPt2}} - \text{surface Ni}_{75\%}\text{Pt-I}$	-3.11	0.48	-5.50	1.90;2.06;2.14
	$\text{fcc}_{\text{Pt3}} - \text{surface Ni}_{100\%}\text{Pt-I}$	-3.35	0.47	-3.07	2.31;2.05;2.03
	$\text{fcc}_{\text{Ni3}} - \text{surface Ni}_{25\%}\text{Pt-II}$	-5.06	0.54	-1.00	1.85;1.85;1.86
	$\text{fcc}_{\text{Ni2Pt}} - \text{Ni}_{50\%}\text{Pt-I} + 25\%\text{Pt-II}$	-3.93	0.50	-3.50	1.90;1.85;2.06
	$\text{fcc}_{\text{Pt3}} - \text{Pt}(111)$	-3.82	0.48	3.20	2.07;2.07;2.08
	$\text{fcc}_{\text{Ni3}} - \text{surface Ni}_3\text{Pt}(111)$	-4.98	0.53	0.80	1.85;1.85;1.85

The only exception to the linearity between the charge transferred from the metal to O and the adsorption energy is obtained with the surface $\text{Ni}_{100\%}\text{Pt-I}$. Adsorption on fcc_{Pt3} site of this Pt pseudomorphic layer has a smaller adsorption energy than expected from the trend in Figure 4.7. The reason of this inconsistency is most probably related to the initial high surface energy of the surface $\text{Ni}_{100\%}\text{Pt-I}$ and its instability which results in a total

reconstruction during O adsorption. Because of this reconstruction, the final adsorption site on Pt pseudomorphic layer can not be called fcc_{Pt3} anymore. It should be noted that this instability of Pt layers over the Ni(111) substrate increases with the thickness of Pt layers. Although not shown here, it was found that as the thickness of Pt layers increase, the compressive surface stress also increases. As a result, the magnitude of reconstruction and energy relief during O adsorption increase and finally, the adsorption energy gets very small on these reconstructed surfaces.

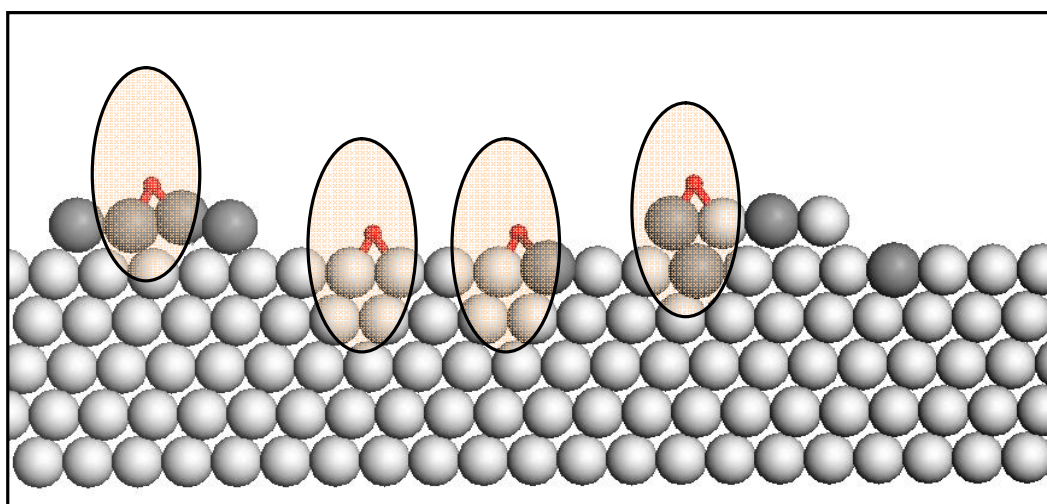


Figure 4.6. Possible oxygen chemisorption sites formed after Pt deposition onto Ni substrate: Pt cluster over Ni, pure Ni site near Pt neighbors, Pt-Ni mixed site, site with Pt atoms in second layer. Dark balls represent Pt, gray ones represent Ni atoms.

However, it should be noted that in calculations of the surface stress of an epitaxial Pt layer over Ni(111) substrate, a perfectly ordered and an infinite layer of Pt over Ni was assumed. Possible dislocations in the Pt layer, which are highly probable in reality, may serve as local relief points by which the excessive compression on the surface is decreased. In this way, chemisorption on Pt layers might be stable structures without atomic reconstructions. However, even these irregular structures would be expected to be under compressive strain and the effect of compressive strain on oxygen adsorption would be similar to what is reported here.

Oxygen adsorption calculations on sites with a Pt at the second layer, under the adsorption site showed that oxygen adsorption may be a driving force that leads to Pt

diffusion from topmost surface layer into the second layer or deeper into the bulk. For instance, comparison of total energies of surface $\text{Ni}_{75\%}\text{Pt-I}$ and surface $\text{Ni}_{50\%}\text{Pt-I}+25\%\text{Pt-II}$ during O adsorption has shown that there is an energy gain by 0.41 J/m^2 for adsorption induced Pt diffusion from the topmost layer into the second layer for surface $\text{Ni}_{75\%}\text{Pt-I}$. Menning et al. also proved on Pt-Ni system by high-resolution electron energy loss spectroscopy (HREELS) and AES analysis that there is an adsorption-induced surface segregation of Ni from subsurface layers to the surface during O adsorption [98]. Jelic and Meyer showed on Pt/Au films that there is a tendency at larger Au atoms to segregate to the surface whereas this is reversed and Pt atoms prefer to reside on the top during O adsorption [99]. Oxygen adsorption energies on a number of sites with a Pt atom at the second layer showed that the presence of Pt does not affect the adsorption energy in a large extent, but slightly decreases it, as seen in Table 4.4. For instance, adsorption energy is -5.06 on $\text{Ni}_{25\%}\text{Pt-II}$, that is 0.03 eV smaller than that on monometallic Ni.

4.1.5. Stress-induced Oxygen Adsorption

Apart from the electronegativity of the metal, local strain fields at a catalytic surface are also known to be effective on the oxygen chemisorption energy. In an experimental study on Ru(0001) by Gsell et al. [100], it was shown with STM analysis of the surface that oxygen adsorption preferably occurs on local strain fields (produced by subsurface Ar gas bubbles) where tensile strain prevails, and are depleted at the regions, around the rim of protrusions created by Ar bubbles, where compression dominates relative to the flat surface.

As surface stress is effective on the adsorption properties of metal surfaces, oxygen adsorption itself is a process accompanied by a change in the surface stress. Bonds between oxygen and metal substitute the missing bonds of the undercoordinated surface metal atoms and thus result in a more homogeneous electron distribution, similar to that within the bulk, and decrease surface stress, as proposed by Fiebelman for O and H chemisorption on Pt(111) surface [65]. Additionally, as oxygen is a highly electronegative adsorbate, it draws electrons and depletes the bond-population at lateral metal-metal bonds further. Mulliken analysis of the surface Ni atoms before and after O adsorption shows that

there is an electron transfer especially from Ni s orbital to oxygen p orbital during the chemisorption.

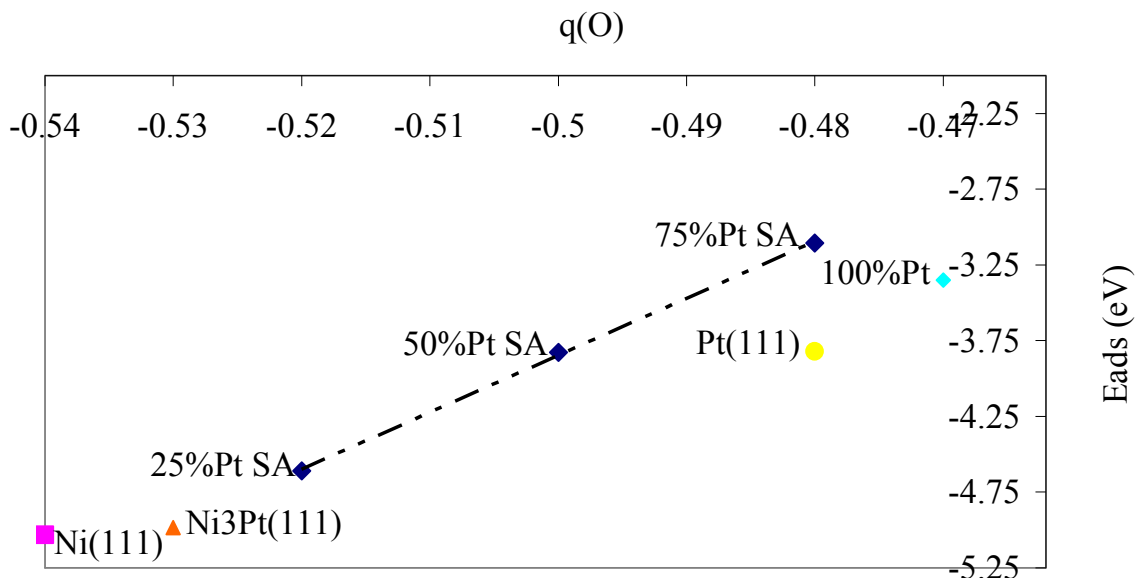


Figure 4.7. The change in oxygen chemisorption energy with the total charge transferred from metal surface to O atom (q). Adsorbate surfaces are monometallic Ni(111), monometallic Pt(111), bulk Ni₃Pt alloy, and Pt-Ni surface alloys (SA) with Pt concentration at the topmost layer ranging from 25 to 100 per cent.

For this reason, on monometallic Ni(111) surface which is under the effect of tensile stress, oxygen chemisorption and the accompanying stress decrease lead to a stable chemisorption structure. Additionally on bulk Ni₃Pt(111) alloy surface, which is also under a tensile stress with a magnitude of 1.81 N/m, oxygen chemisorption leads to a stable structure and the oxygen adsorption energy, which is -4.98 eV, is nearly as high as that on monometallic Ni(111). On surface alloys, on the other hand, the chemisorption leads to an excessive compression on the surface (Table 4.4) and the electron deficient s and p orbitals of the Ni atoms render the electron donation capacity of Ni atoms to oxygen adatoms, decreasing the chemisorption stability. In some cases, especially at surface alloys with high Pt concentrations, the compression created during adsorption may reach such excessive values that Pt diffusion from topmost surface layer to the second layer becomes possible.

Along with the chemical changes effective on Ni atoms, Pt atoms are also influenced electronically and chemically by surface stress. On mixed Pt-Ni adsorption sites, weaker

(and longer, as seen in Table 4.4) Pt-O bonds substitute the stronger Ni-O bonds. For instance, there is a difference in the adsorption energy of oxygen on the $\text{fcc}_{\text{Ni}3}$ and $\text{fcc}_{\text{Ni}2\text{Pt}}$ sites of surface $\text{Ni}_{25\%\text{Pt-I}}$; the former being more stable by 0.35 eV, because of the replacement of one Ni-O bond by Pt-O. The major reason of the difference in Pt-O and Ni-O bond strengths is the difference in the workfunction of the two metals as mentioned before. Additionally, the compression effective on the surface alloys causes an electronic reconstruction at Pt atoms, which further weakens the Pt-O bonds in a covalent way. The electronic reconstruction has similarities with that observed on monometallic Pt(111) surface after it is exposed to compression [101]: a great portion of valance electrons at Pt surface atoms are shifted to lower values, and the center of d-band is pushed far away from the Fermi energy. Xu et al. had found that this compressive strain on Pt(111) destabilizes the adsorption of atomic oxygen [69]. As seen in the LDOS curve of surface Pt atoms (Figure 4.5), this widening and shift in the Pt-LDOS is proportional to the surface Pt concentration and to the compression at the surface. As a result of this compression-induced electronic reconstruction at Pt atoms, the adsorption energy on site $\text{fcc}_{\text{Pt}3}$ of surface $\text{Ni}_{100\%\text{Pt-I}}$ is higher than the adsorption energy on $\text{fcc}_{\text{Pt}3}$ of Pt(111) surface by 0.47 eV.

4.1.6. Summary

The changes in the properties of Ni(111) surface led by Pt substitution and the resulting decrease in oxygen chemisorption stability upon Pt-Ni surface alloy formation were investigated. It was shown that Pt-Ni surface alloy formation is energetically favored on the Ni(111) surface, based on the fact that Pt substitution decreases both the total energy and the tensile stress effective on the surface. The decrease in surface stress leads to a decrease in the rate of electron transfer from the surface Ni atoms to oxygen and, as a consequence, to a weakened oxygen chemisorption stability on the surface. The overall results confirm that Pt-Ni surface alloys have a higher tendency to stay in metallic form, compared to monometallic Ni, and this is one of the reasons of increased catalytic activity and enhanced stability of Pt-Ni bimetallic catalyst in OSR especially at low reaction temperatures.

4.2. Oxidative Steam Reforming Reaction on Pt-Ni Surface Alloy: A Comparison with Monometallic Ni

Small amounts of Pt incorporated into Ni forming Pt-Ni surface alloys either supports the surface to stay in metallic form or leads to easy reduction of NiO to metallic form during oxidative steam reforming (OSR) of methane. It has been proposed that Pt atoms in Pt-Ni surface alloys act as special sites forming an alternative reaction pathway for dehydrogenation of CH₄, which involves the reduction of oxidized NiO species via hydrogen spillover and that promotes the stable activity of the Ni sites during the reforming of methane at lower temperatures [102]. In this respect, dehydrogenation of methane is of crucial importance for the sustainability of the catalytic activity in methane OSR.

Additionally, CH₄ dehydrogenation is the first elementary step in the overall methane steam reforming mechanism. Previous experimental kinetics studies showed that activation of C-H bond in CH₄ and the dehydrogenation reaction are the rate determining steps in methane SR reaction [11,103]. Computational methods also confirmed that CH₄ dehydrogenation has the highest activation energy [104]. Thus, methane dehydrogenation itself has a dominant effect on the overall rate of SR reaction.

In this part of the work, dehydrogenation reaction of methane has been studied on Pt-Ni surface alloys via utilizing DFT. The reaction mechanism was found on both monometallic Ni(111) surface and Pt-Ni surface alloys having trace amounts of Pt incorporated into Ni(111) surface. The activation energy and the heat of reaction were computed and the results were analyzed based on the electronic structure of the surface and the calculated adsorption energies of the products, that are CH₃ and H. The effect of relativistic effects on the electronic structure of Pt-Ni surface alloy has also been analyzed briefly.

4.2.1. Calculational Parameters

Spin-polarized density-functional theory calculations were carried out with the program package DMol3. The surfaces were modelled as five-layer slabs. The uppermost

two layers of the slabs were allowed to relax out of plane together with the adsorbate until all the relevant atomic forces were below threshold. The remaining bottom three substrate layers were fixed in their bulk positions. The vacuum thickness between slabs was taken as 12 Å. A real-space cutoff of 4.5 Å was used.

Ni single crystal surface was modelled by the (111) termination. Surface alloys with different Pt concentrations were created by substituting different number of Ni atoms from the topmost layer of the Ni surface by Pt. Throughout these studies, the slab dimensions were kept unchanged. The stability of the surfaces were compared based on their surface energy for both monometallic surfaces and bimetallic surfaces. The surface energy (E_{surf}) was calculated according to the following formula:

$$E_{\text{surf}} = \frac{E^{\text{slab}} - N_{\text{Pt}} E_{\text{Pt}}^{\text{bulk}} - N_{\text{Ni}} E_{\text{Ni}}^{\text{bulk}}}{2A}. \quad (4.7)$$

In the formula, A is the surface area of the unit cell of the slab, E^{slab} is the total energy per unit cell of the slab, E^{bulk} is the total energy per unit cell of the bulk crystal of metal and N is the number of atoms in the unit cell of the slab. The factor 2 reflects the presence of two surfaces in the slab.

The adsorption energies were calculated using the following basic formula, where $E^{\text{adsorbate}}$ represents the energy of molecule in the gas phase:

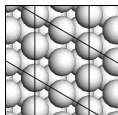
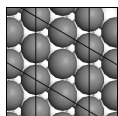
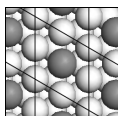
$$E_{\text{ads}} = E^{\text{slab+adsorbate}} - E^{\text{slab}} - E^{\text{adsorbate}}. \quad (4.8)$$

4.2.2. Pt-Ni Surface Alloy Formation

Incorporation of Pt atoms into Ni(111) decreases the surface energy of the system and thus increases its stability. The magnitude of this decrease is 0.17 J/m² with 25 per cent Pt concentration at the surface (Table 4.5). It is found that relativistic effects promote this energy decrease. When the relativistic effects are excluded from the basis sets during the calculations, the surface energy slightly increases from 1.90 J/m² to 1.99 J/m² as a result of surface alloy formation having the same Pt concentration.

Relativistic effects also have an influence on the surface energy of (111) terminations of both Ni and Pt metals in their monometallic form (Table 4.5). While exclusion of relativistic effects decreases surface energy of Ni(111) from 2.07 to 1.98 J/m², the effect is more pronounced in Pt(111), for which the surface energy decreases from 1.66 to 1.31 J/m². The crystal size of Pt increases from 3.91 to 4.19 Å with the exclusion of relativistic effects in the basis set. On Ni, this exclusion causes an increase in Ni crystal size from 3.53 to 3.56 Å. The decrease in surface energy of single crystal metal surfaces and the increase in the crystal size can be tracked down from the changes in the electronic charge distribution at the surface atoms of these two metal atoms.

Table 4.5. Surface energy (E_{Surf}) Ni(111), Pt(111) and Pt-Ni surface alloys with 25 per cent Pt concentration at topmost surface layer. Calculations are performed with two different basis sets: (i) including relativistic effects (AER) and excluding relativistic effects (AE). First column gives the top view of stable surface structures: Dark, big balls represent Pt, small, grey ones represent Ni atoms.

	Surface structure	$E_{\text{Surf-AER}} \text{ (J/m}^2\text{)}$	$E_{\text{Surf-AE}} \text{ (J/m}^2\text{)}$
	Ni(111)	2.07	1.98
	Pt(111)	1.66	1.31
	Ni(111)-25%Pt	1.90	1.99

Relativistic effects increase the charge density of s and p orbitals and decrease the charge density of valance d orbitals, as seen in Table 4.6, for both Pt(111) and Ni(111) surface atoms. This charge redistribution is a result of energy shift of s and p orbitals. Relativistic effects decrease the energy of valance s and p orbitals of metal atoms and led by this contraction in the s and p orbitals, the shielding of the nucleus is increased and, valance d orbital is shifted to higher energies. As a result, electrons are more populated at lower energy s and p orbitals compared to d orbital. The s and p orbitals are the bonding orbitals of both Ni and Pt, whereas the nearly-full d-orbital is the antibonding orbital. Thus, the pre-mentioned increase in the electron density of s and p orbitals and the accompanying

decrease in d orbitals cause an increase in the strength of metal-metal bonds of these two monometallic crystals and results in a decrease in the crystal size of Pt and Ni.

In the case of the surface, the electronic distribution at undercoordinated surface atoms of monometallic Pt and Ni metals leads to especially stronger lateral metal-metal bonds, for which the excessive electrons that are not homogeneously distributed as in the bulk are used to increase the strength of these bonds. Stronger bonds lead to a large tensile stress on the surface and a decrease in the surface stability. As inclusion of relativistic effects during the calculations was shown to increase the strength of bonding orbitals between metals, it is highly probable that the higher surface energy obtained from these calculations is directly related to the large tensile stress effective for both monometallic surfaces. Similarly, exclusion of relativistic effects decreases the electron population of s and p bonding orbitals and increases the antibonding d-orbital occupation; by this way, both the surface energy of the system and the tensile stress decrease in a coupled fashion.

Table 4.6. Charge distribution at valance orbitals of surface metal atoms and changes during surface alloy formation. Calculations are performed with two different basis sets: (i) including relativistic effects (AER) and excluding relativistic effects (AE).

	With AER			With AE		
	s	p	d	s	p	d
Ni(111) - Ni	0.76	0.48	8.74	0.75	0.45	8.78
Ni(111)-25%Pt – Ni	0.65	0.47	8.71	0.71	0.44	8.78
Charge difference	-0.11	-0.01	-0.03	-0.04	-0.01	0.00
Pt(111) - Pt	0.87	0.60	8.53	0.58	0.27	9.14
Ni(111)-25%Pt – Pt	1.10	0.80	8.76	0.63	0.46	9.18
Charge difference	0.23	0.20	0.23	0.05	0.19	0.04

As can be seen at the LDOS graph of Pt and Ni surface atoms, Pt valance orbitals are at a lower energy value than Ni valance orbitals (Figure 4.8). For this reason, alloy formation is accompanied by a charge transfer from Ni to Pt. As can be seen in Table 4.6, there is hybridization especially between the s orbitals. In section 4.1, it has been shown that accompanying this charge redistribution, tensile stress is also decreased on the surface and that the trend in the surface energies of Pt-Ni surface alloys with different

stoichiometries is closely related to the surface stress. The calculations here has shown that relativistic effects again play an important role on the charge transfer between Ni and Pt orbitals and that s orbital hybridization is greatly hindered when relativistic effects are excluded from the basis sets defining the system. As a result, the surface energy is increased. It was also shown in a previous study that Ni-Pt mixing and homogeneous Ni-Pt surface alloy formation is easier than Ni-Pd mixing since the relativistic effects are more pronounced on heavier Pt atom and its electronic structure, compared to those on Pd [105]. This surface energy increase as a result of alloy formation when the relativistic effects are excluded from basis sets is most probably due to excessive compression created with the insertion of a metal with a larger radius than Ni. Indeed, when the surface relaxation values are analyzed, it is seen that Pt atoms protrude out of the Ni surface layer by 0.37 Å although a flat surface profile is obtained with AER calculations. This surface corrugation is an indirect evidence of excessive compression.

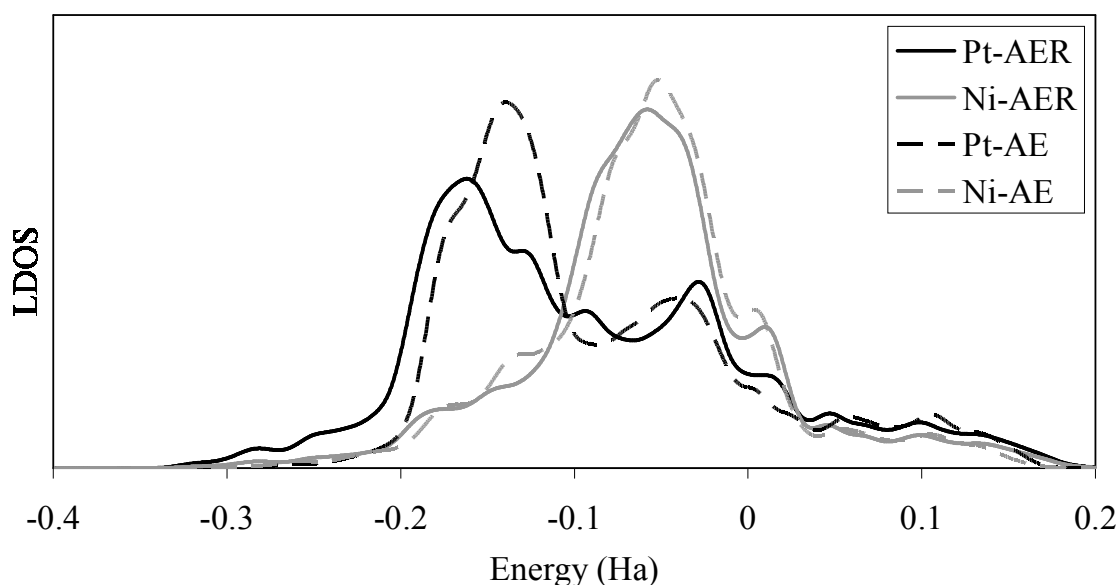


Figure 4.8. LDOS at surface Pt and Ni atoms of Pt-Ni surface alloy. Calculations are performed with two different basis sets: (i) including relativistic effects (AER) and (ii) excluding relativistic effects (AE).

4.2.3. Adsorption of Reactants and Products

CH₄ is a very stable compound and thus, dissociation of CH₄ in the gas phase is a very endothermic reaction. On metal surface, however, strong CH₃-metal and H-metal

bonds make the progress of the reaction easier. The adsorption of reactants and products is a crucial mechanistic step in the overall reaction path. Based on the Bronsted, Evans, Polanyi (BEP) relationship, the adsorption energies of the reactants and products play an essential role in the activation of the reaction [106,107]. Thus, the possible adsorption sites for CH₄, H and CH₃ and the adsorption energies are all calculated, as the starting point of this study. The results are given in Table 4.7.

Table 4.7. Energy of CH₃ and H adsorption and CH₃+H coadsorption on Ni(111) and Pt-Ni surface alloy (SA).

Adsorption site	E_{ads}(CH₃) (eV)		E_{ads}(H) (eV)		E_{ads}(CH₃ + H) (eV)	
	Ni(111)	SA-25%Pt	Ni(111)	SA-25%Pt	Ni(111)	SA-11%Pt
atop _{Ni} p(2x2)	-1.79	-1.68	-2.35	-2.22	-	-
fcc _{Ni3} p(2x2)	-1.90	-1.66	-2.76	-2.60	-	-
hcp _{Ni3} p(2x2)	-1.85	-1.61	-2.70	-2.55	-	-
atop _{Pt} p(2x2)	-	-2.03	-	-2.82	-	-
fcc _{Ni2Pt} p(2x2)	-	unstable	-	-2.69	-	-
hcp _{Ni2Pt} p(2x2)	-	unstable	-	-2.68	-	-
hcp+fcc p(3x3)	-	-	-	-	-4.63	-4.52
atop _{Pt} +fcc p(3x3)	-	-	-	-	-	-4.73
atop _{Pt} +hcp p(3x3)	-	-	-	-	-	-4.68

CH₄ physically adsorbs on flat Ni(111) surface. The adsorption energy of CH₄ on Ni(111) and Pt-Ni(111) are found to be between -0.03 eV and -0.05 eV and are in accordance with the literature [108]. The relation between the adsorption site and the adsorption energy is not so pronounced. Additionally, Haroun et al. had calculated that the activation energy of the dehydrogenation reaction is not influenced by whether the CH₄ enters the reaction from the physisorbed state or the gas phase [108]. Similarly, CH₄ adsorption energy ranges between -0.3 and -0.4 eV on the Pt-Ni surface alloy, which means adsorption is also in the physisorption range.

It can be expected that adsorption structure of methyl would be linear on transition metals as a general rule, considering the resemblance of its tetrahedral structure to the CH₄. However, CH₃ tends to adsorb on a three-fold hollow site on Ni(111), as proved by

HREELS analysis [109]. This is also confirmed by recent computational studies [110-112]. The adsorption energy of the fcc and hcp sites are -1.90 eV and -1.85 at 0.25 ML in a p(2x2) cell, as seen in Table 4.7. On the Pt-Ni surface alloy, on the other hand, linear adsorption on the Pt atom is energetically favorable. This is similar to adsorption process of CH₃ on monometallic Pt(111) surface, for which computational studies had again shown the preference of the top-site [113-115]. The adsorption energy of CH₃ on Pt-Ni surface alloy is found to be -2.03 eV, which is higher than the adsorption energy found for monometallic Ni(111).

Previous DFT studies had shown that on Ni(111), the main contribution to the bonding between methyl and the metal comes from the interaction between the HOMO of CH₃, that is 3a₁ orbital, and Ni-3d states; however the preference of multifold site over atop site for adsorption comes from the difference in the degree of interaction between the two other orbitals of CH₃, namely 1e, which is next to the 3a₁ orbital in energy, and 2a₁, which is the lowest energy orbital of CH₃ in interaction with Ni-d states [112]. It was also proposed that LUMO of CH₃, which is the antibonding orbital of the bond between C and H, also plays a role in the CH₃ adsorption strength on Ni [111], as the bond length between C and H changes during adsorption.

In order to understand the difference in the adsorption of methyl on Ni(111) and on Pt-Ni surface alloy, the LDOS at C is analyzed (Figure 4.9). A comparison of LDOS at C atom of methyl molecule adsorbed linearly on Ni(111) and Pt-Ni surface alloy shows that the energy of 2a₁-derived and 1e-derived states of C on Pt-Ni alloy is 0.04 eV and 0.16 eV lower in energy, respectively, compared to those observed for Ni(111). However, the difference in bonding strength between these two surfaces, which is 0.24 eV in magnitude, stems mainly from the difference between the energy of 3a₁-derived states; for CH₃ adsorbed on Ni(111), the 3a₁-derived states is concentrated at a higher energy than the same orbitals observed for Pt-Ni surface. The reason may be that Ni valance orbitals are concentrated at higher energy values than Pt orbitals (Figure 4.8). Actually, when relativistic effects are excluded from the calculations on Pt-Ni alloy, a resulting upshift in energy of valance orbitals is accompanied with an upshift of 3a₁-derived states formed during binding of CH₃ on Pt and an increase in adsorption energy by a magnitude of 0.43 eV.

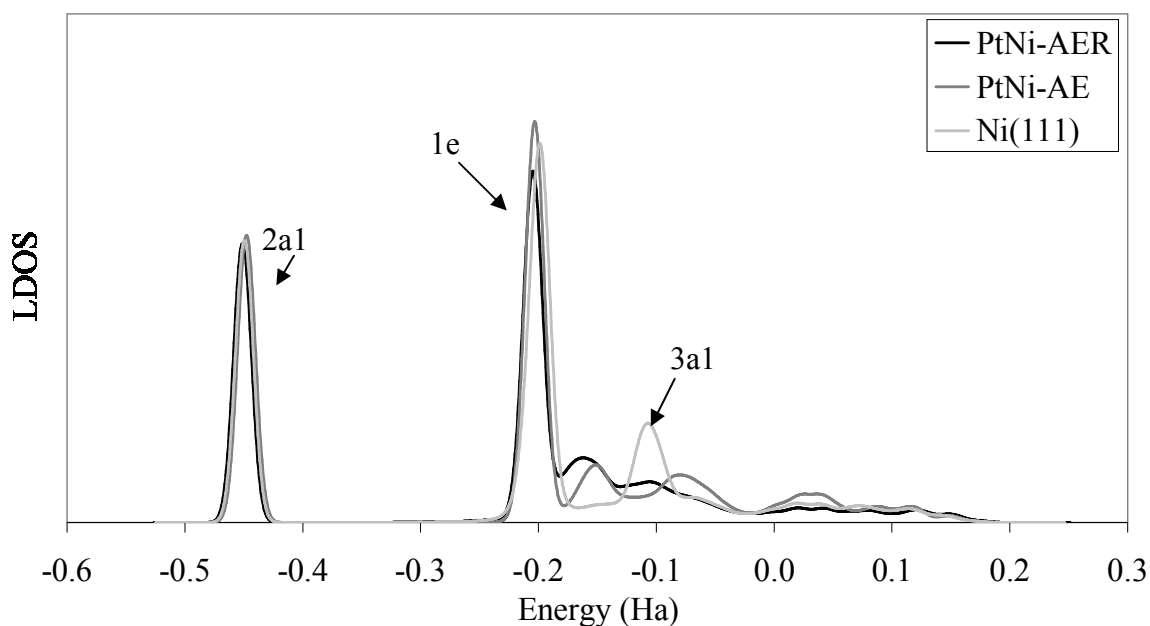


Figure 4.9. LDOS at C of CH_3 molecule adsorbed on Pt-Ni surface alloy and Ni(111). Calculations are performed with two different basis sets: (i) including relativistic effects (AER) and excluding relativistic effects (AE). Calculations for Ni(111) are performed only with AER.

Similar to CH_3 adsorption, the most stable adsorption site for atomic hydrogen is the three-fold hollow site on Ni(111). The adsorption energy of fcc and hcp sites are -2.76 eV and -2.70 eV, respectively. Experimental studies had shown that on Ni(111) hydrogen adsorbs on three-fold site, with an adsorption energy of 49 kJ/mol with respect to molecular hydrogen [116], which is only 4.6 per cent larger than that is reported here. Results obtained for hydrogen along with those obtained for CH_3 adsorption are also close to the computational results of Wang et al. Wang et al. had found that the most stable adsorption sites for H are fcc and hcp sites with an adsorption energy of -2.77 and -2.76 eV, respectively and, for CH_3 , -1.81 and -1.78 eV for fcc and hcp sites, respectively. On Pt-Ni surface alloy, linear adsorption of atomic H is more stable on the Pt site, and its adsorption energy is -2.82 eV, which is lower than the one obtained for Ni(111). Based on HREELS analysis, it was concluded previously that on Pt(111) surface, hydrogen adsorption occurs on fcc sites [117]. Computational studies generally found that atop site is preferable to three-fold hollow site, however the potential energy surface is so flat that differences in zero point energy [118,119] or change in the computational parameters, such as number of metal atom layers [120] may easily change this site preference sequence

during the calculations. Here, it is also seen that the potential energy surface on Pt-Ni surface alloy for hydrogen adsorption is flat and the difference between the adsorption energy of linear and multifold adsorption is very small. It should be also reported that the current results are in contradiction with some previous calculations, which state that atomic hydrogen adsorption is stronger on Ni(111) surface than on Pt(111) [121,122].

The coadsorption of CH_3 and H (CH_3+H) is studied in a $p(3\times 3)$ cell to avoid interactions between periodic cells. For CH_3+H , it is seen that the most stable coadsorption structure is hcp+fcc structure on Ni(111). This is followed closely by the fcc+hcp structure. On Pt-Ni surface alloy, the coadsorption structure is more stable compared to that on Ni(111) at the same surface coverage and the coadsorption structure involves CH_3 adsorbed atop Pt and H on three-fold hollow site (atop_{Pt}+fcc).

4.2.4. Dehydrogenation of Methane

Experimental kinetic studies showed that the activation energy of methane dissociation on Ni catalyst ranges from 0.77 ± 0.10 eV [12] and 0.94 eV [13] to values as high as 1.05 ± 0.04 eV [11]. One of the reasons for these variations in activation energy obtained from experiments may be the relation between the size of Ni particles and the activation energy which was found by experimental studies [123] and was later confirmed computationally [14].

Of the reaction mechanism, DFT calculations are proved to be very useful to shed a light on the details. The generally accepted reaction pathway of CH_4 dehydrogenation on Ni(111) involves CH_4 dissociation on-top of a single Ni atom at the initial stage. Upon dissociation, CH_3 and H species diffuse to opposite hollow sites. The reported activation energy values reported in these computational studies also show variations: The calculated activation energy values on Ni(111) range between 0.71 eV - 1.32 eV [108,110,124] and depends on parameters such as the convergence criteria, the number of layers used to model the system, whether spin-polarization was included or not, the functionals used and additionally, the size of the model. In a recent study, activation energy was calculated to be 1.17 eV in a (2×2) cell [125] and 1.24 eV in a (3×3) Ni(111) cell [104]. In the same

calculations, the heat of reaction was shown to decrease from 0.36 eV to 0.26 eV as the size of the cell is increased.

As the reported values show differences among themselves, it was necessary to obtain the transition state for CH₄ dehydrogenation on Ni(111) surface in order to have a comparison basis for analyzing the reaction on Pt-Ni surface alloy. Ni(111) surface is modelled with a p(3x3) cell that is large enough to eliminate the lateral interactions between the adjacent cells. The Pt-Ni surface alloy is obtained by substituting one of the Ni atoms on the Ni(111) surface with a Pt atom which gives a nearly 11 per cent Pt concentration on the surface.

According to DFT calculations, the reaction involves CH₄ adsorption on top of a Ni atom at the initial stage on Ni(111). The reaction proceeds with breaking of one of the C-H bonds on top of this Ni surface atom and proceeds with the diffusion of the H atom to the neighboring fcc site, while CH₃ diffuses to the opposite and adsorbs on hcp site at the final stage, as seen in Figure 4.10. On Pt-Ni surface alloy, on the other hand, the calculations showed that the reaction pathway with the minimum activation energy starts with CH₄ adsorption on top of a Pt atom. The details of the transition state search is given in Appendix A. During the reaction, one of the H atoms pointing towards the surface is stretched and breaks its bond with C. Then, this H atom diffuses to the hcp site, while leaving the CH₃ molecule on top of the Pt atom nearly unchanged from its initial position.

The structural transition state parameters and energy values obtained for these two surfaces are given in Table 4.8. Comparing the structural parameters at the transition state on both of these surfaces, it is seen that the C-H bond is stretched from 1.10 Å to 1.72 Å for Ni(111) and to 1.43 Å for Pt-Ni surface alloy. In this respect, it is easier for the reaction to proceed to the transition state on the surface alloy. The activation energy required to reach the transition state on the alloy surface is indeed smaller than the activation energy required on the monometallic Ni surface; 1.03 eV vs. 1.48 eV. The reactions are endothermic on both surfaces, whereas the degree of endothermicity is smaller on Pt-Ni surface alloy compared to Ni(111) by 0.04 eV. This is reasonable considering that the coadsorption of CH₃ and H are more stable on Pt-Ni surface alloy, as mentioned previously.

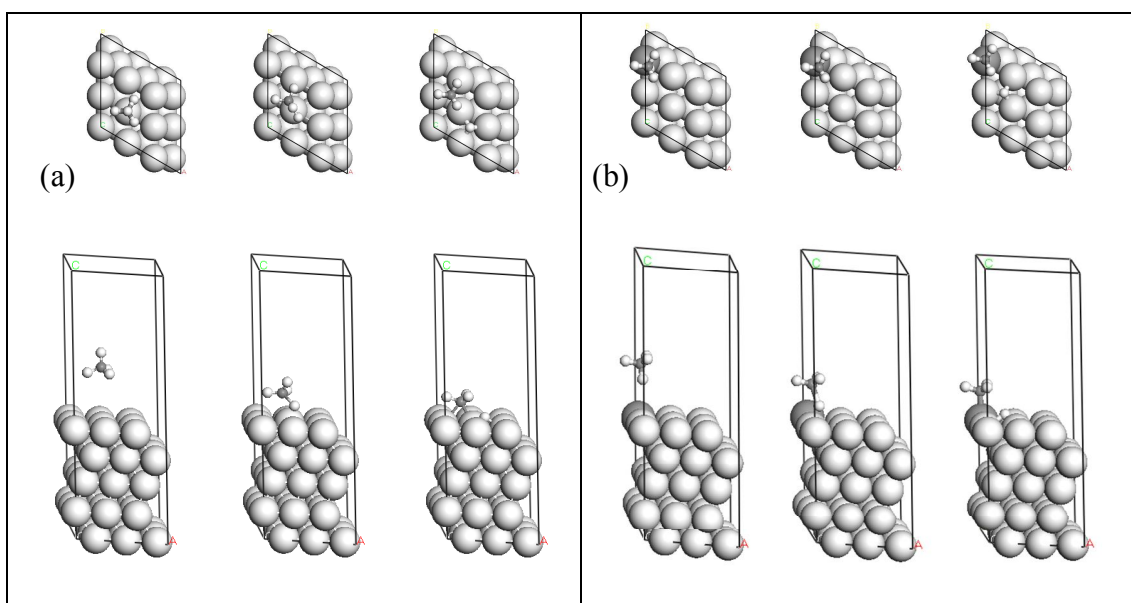


Figure 4.10. Reaction pathway for CH₄ dehydrogenation, initial adsorption state, transition state and the product in series from left to right, on (a) Ni(111) (b) 11%Pt-Ni(111)

Although there is no data in the literature on the activation energy of the methane dehydrogenation reaction on Pt-Ni surface alloys, the reaction on Ni(111) surface has been thoroughly analyzed in both experimental and computational studies. Compared with the results of the previous computational studies, it is seen that the activation energy obtained on Ni(111) is higher than the reported values. One of the reasons is that the size of the unit cell used to model the system is larger than many of the models previously used and this has a direct impact on the activation energy of the reaction. For analyzing the effect of the cell size, the same reaction path on Ni(111) surface is also modelled with a p(2x2) cell. It is seen that the C-H bond stretches to 1.60 Å at the transition state on this surface and the activation energy reduces to 1.37 eV. Other than that, the calculational parameters such as the basis set should be effective on the results, which may cause the differences between the obtained data in different studies.

Table 4.8. The activation energy (E_{ads}), heat of reaction (ΔE_{rxn}) and bond lengths (r) at the transition state

	E_{act} (eV)	ΔE_{rxn} (eV)	$r_{\text{C-H}}$ (Å)	$r_{\text{C-Ni / Pt}}$ (Å)	$r_{\text{H-Ni/Pt}}$ (Å)
Ni(111)	1.48	0.17	1.72	2.29	1.52; 2.55; 2.57
11%Pt - Ni(111)	1.03	0.13	1.43	2.34	2.42; 2.40; 1.64

4.2.5. Summary

The reaction paths for CH₄ dehydrogenation were investigated on Ni(111) and Pt-Ni surface alloy formed by incorporation of trace amounts of Pt into the Ni(111) surface. It was shown that CH₄ dehydrogenation is easier on the Pt-Ni surface alloy, based on the fact that the activation energy of the reaction on that surface is lower than that on the monometallic Ni(111) surface. The lower activation energy is related to the higher stability of linearly adsorbed CH₃ molecules on Pt atoms. The overall results confirm that Pt-Ni surface alloys can be reduced to metallic states at lower temperatures, compared to the Ni(111) surface, and this is one of the reasons of increased catalytic activity and enhanced stability of Pt-Ni bimetallic catalyst in OSR, especially at lower reduction temperatures.

4.3. Adsorption Induced Surface Electronic Reconstruction of Pt and Pt-Sn Alloys During CO Adsorption

CO oxidation reaction on monometallic Pt and Pt-based bimetallic alloys follows a Langmuir-Hinshelwood mechanism for which the initial step is the adsorption of reactants, CO and O₂, on the surface. For this reason, analyzing the differences between the adsorptive properties of Pt and Pt-based alloys by means of the favorable adsorption sites, the adsorption energies and coverage-dependent changes in adsorption, are essential to understand the changes in the activity of Pt-based catalysts, having Pt either in monometallic or alloy forms, in the CO oxidation reaction. Owing to that, CO adsorption on Pt and Pt-based bimetallic or alloy type active sites of the catalysts used in the above mentioned processes, are widely investigated both experimentally [35,126] and theoretically [27,127,128], and an extensive amount of data have been accumulated.

Surface analysis with LEED and EELS showed that CO adsorption occurs only on atop sites on Pt(111) at low surface coverages. These atop-adsorbed CO form a structure with a $(\sqrt{3}\times\sqrt{3})R30^\circ$ pattern starting from coverages as low as 0.17 ML till 0.33 ML [23,24]. The maximum coverage obtainable with only linearly-adsorbed CO on the surface is 0.33 ML; bridge-type occupation has been reported to be observed above 0.25 ML coverage [25]. A $c(4\times 2)$ structure starts to form at 0.35 ML and becomes uniform at 0.5 ML, for which half of the CO are adsorbed atop while the rest are adsorbed on bridge sites

[24,25]. STM also confirms this structure [26]. No three-fold adsorption has been observed at any coverages. In the case of Pt₃Sn(111), however, HREELS analysis of Sn/Pt(111) surface alloy and bulk Pt₃Sn(111) has revealed that multicoordinated CO adsorption sites exist on the alloy surface starting from very low CO coverages. Atop adsorption is still the most favorable structure, but apart from bridge sites, adsorption on threefold hollow sites is also possible on the alloy surface [44].

Theoretical DFT studies, with this respect, are very useful to provide detailed information of the surface and the adsorption process that can not be gained with experimental tools. In parallel to the recent developments in the computer technology, a vast number of scientific papers have been published for the last decade related to the DFT calculations of CO adsorption on transition metals [27-31,127,128]. However, there are still problems related to DFT to be overcome for the CO/Pt system, especially related to the sequence of site preference.

In a bulk number of studies performed with DFT-LDA or GGA functionals, the site preference of CO on Pt(111) (and additionally on Pt-Sn alloy) was falsely predicted and the hollow sites were given to be the most favorable sites for adsorption. It was proven that the reason for this error was not related to the convergence of calculations [28]. Later, Orita et al. found that using numerical basis sets and all electron calculations with scalar relativistic corrections (AER), the correct site preference, i.e. atop sites followed by bridge sites and then the hollow sites, can be obtained and the results are not affected by the choice of exchange-correlation functional [29]. Doll had used a Gaussian type basis set and showed that hybrid B3LYP functional correctly predicts the preference of atop sites, whereas PW91 favors the hollow site [30].

Research on the reasons of these discrepancies at the electronic level revealed that DFT calculations underestimate HOMO-LUMO gap of CO molecule [31]. According to the Blyholder model [129], CO adsorption occurs via donation from the occupied CO-5σ states into empty surface orbitals and the back-donation from occupied surface orbitals to the CO-2π* orbitals. During adsorption, the backdonation of electron density from the substrate to the LUMO of CO molecule increases with the coordination number of the adsorption site and when the position of the LUMO orbital is estimated lower than it

should have been during the calculations, the interaction with the metal electrons are falsely predicted higher on, especially, hollow sites. It was reported that AER calculations solved the problem by shifting the metal d-band and the Fermi level to lower values and, thus, decreasing the interaction of metal d band with LUMO of the adsorbate at an appropriate ratio [29,32]. The effect of relativistic effects on the electronic and chemical properties of Pt(111) surface is shown in Appendix B.

In this study, CO adsorption on Pt(111) and on Pt₃Sn(111) was analyzed for CO surface coverages ranging between 0-0.5 ML. Considering that a correct description of site preference of metal surface is crucial and that DFT-AER calculations have been proven to give the correct site preference for CO adsorption on Pt(111), DFT-AER was also used in this study to analyze CO adsorption on both pure Pt and Pt-Sn alloy. The effect of CO surface coverage on (i) electronic reconstruction of free sites; (ii) extent of adsorbate-adsorbate and adsorbate-surface interactions (iii) adsorption type of CO are parametrically studied. LDOS profiles were used as the tool in analyzing the changes in the electronic structures of the free and occupied states of surface metal atoms, as well as that of adsorbed CO. The adsorbate-adsorbate interaction was studied by analyzing both equilibrium geometric structures and LDOS profiles in combined fashion. Based on LDOS, the parameters that may cause changes in the occupation of sites with varying coverages and the differences between pure Pt and Pt-Sn alloy surface, in this respect, were tried to be explained.

4.3.1. Calculational Parameters

All the DFT calculations were performed with the program package DMol3 (version 4.0). The surface was modeled as four-layer slabs, with the uppermost layer relaxed together with the adsorbate, while the remaining three substrate layers were being fixed in their bulk positions. The accuracy of this structure is tested using a five-layer slab with its uppermost two layers relaxed and shown that the change in the CO adsorption energy is negligible on both atop and bridge sites of Pt(111) and Pt₃Sn(111) and there is no change in the adsorption energy difference between these two sites. The vacuum thickness between slabs is taken as 12 Å. A real-space cutoff of 4 Å was used and the accuracy was

checked with a higher cutoff value, 4.3 Å. No spin-polarization effects were included in the exchange-correlation functional.

The lattice constants of 3.92 Å and 4.02 Å were used for the Pt and Pt₃Sn unit cells, respectively. There is no inward or outward relaxation of topmost Pt atoms at Pt(111), i.e. the interlayer spacing between the first and second layer does not change during surface relaxation. On Pt₃Sn(111), on the other hand, the Pt atoms at the topmost layer relax inward by 0.05 Å, i.e. 1.9 per cent, based on bulk metal interlayer spacing. Sn atom protrudes from the surface by 0.29 Å, which is parallel to LEED results stating that on bare surfaces, there is an outward relaxation of Sn by 0.24 Å [130].

The binding energy of CO individually is calculated from

$$E_{\text{ads}}(\text{CO}) = E^{\text{slab+CO}} - E^{\text{slab}} - E_{\text{CO}}^{\text{free}} \quad (4.9)$$

Here, $E^{\text{slab+CO}}$ and E^{slab} represent the total energy of the surface with adsorbed CO and the energy of the clean surface, respectively. $E_{\text{CO}}^{\text{free}}$ is the energy of the free gas-phase CO molecule. The C–O bond length for free CO molecule is calculated as 1.14 Å.

4.3.2. CO Adsorption on Pt(111)

As an initial step, the strength of four possible CO adsorption sites (Figure 4.11) at a constant surface coverage of 0.25 ML were analyzed. To simulate this surface coverage, one CO molecule was placed in (2x2) unit cell (Figure 4.12). The adsorption energy on these four sites, i.e. top (T), bridge (B_{Pt}), hollow hcp (H_{hcp}) and hollow fcc (H_{fcc}), are reported in Table 4.9. Among the possible adsorption sites, site T is the most favorable site, in parallel with the experimental surface science studies; the atop adsorption energy at 0.25 ML at a p(2x2) pattern is -1.97 eV. This is smaller than microcalorimetry results reported at this coverage [131]. The use of RPBE functional instead of PBE results in an increase in adsorption energy, to a value closer to the experimental data. However, the sequence of site preference and the difference in the adsorption energies of these sites are

proven to be the same with both PBE and RPBE on Pt(111). Thus, PBE calculations are also adequate whenever a comparison is made between different sites.

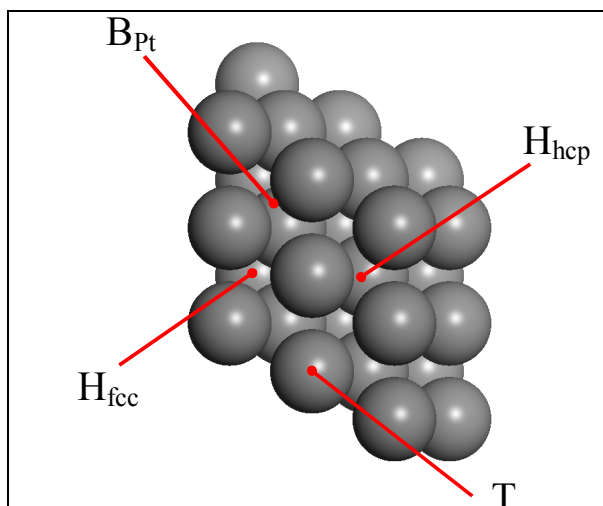


Figure 4.11. Ball model of Pt(111) and various CO adsorption sites available on the surface. Gray balls represent Pt. Sites are labelled as T(atop), B_{Pt} (bridge), H_{hcp} (hollow hcp) and H_{fcc} (hollow fcc).

Table 4.9. Energy of CO adsorption on Pt(111). The values correspond to total adsorption energy per unit cell. Adsorption energy of single CO molecule, in case there is more than one per each cell, is given in brackets where appropriate. Sites are labeled as T(atop), B_{Pt} (bridge), H_{hcp} (hollow hcp) and H_{fcc} (hollow fcc). T- B_{Pt} is for half-atop and half-bridge, and T- H_{fcc} is for half-atop and half-hollow fcc type adsorption.

Site	Cell size	θ (ML)	min(d_{CO-CO})	$E_{ads}(CO)$ (eV)	$d_{C-O}(\text{\AA})$	$d_{C-M}(\text{\AA})$
T	(3x3)-CO	0.11	8.32	-2.01	1.15	1.84
T	(2x2)-CO	0.25	5.55	-1.97	1.16	1.83
B_{Pt}	(2x2)-CO	0.25	5.55	-1.89	1.18	2.02
H_{fcc}	(2x2)-CO	0.25	5.55	-1.87	1.19	2.11
H_{hcp}	(2x2)-CO	0.25	5.55	-1.85	1.19	2.08
T	(3x3)-3CO	0.33	4.81	-5.88 (-1.96)	1.16	1.84
T	(2x2)-2CO	0.5	2.85	-3.48 (-1.74)	1.16	1.83
T- B_{Pt}	(2x2)-2CO	0.5	3.02	-3.65	1.15-1.19	1.85-2.02
T- B_{Pt}	c(4x2)-2CO	0.5	3.66	-3.76	1.15-1.19	1.84-2.02
T- H_{fcc}	c(4x2)-2CO	0.5	3.35	-3.72	1.15-1.20	1.84-2.10

The linear adsorption of CO is followed by bridge adsorption in strength and the difference between the energy of the two adsorption structure is 0.08 eV. The bridge site is followed by fcc and hcp three-fold sites in adsorption strength. It should be noted that the strength of adsorption on these three sites are very close. There are some discrepancies in the adsorption energy difference between atop and bridge sites in the literature. The difference was previously reported as 0.04 eV, as calculated with RPBE functional at 0.25 ML [132], 0.69 eV at very low coverage with B3LYP functional [133] and 0.07 eV at 0.33 ML with B3LYP functional [30]. Mieher et. al. found with EELS that the enthalpy difference between two sites decreases from 0.03 eV at 0.09 ML to -0.01 eV at 0.44 ML and then returns to zero at 0.5 ML [25]. Thus, the difference calculated in this study is in general close to the previously reported ones.

It is known from experimental adsorption studies that Pt(111) dominantly has linearly adsorbed CO from very low coverages to 0.33 ML. As the coverage is increased further, bridge sites are started to be filled. The changes in the electronic structure of the system for both bare and CO-coordinated surface atoms, as well as that of the adsorbate, at coverages 0.11 ML, 0.25 ML and 0.33 ML were examined by means of LDOS analysis; the electronic change was taken as one of the parameters affecting CO adsorption type change with surface concentration variations. The low coverage structure is simulated by placing one CO molecule in a (3x3) cell, which corresponds to 0.11 ML coverage. The adsorption energy of CO at this coverage was calculated as -2.01 eV, which is slightly lower than -1.97 eV for the adsorption energy of CO at 0.25 ML. 0.33 ML coverage was simulated by placing three molecules in (3x3) cell. The adsorption energy of linearly adsorbed CO at a surface pattern of $(\sqrt{3}\times\sqrt{3})R30^\circ$ is -1.96 eV, nearly the same as it was for 0.25 ML.

Accompanying the relatively small change in the adsorption energy with increasing CO coverage, LDOS at CO-coordinated Pt atom and C atom of the adsorbate do not show any differences as surface coverage was increased from 0.11 and 0.33 ML, as shown in Figure 4.13. However, LDOS at neighboring bare surface Pt atoms show deviations from each other depending on CO coverage and from the Pt atoms of the clean surface. LDOS at Fermi energy decreases as the concentration increases along with the intensity of the peaks below Fermi level.

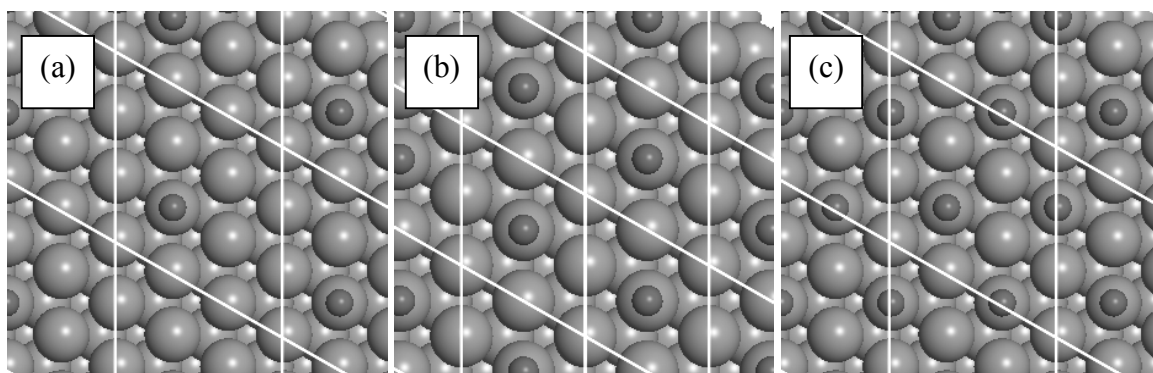


Figure 4.12. CO at (a) 0.11 ML, (b) 0.25 ML - $p(2 \times 2)$ and (c) 0.33 ML - $(\sqrt{3} \times \sqrt{3})R30^\circ$ LEED pattern

It is known that adsorbate-adsorbate lateral interactions, which are effective in the formation of homogeneous adsorption pattern, can be categorized into two groups [134]: (i) The direct adsorbate-adsorbate interactions (“through-space” interactions) and (ii) The substrate-mediated indirect interaction (“through-bond” type). The former is essentially ineffective for CO-CO distance larger than 3.3 Å [135], i.e. for all the structures with a coverage below 0.33 ML in this study (Table 4.9). Thus, above 0.33 ML surface coverage, i.e. the distance between the adsorbates reduce below 3.3 Å, the strength of the surface structures start to be affected both by direct, which is composed of mainly dipolar interactions and indirect interactions [136]. LDOS analysis at three surface coverages here shows that direct interactions are ineffective at these coverages as LDOS at C atom of the adsorbate does not change, however there are the indirect interactions between CO molecules which cause a change in the electronic structure of surface Pt atoms neighboring the adsorption site.

Surface science experiments have shown that on Pt(111) surface linearly adsorbed CO molecules form a $(\sqrt{3} \times \sqrt{3})R30^\circ$ pattern starting from coverages as low as 0.17 ML. Based on this fact, CO-CO pair interaction was claimed to be attractive at the distance of 4.8 Å [137]. Thus, in order to analyze whether the above mentioned electronic changes in the electronic structure of neighbor Pt atoms have any contributonal effect on pattern formation, LDOS at the second-nearest bare neighbor of the adsorption site at 0.11 ML was investigated.

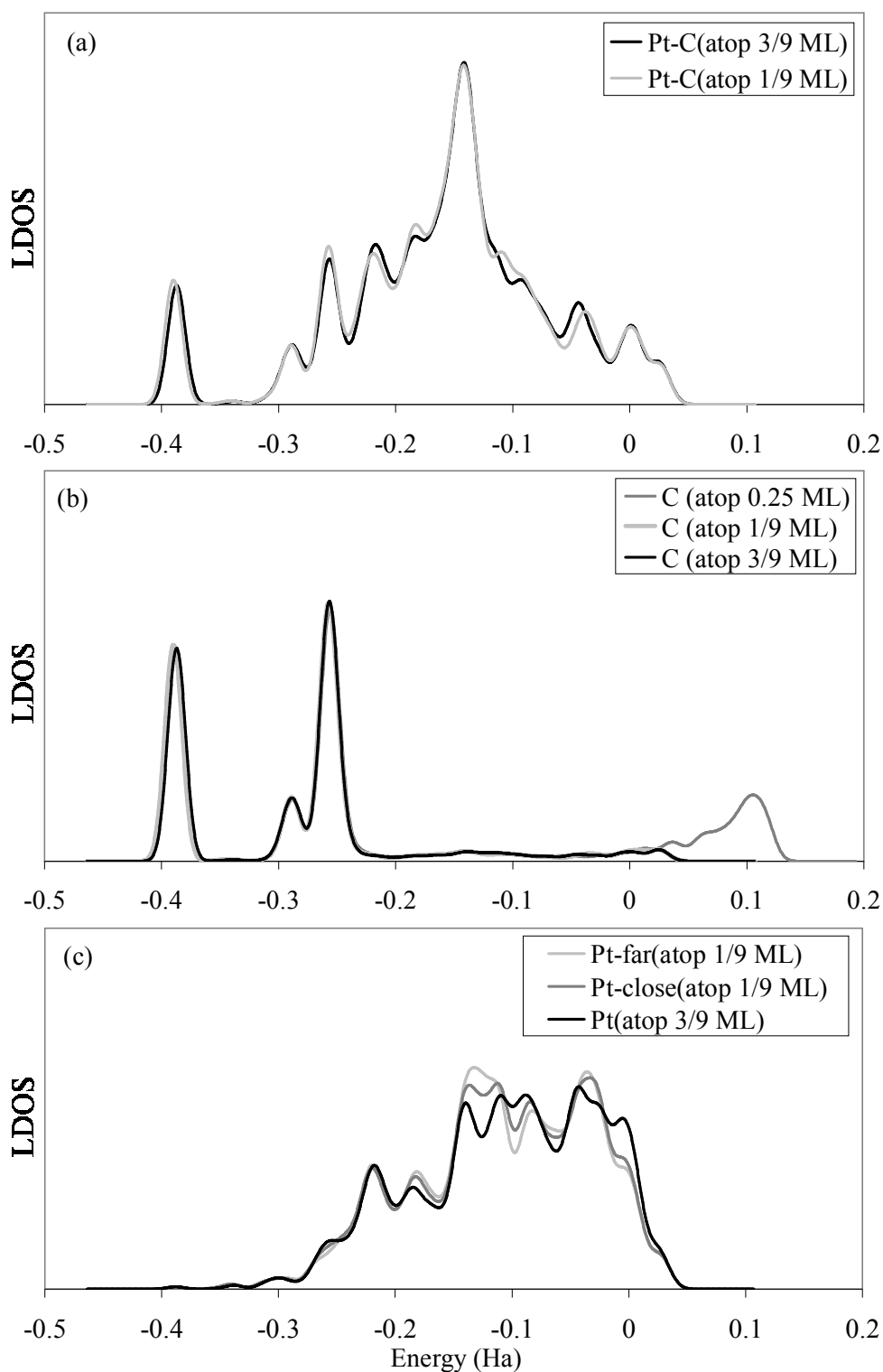


Figure 4.13. Changes in LDOS with coverage increasing from 0.11 to 0.33 ML at (a) CO-coordinated Pt atom (b) C of adsorbed CO molecule (c) bare Pt atoms at the topmost surface layer which are neighbors of adsorption site. Pt-close and Pt-far denote the first and second nearest neighbors, respectively, at 0.11 ML

The results showed that when CO is adsorbed atop Pt, this causes a change in the electronic structure of second-nearest neighbor atoms (Figure 4.14). Compared with the clean surface Pt atoms it is seen that there is a slight shift of d-band towards lower values and a decrease at the intensity at Fermi energy, and additionally there is a decrease in the intensity of peaks below Fermi level. This slight shift in the d-band closes the distance between the HOMO of the adsorbate and thus makes electron donation easier. Similarly, as the distance between the substrate band and LUMO of the adsorbate increases, electron back-donation becomes more difficult. These two combined effects favor the adsorption of CO on atop site other than multifold site, and this may be the reason why only atop sites are occupied on the surface, along with the fact that atop site strength is higher than bridge site by 0.08 eV.

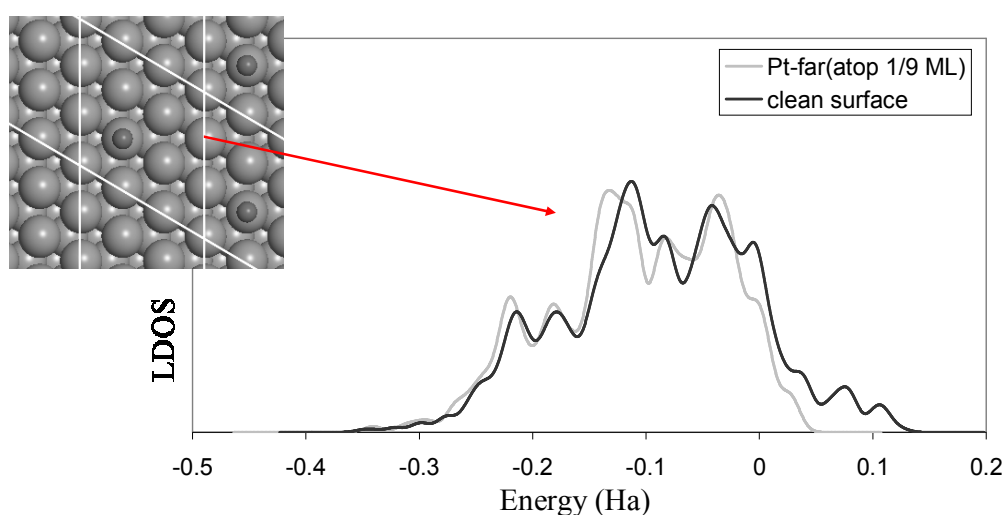


Figure 4.14. Shift of metal LDOS at bare surface Pt atoms to lower values as a result of CO adsorption at 0.11 ML

Above 0.33 ML, addition of any more linearly adsorbed CO would reduce the distance between adsorbates to 2.85 Å (Table 4.9), i.e. the region where strong direct electrostatic repulsive interactions dominate. When the adsorption constitutes only of linearly-adsorbed CO at 0.5 ML (Figure 4.15-d), the total adsorption energy per cell increases to -3.48 eV (-1.74 eV per CO molecule) and there is a tilting of CO molecules by approximately 10 degrees from their perpendicular structure. LDOS analysis of C atom show dominance of direct adsorbate-adsorbate interactions, causing a splitting of molecular orbitals on Figure 4.16. The tilting of CO molecules may also be a sign of the tendency to increase electron back-donation rate.

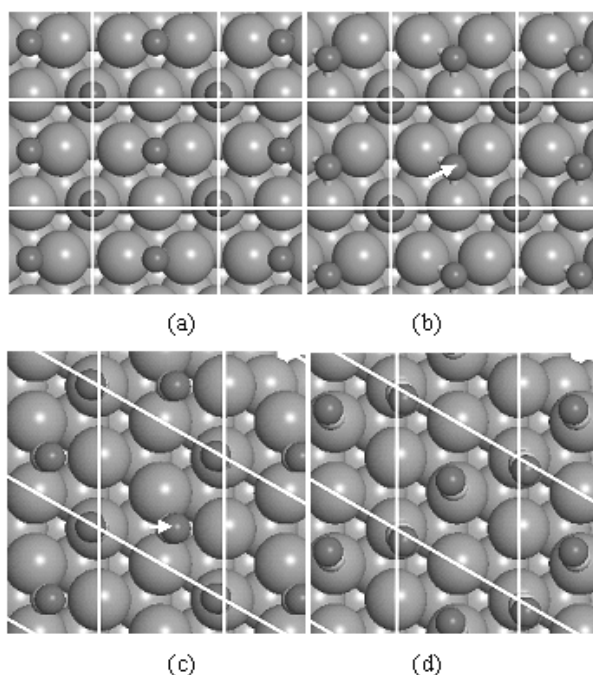


Figure 4.15. CO at 0.5 ML with (a) T-B structure at c(4x2) cell (b) T-H_{fcc} structure at c(4x2) cell (CO diffuses from site B to H_{fcc}) (c) T-B structure at p(2x2) cell (d) T-T structure at p(2x2) cell

The T-B structures, which consist half of the CO adsorbed linearly and half as bridge-type at 0.5 ML are more stable adsorption structures compared to pure atop structure, in parallel with experimental findings. The most stable structure is T-B structure in a c(4x2) cell (Figure 4.15-a). The total adsorption energy of two CO molecules in c(4x2) LEED structure is -3.76 eV, 0.28 eV smaller than that for pure atop structure. LDOS analysis at C atom of the linearly-adsorbed molecule showed that increased coverage decreases the strength of the adsorption structure, which manifests itself in a shift of the molecular orbitals of CO to higher energy values and a decrease in the peak intensities, compared to values at 0.25 ML (Figure 4.16). However, as the CO-CO distances are larger at this structure, LDOS analysis showed that the direct repulsion between the adsorbates is smaller compared to only-atop structure (Figure 4.16). The calculated C-O bond length equals to 1.15 and 1.19 Å for atop and bridge sites, respectively. C-Pt bond length equals to 1.84 and 2.02 Å for atop and bridge sites, respectively, and these values are in agreement with LEED data which give Pt-C bond lengths of 1.85 (± 0.1) Å and 2.08 (± 0.07) Å for atop and bridge sites, respectively and C-O bond lengths 1.15(± 0.05) Å [138].

The other possible T-B structures consists the adsorption of CO on a bridge site close to atop site. However, in both c(4x2) cell and p(2x2) cell, CO adsorbed on bridge site is found to diffuse away from the linearly adsorbed CO. In c(4x2) cell, this resulted in T-H_{hcp} structure, and in p(2x2) cell, the bridge-adsorbed CO is slightly tilted to H_{hcp} site. In both cases, linearly adsorbed CO diffuses slightly from its equilibrium position towards the opposite direction of the other CO molecule. Additionally, it is interesting that the strength of these possible three configurations increase as the distance between the two adsorbates increase.

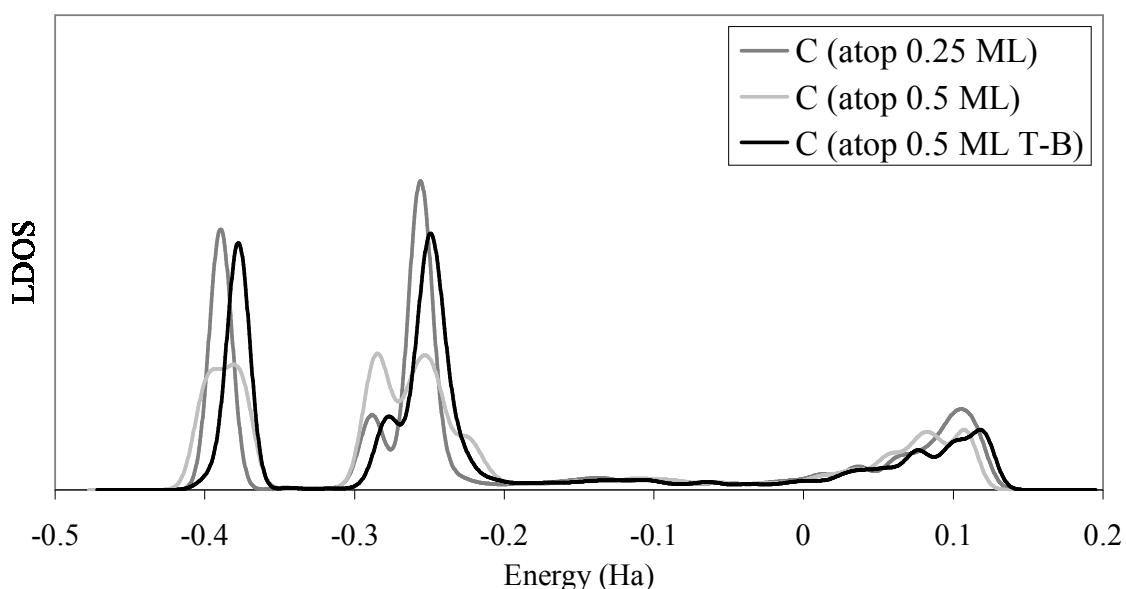


Figure 4.16. LDOS at C atom at 0.25 ML and 0.5 ML with CO adsorbed only linearly and half-linear and half- bridge type (T-B)

4.3.3. CO Adsorption on Pt₃Sn(111)

Similar to the adsorption on Pt(111), the CO adsorption energy on five possible sites at Pt₃Sn(111) surface (Figure 4.17) at 0.25 ML were calculated as an initial step and reported in Table 4.10. A comparison with previously reported values from the literature are also added to the table. It should be noted that CO adsorption is not stable on Sn-including sites [27,46]. The coverage of 0.25 ML is simulated by placing one CO molecule in a p(2x2) cell. The most favorable site, according to AER-DFT calculations, is the atop site (T), with an adsorption energy of -1.72 eV, which is slightly smaller than the results of reported DFT studies (Table 4.10). Adsorption energy of linearly-adsorbed CO on

Pt₃Sn(111) surface was calculated to be 0.25 eV weaker than it is on Pt(111). Previous DFT calculations reported the difference between Pt and Pt-Sn alloy as 0.12 eV [127] and 0.16 eV [139] for atop adsorption. The linear adsorption of CO causes the CO-coordinated Pt atom to buckle by 0.08 Å and the buckling of Sn on the surface reduces to 0.13 Å.

Table 4.10. Energy of CO adsorption on Pt₃Sn(111). Although saturation coverage (θ) is below 0.5 ML on Pt-Sn alloy, the structures at this coverage were tested to analyze deeply the stability-electronic structure interaction. Sites are labeled as T(atop), B_{Pt}(bridge on Pt), B_{Sn}(bridge on Sn), H_{hcp}(hollow hcp) and H_{fcc}(hollow fcc).

Site	θ (ML)	$E_{\text{ads}}(\text{CO})$ (eV)		$r_{\text{C-O}}(\text{\AA})$	$r_{\text{C-M}}(\text{\AA})$
		This work	Literature		
T	0.125	-1.81	-	1.16	1.84
T	0.25	-1.72	(a) -1.40 (b) -1.50 (c) -1.60	1.16	1.85
H _{hcp}	0.25	-1.68	(a) -1.82 (b) -1.63 (c) -1.99	1.20	2.13
B _{Sn}	0.25	-1.66	(a) -1.64 (b) -1.13 (c) -1.89	1.19	2.05
B _{Pt}	0.25	-1.28	(c) -1.35	1.18	2.05-2.09
H _{fcc}	0.25	-1.22	(a) -1.35 (b) -1.14 (c) -1.48	1.19	2.12

a. Ref. 46

b. Ref. 139

c. Ref. 27

The strength of atop adsorption on Pt₃Sn(111) is followed by three-fold hollow (H_{hcp}) and bridge (B_{Sn}) sites. The adsorption energy on these sites are very close, -1.68 eV for H_{hcp} and -1.66 eV for B_{Sn}, to that calculated for atop site T, which means the potential energy surface (PES) is essentially flat on Pt-Sn alloy for CO adsorption. Compared to Pt(111) surface, this flat PES makes multifold adsorption easier on the alloy surface, whereas there is a more pronounced difference between the strength of atop and multifold sites on Pt(111). The increased strength of multifold adsorption relative to linear adsorption on Pt-Sn alloy may be related to the increased π -backdonation rate, which is known to favor multifold adsorption and which directly affects C-O bond length [140]. C-O bond length of the adsorbate on bridge and hcp hollow sites was calculated to be 1.19 Å and 1.20 Å, respectively. These values are larger than the C-O bond lengths on the same

sites at Pt(111) (which are 1.18 Å, for bridge adsorption and 1.19 Å, for hcp hollow adsorption).

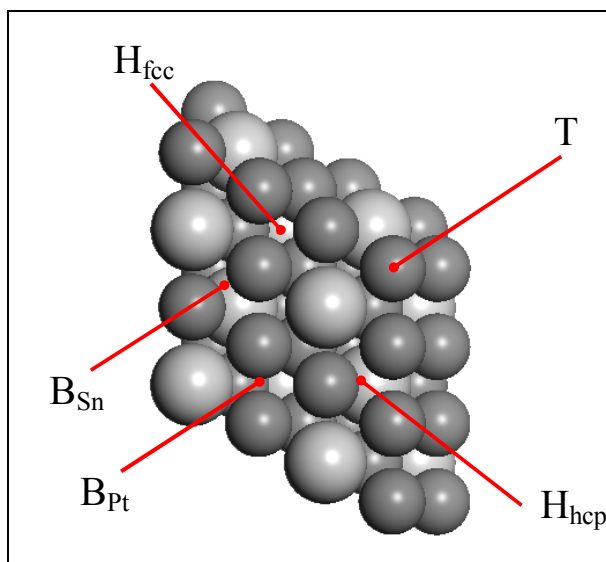


Figure 4.17. Ball model of $\text{Pt}_3\text{Sn}(111)$ and stable CO adsorption sites on the surface. Bigger grey and blue balls represent Sn and Pt, respectively. Sites are labelled as T(atop), B_{Pt} (bridge on Pt), B_{Sn} (bridge on Sn), H_{hcp} (hollow hcp) and H_{fcc} (hollow fcc).

It is difficult to investigate the low coverage region on $\text{Pt}_3\text{Sn}(111)$ in a symmetrical cell due to computational limitations. The low coverage system, in this study, was simulated by placing one CO molecule in a (4x2) cell, which corresponds to 0.125 ML coverage. There is not significant difference in the LDOS at neighboring bare Pt atoms upon CO adsorption compared with LDOS at clean surface Pt atoms (Figure 4.18). As a result, contrary to Pt(111) surface, the change in the electronic structure of surface Pt atoms is less pronounced with increasing coverage. Based on the fact that PES is essentially flat on the alloy surface for 0.25 ML, and considering that there is no external factor that would change the sequence of site preference with varying concentrations, multifold adsorption sites are observed along with atop sites at low surface coverages. EELS showed that the occupation ratio of multifold sites on $\text{Pt}_3\text{Sn}(111)$ decreases as surface CO coverage increases. Lower intensity of the peaks corresponding to multifold sites on HREELS spectra may be discussed in a similar context why CO saturation value is lower on Pt-Sn alloy compared to pure Pt: As CO can not adsorb on Sn, there is geometrically less atoms available on the substrate surface for CO adsorption and as the

CO coverage increases, the competition for surface Pt atoms makes atop adsorption sites more favorable.

It was reported that three-fold sites also exist with bridge and atop sites on $\text{Pt}_3\text{Sn}(111)$, contrary to that on $\text{Pt}(111)$ where only atop and bridge sites are determined [44]. The energy difference between the bridge and three-fold site is very low. Our calculations actually showed that contrary to that on $\text{Pt}(111)$, hollow adsorption is slightly stronger than that on bridge sites. This makes three-fold adsorption possible on the alloy surface. The low intensity of the peaks corresponding to three-fold adsorption on HREELS spectra compared to bridge type adsorption is probably because three-fold sites need more surface Pt atoms.

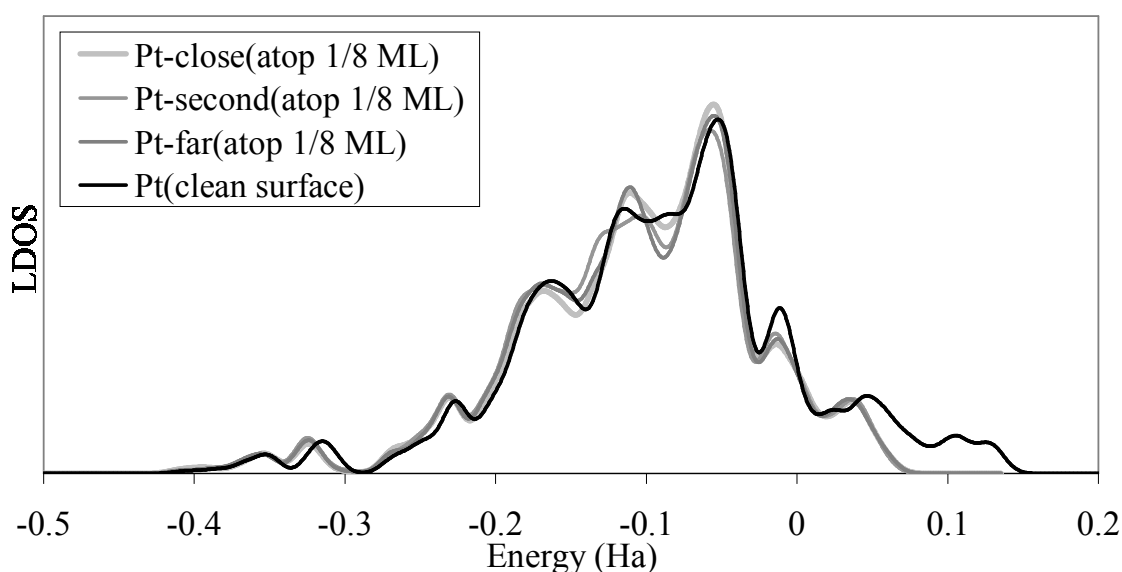


Figure 4.18. Effect of CO adsorption on bare Pt atoms of $\text{Pt}_3\text{Sn}(111)$ surface. Pt-close, Pt-second and Pt-far denote the first, second and farthest neighbors, with respect to the distance to the CO adsorption site at 0.125 ML

4.3.4. Summary

CO adsorption on $\text{Pt}(111)$ and $\text{Pt}_3\text{Sn}(111)$ at coverages ranging from 0.11 ML to 0.5 ML has been studied using theoretical ab-initio methods. DFT-AER has been proved to give the correct site preference of CO adsorption, in parallel to experimental surface science studies, on both pure Pt and Pt-Sn alloy surface. According to the results, the linear

adsorption of CO is the most stable structure on these surfaces. The difference of the adsorption strength between linear adsorption and multifold adsorption is very small on Pt₃Sn(111), which results in the presence of multifold-adsorbed CO along with linearly-adsorbed CO. On Pt(111) surface, the difference in the adsorption strength is larger. CO binding on the surface causes a reconstruction of the electronic structure of the neighboring sites on Pt(111). For CO concentrations up to 0.33 ML, shift of the d-band of neighboring bare Pt atoms to lower values favors linear CO adsorption on these sites. This leads to the formation a $(\sqrt{3} \times \sqrt{3})R30^\circ$ pattern with all the CO linearly adsorbed at low surface coverages. Further increase in CO coverage force bridge type CO adsorption.

4.4. CO and O Coadsorption on Pt₃Sn: Changes in the Adsorptive Properties of the Surface with Alloying and Coverage

Bimetallic alloy sites have higher CO oxidation activities when compared to monometallic sites. Experimental [141-144] and theoretical [145-147] calculations showed that this enhancement in the activity of bimetallic alloys is through a combination of so-called “bifunctional” and “electronic effects”. In the latter, electronic modification of the primary surface metal atoms, like Pt, due to alloying led to a decrease in the adsorption strength of CO and thus the surface becomes more active for the reaction to proceed. In the case of the former, the existence of a second metal, like Ru or Sn, at the bimetallic alloy surface creates highly favorable sites for oxygen adsorption and thus eliminates competition between CO and O during adsorption. Both of these factors are related to the adsorption properties of the metal surface and the increased catalytic activity of the alloy compared to monometallic metal is a result of the differences between the adsorption properties of the surface.

Apart from the adsorption of single species, studies on coadsorption of CO and O simultaneously on the surface has special importance, especially if there is a strong interaction between adsorbed CO and O. A number of experimental and theoretical studies performed on different metal surfaces have shown that coadsorption of the species leads to a change in the adsorption properties of the species such as a decrease in adsorption strength with changes in adsorbate-metal bonds and, in some cases, a change in the adsorption site preference of the species. On Rh(111), LEED analysis of the coadsorbate

surface structure of CO and O showed that CO adsorbs on atop sites and oxygen on threefold fcc sites in both of the (2x2)-(O+CO) and (2x2)-(2O+CO) overlayer structures [148,149]. CO coadsorption on Rh(111) leads to a weakening of bonds between O and surface metal atoms which indicates itself as an increase in the O-Rh bond lengths [148]. In the (O+2CO) structure, some CO molecules are also found to occupy hcp sites after atop sites are 100 per cent full [149] and RAIRS results also show that adsorption of CO on bridge sites also becomes possible [150]. Temperature programmed desorption experiments showed that due to bonding competition between O and CO for the same Rh atoms at high CO coverages, the bond strength of CO decreases, which leads to increased CO₂ formation rate [148,150]. Similarly, on Ru(001) surface, CO prefers to adsorb on top sites and O on hcp sites in the (2x2)-(O+CO) phase. Upon an increase in the surface O coverage, LEED analysis showed that O also start to fill the fcc sites and as the surface restructures itself in such a way that atop adsorption of CO becomes possible [151]. DFT calculations showed that the decrease in the binding strength of CO upon O coadsorption in the (O+CO) phase is as small as 0.07 eV, and what is more, this small decrease is assumed to be a result of electrostatic repulsion between the adsorbed CO and O, i.e. the bonding on Ru(001) is rather localized [152]. DFT results interestingly showed that increasing O coverage further, from O+CO to 2O+CO structure, a small increase in the adsorption energy of CO occurs, which is attributed to the weakening of surface metal Ru bonds due to strong O adsorption. On Pd(111) metal surface, on the other hand, O and CO competes for the same adsorption sites; they both prefer to adsorb on hollow sites. The adsorption of CO on the hollow site is very stable and DFT calculations showed that the energy difference between the adsorption of CO on hollow site and atop site is as large as 0.5 eV, the latter being less stable [153]. LEED analysis of the coadsorbate surface structure showed that CO molecules form a separate phase and not a mixed CO+O adlayer, until finally high exposures of CO is used on Pd(111). There is no such a bonding competition on Pt(111) and DFT calculations proved that CO and O adsorb on top and hollow sites, respectively, and that there is a weak interaction between the CO molecule and chemisorbed O atom; the decrease in the binding strength of CO upon coadsorption was found to be 0.04 eV with using a 3-layer slab in the calculations, all of which were kept frozen in their bulk positions during the adsorption [154]. In a following paper however, it was claimed that surface relaxation has a direct influence on the binding strength of reactants and using a 6-layer slab with the topmost 3 layers relaxed, a decrease

by 0.2 eV in energy was found in the adsorption strength of CO upon O coadsorption on Pt(111) [155]. When Pt is alloyed with Ru, the decrease in the CO binding strength on PtRu(111) due to O coadsorption was found to be approximately 0.12 eV with the same calculational parameters. Another study showed that alloying Pt with Sn led to a decrease in the coadsorption strength by 0.10 eV [156].

In the related research papers, O-Pt₃Sn [147], CO-Pt₃Sn [27], and (O+CO)-Pt₃Sn [156], oxygen adsorption was studied for a fixed surface concentration at a single total coverage. In this study, coadsorption of CO and O on Pt₃Sn(111) was studied aiming to analyze the changes in the binding strength of O and CO on the metal surface led by coadsorption. The study also includes a parametric investigation on the relation between relative surface concentrations of CO and O and their adsorption energies.

4.4.1. Calculational Parameters

Density-functional theory calculations were carried out using the program package CASTEP (version 2.2.1). The electronic wave functions involved were expanded in a basis set of plane waves, up to a kinetic energy cutoff of 340 eV. The calculated lattice constant of Pt₃Sn is 4.01, which is in correspondence with the experimental value of 4.0 Å [130]. No spin-polarization effects were included in the exchange-correlation functional.

The Pt₃Sn surfaces were modelled as four-layer slabs, with the uppermost layer relaxed together with the adsorbate, while the remaining 3 substrate layers were being fixed in their bulk positions. The vacuum thickness between slabs is 12 Å. In order to check whether the thickness of the slab and number of layers relaxed would affect the adsorption energies, we recalculated the adsorption energies using a 6 layer slab with the bottom 3 layers kept frozen in their positions while the rest is relaxed. It was shown that the change in the adsorption energy of CO alone and coadsorbed with O is approximately 0.02 eV and 0.03 eV, respectively, which proves that using a 4 layer slab has been sufficient to obtain the correct CO adsorption energy.

The binding energy of CO on O covered surface is calculated by

$$E_{\text{ads}}^{\text{CO/slab+O}} = E^{\text{slab+O+CO}} - (E^{\text{slab+O}} + E_{\text{CO}}^{\text{free}}) \quad (4.10)$$

or

$$E_{\text{ads}}^{\text{CO+O/slab}} - (E^{\text{slab}} + E_{\text{CO}}^{\text{free}} + E_{\text{O}}^{\text{free}}) \quad (4.11)$$

Here, $E^{\text{CO+slab+O}}$, $E^{\text{slab+O}}$ and $E_{\text{CO}}^{\text{free}}$ represent the total energy of the surface with coadsorbed O and CO, the total energy of the surface with chemisorbed O individually and free energy of CO molecule, respectively. The binding energy of CO individually is calculated by

$$E_{\text{ads}}^{\text{CO/slab}} = E^{\text{slab+CO}} - (E^{\text{slab}} + E_{\text{CO}}^{\text{free}}) \quad (4.12)$$

Here, $E^{\text{slab+CO}}$ and E^{slab} represent the total energy of the surface with chemisorbed CO and the energy of the clean surface, respectively. The binding energy of oxygen, referenced to atomic oxygen in vacuum, is calculated in a similar way. The effect of coadsorption on the binding energy is calculated by

$$\Delta E = E_{\text{ads}}^{\text{CO/slab+O}} - E_{\text{ads}}^{\text{CO/slab}} = E^{\text{slab+CO+O}} - E^{\text{slab+O}} - E^{\text{slab+CO}} + E^{\text{slab}} \quad (4.13)$$

The adsorption of CO and O was studied in a p(2x2) surface unit cell. The surface coverage is 0.25 ML for both CO and O, if not specified otherwise.

4.4.2. Adsorption of CO and O

Firstly, the adsorption properties of CO and O on Pt₃Sn(111) are determined aiming to form a comparison basis for coadsorption studies to follow. Possible stable adsorption sites were previously reported for both CO [27,46,139] and O [147]. CO adsorption sites and the calculated adsorption energies are given in Figure 4.19 and Table 4.11, respectively. The most favorable adsorption site, according to our calculations, is hollow hcp Pt3 site, with an adsorption energy of -1.97 eV, followed by atop and hollow fcc Pt3 sites with adsorption energies of -1.63 eV and -1.40 eV, respectively. The site preference

sequence is the same as the results of DFT studies in the literature and adsorption energies are close to that reported in these studies [27,46,139]. It is known that DFT tends to overestimate the binding strength of CO on high-coordinated 3-fold sites on metal surfaces, which is not related to convergence based problems or on the choice of variables, such as exchange-correlation functional, as explained for Pt(111) surface [28]. So, although experimental findings of Paffett et al. showed that the most favorable site for CO adsorption on Pt₃Sn(111) is atop site [44], the most favorable site, according to the results of our DFT calculations, seems to be three-fold hcp site. However, as we used the results mainly to make a comparison of the adsorption strength of components in their individual states and coadsorption states, the wrong estimation of CO site preference by DFT did not affect our conclusions.

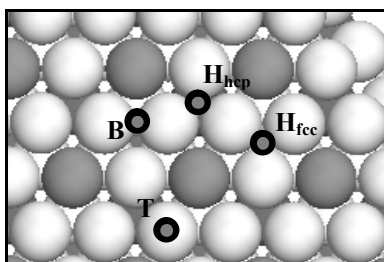


Figure 4.19. Ball model of Pt₃Sn(111) surface from top and CO adsorption sites available on the surface. Small gray-over-black balls represent CO. Bigger dark and light balls at the sublayer represent Sn and Pt, respectively.

Table 4.11. Calculated CO adsorption energies and bond lengths on Pt₃Sn(111)

Site	Description	$E_{\text{ads}}(\text{eV})$	$d_{\text{C-O}}(\text{\AA})$	$d_{\text{C-Pt}}(\text{\AA})$	$d_{\text{C-Pt}}(\text{\AA})$	$d_{\text{C-Pt}}(\text{\AA})$
T	atop Pt	-1.63	1.16	1.88	-	-
H _{hcp}	hollow hcp Pt ₃	-1.97	1.19	2.12	2.12	2.12
B	bridge Pt-Pt	-1.38	1.18	2.03	2.03	-
H _{fcc}	hollow fcc Pt ₃	-1.40	1.19	2.10	2.10	2.10

Experimental and theoretical studies show that oxygen generally prefers to adsorb on 3-fold hollow sites on the close packed (111) surface termination of metal catalysts. The stable adsorption sites and the calculated adsorption energies of chemisorbed oxygen for Pt₃Sn(111) surface, with respect to atomic oxygen in vacuum, are given in Figure 4.20 and Table 4.12, respectively. The most stable site is site A, i.e. fcc Pt₂Sn, with an adsorption

energy of -3.91 eV. This is close to the value previously calculated by Watwe et. al [147]. The adsorption strength of fcc Pt₂Sn is followed by adsorption on site B, i.e. hcp Pt₂Sn. The difference in the adsorption energy values of those two sites is 0.52 eV, slightly higher than what was calculated for Pt(111) (0.47 eV) [157].

To make a comparison, we also calculated the adsorption energies of O and CO on Pt(111) with the same computational parameters used for Pt₃Sn. On Pt(111), the most stable sites for the adsorption of CO and O are atop Pt and fcc Pt₃ sites, respectively. The calculated CO adsorption energies on Pt(111) was -1.75 eV, which is in agreement with the results of microcalorimetry experiments reported in the literature [158]. The calculated O adsorption energy was -3.85 eV. It was determined using temperature programmed desorption, isothermal desorption, AES, LEED and isotopic measurements that oxygen dissociates above 150 K and the estimated heat of adsorption is 48 kcal/mol on Pt [159]. The adsorption structure is a well ordered p(2x2) at temperatures $200 \leq T \leq 350$ K and the adsorption site is fcc three-fold hollow site at a height of 0.85 ± 0.06 Å above the Pt surface layer [160]. Thus, the calculations on oxygen adsorption are in agreement with surface science studies.

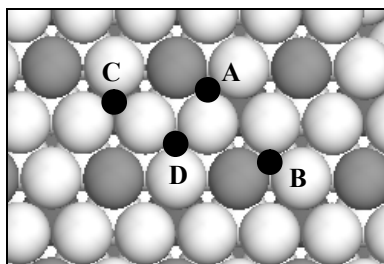


Figure 4.20. Ball model of Pt₃Sn(111) surface from top and O adsorption sites available on the surface. Small black balls represent O. Bigger dark and light balls at the sublayer represent Sn and Pt, respectively.

CO adsorption is stronger on monometallic Pt by 0.12 eV, whereas O adsorption is weaker by 0.06 eV compared to Pt₃Sn alloy. It is interesting to note that O adsorption on fcc Pt₃ site is 1.12 eV weaker on Pt₃Sn(111) than it is on Pt(111). In order to explain the differences in adsorption strength of O on Pt(111) and Pt₃Sn(111), LDOS profiles at O and at Pt of three different adsorption sites, fcc Pt₂Sn and fcc Pt₃ of Pt₃Sn(111) and fcc Pt₃ on Pt(111), which are given in Figure 4.21 and 4.22, are studied. LDOS at O on three site

have similar features. The first peak on Figure 4.21, at between -20 and -17 eV is attributed to O-2s derived orbital which mixes only to a small extent with the metal states as seen in Figure 4.22 and is more stabilized in the case of fcc Pt3 site on Pt(111). The peak at the region between -8 and -4 eV is the result of the mixing of O-2p orbital and metal d-states which is especially effective in O-metal bonding as mentioned elsewhere [157]. As noted previously, O adsorption on fcc Pt3 site is 1.12 eV weaker on Pt₃Sn(111) than it is on Pt(111). The O-2p derived peak between -8 and -4 eV is at a lower energy for fcc Pt3 site on Pt(111) (at approximately -6.4 eV) than it is for fcc Pt3 site on Pt₃Sn(111) (at approximately -5.7 eV) and its intensity is higher. This shift in the LDOS at O on Pt₃Sn(111) towards higher energy levels is a clear indication of the weaker Pt-O bonding strength of fcc sites on the alloy surface. Zhang et al. had found similarly that on Cu₃Pt(111), LDOS at O is shifted upwards compared to monometallic Cu and O adsorption consistently is weaker on Cu₃Pt [146]. Lynch and Hu also had shown that there is, in general, a direct relation between the O adsorption strength and the intensity of 2p(O)-d(Pt) derived peak at O-LDOS curves for different adsorption sites on Pt(111) [157].

Table 4.12. Calculated O adsorption energies and bond lengths on Pt₃Sn(111)

Site	Description	E _{ads} (eV)	d _{O-Pt} (Å)	d _{O-Pt} (Å)	d _{O-Pt/Sn} (Å)
A	fcc Pt2Sn	-3.91	2.14	2.13	2.06
B	hcp Pt2Sn	-3.39	2.18	2.18	2.02
C	hcp Pt3	-3.36	2.15	2.16	2.16
D	fcc Pt3	-2.74	2.10	2.11	2.11

The difference between fcc Pt2Sn and fcc Pt3 sites on Pt₃Sn(111) is that while the former has 2 Pt atoms and 1 Sn atom, the latter only consists of 3 Pt atoms. The O-2p derived peak for fcc Pt2Sn site, which is at approximately -6.4 eV, is at higher energy than the same peak for the other two fcc Pt3 sites on Figure 4.21. This may seem contradictory to the fact that O adsorption is strongest on that site. The greater adsorption energy of fcc Pt2Sn site comes from the strong Sn-O bond and this bond is a result of mixing of O p-states and Sn-p states, as is evident from the reduced electron density at the region below the Fermi level, as indicated in Figure 4.21-b. The strong O adsorption on fcc Pt2Sn reflects itself at LDOS profile of adsorbed O as broadened peak between ca. -8 and -4 eV. The peak broadening at O-LDOS occurs through electron transfer from Sn to at the sites in

the region between ca. -5 to 0 eV. The Sn-O bond length is also shorter than Pt-O bond lengths on Pt₃Sn (Table 4.12). Additionally, there is a peak on the LDOS curve of O for fcc Pt₂Sn site of Pt₃Sn(111), at ca. -8.7 eV, which does not appear on the fcc Pt₃ site, meaning that adsorption on this site involves more than mixing of 2p(O)-d(Pt) states. The peak at approximately -8.7 eV is attributed to the mixing of O-2p orbital and Sn s-states. As there is no Sn atom involved in the adsorption of O on fcc Pt₃ sites, that peak does not appear at the LDOS curves of these sites.

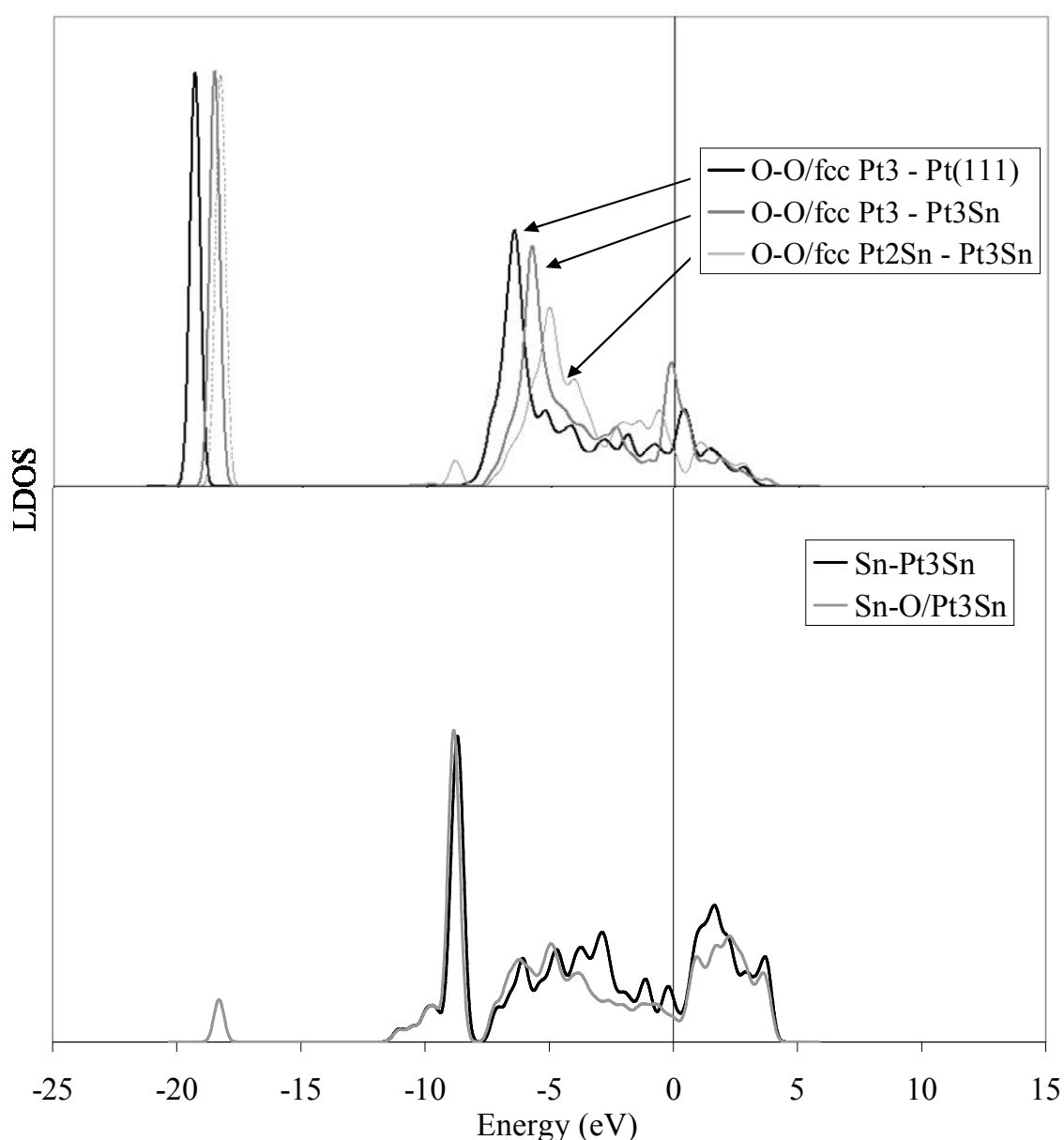


Figure 4.21. LDOS at (a) O adsorbed on three different adsorption sites on Pt₃Sn(111) and Pt(111), and (b) Sn before and after O adsorption on site fcc Pt₂Sn on Pt₃Sn(111).

The weaker Pt-O bond on fcc Pt₂Sn site of Pt₃Sn(111) is also evident from the shift in LDOS at Pt during O adsorption. While there is a shift in energy of the LDOS curve towards lower values at Pt(111), at the region between -8.5 and -3.5 eV, this shift is smaller for LDOS at Pt on Pt₃Sn(111) (Figure 4.22-a and 4.22-b). For fcc Pt₂Sn site, the adsorption strength of O is dominantly determined by the bond between O and Sn atom.

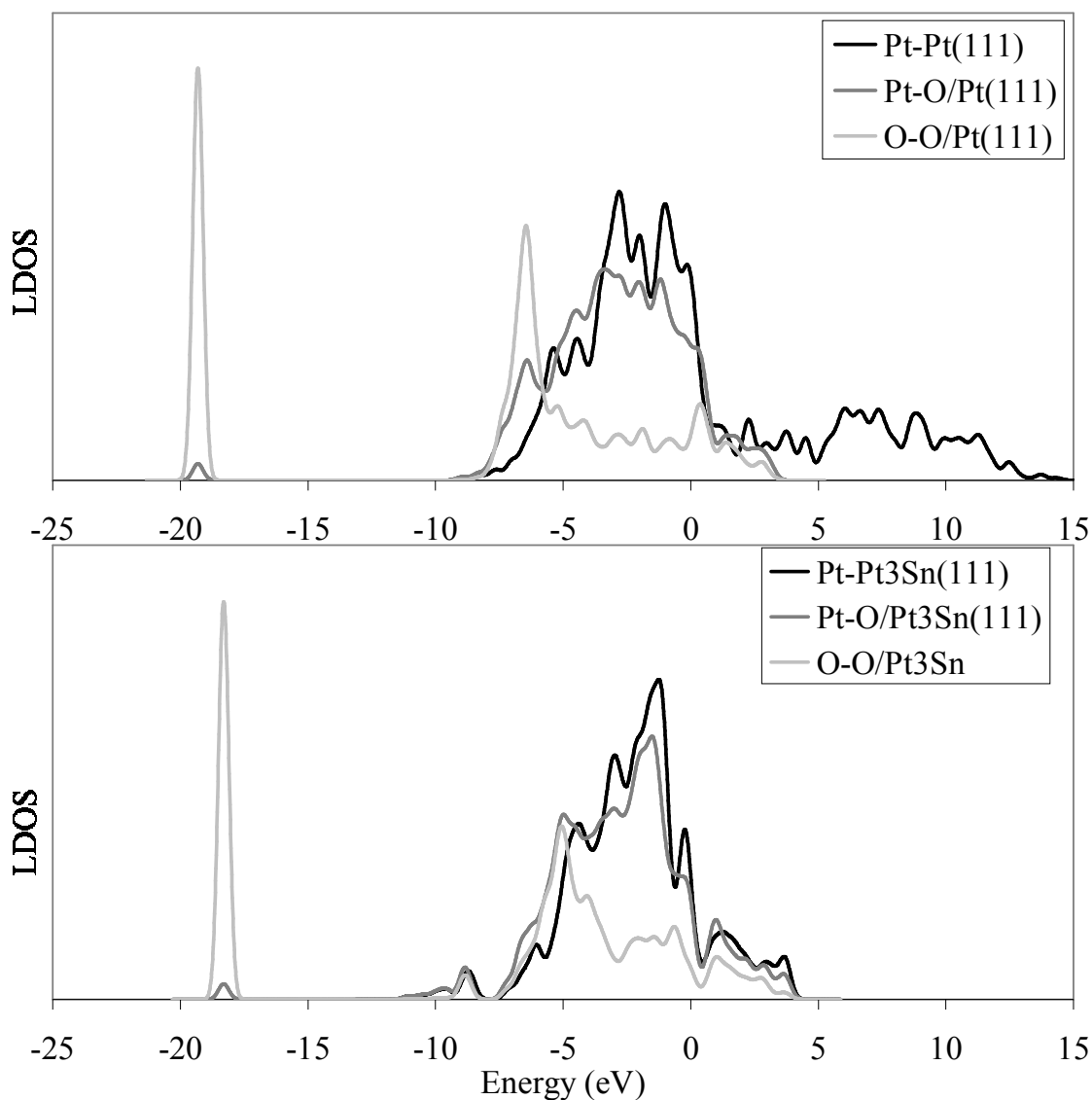


Figure 4.22. Changes in LDOS profiles at Pt atom of (a) fcc Pt₃ site on Pt(111) and (b) fcc Pt₂Sn site on Pt₃Sn(111), after O adsorption on site.

4.4.3. Coadsorption of CO+O

CO and O surface coverages are both taken as 0.25 ML (total coverage 0.5 ML) for the CO+O coadsorption system throughout the paper, if not specified otherwise. When CO

is adsorbed on O-precovered surface, the adsorption energy of CO changes due to interaction between the two adsorbed reactants. The most stable site configuration for coadsorption and the adsorption energies of CO on O-precovered surface are given in Figure 4.23 and Table 4.13, respectively. The most stable coadsorbate structure with the minimum energy on $\text{Pt}_3\text{Sn}(111)$ is CO-atop Pt/O-fcc Pt_2Sn , i.e. CO adsorbed atop Pt and O adsorbed on fcc- Pt_2Sn site (Figure 4.21-a). This is followed by CO-atop Pt/O-hcp Pt_2Sn structure, with respect to the total energy level of the system.

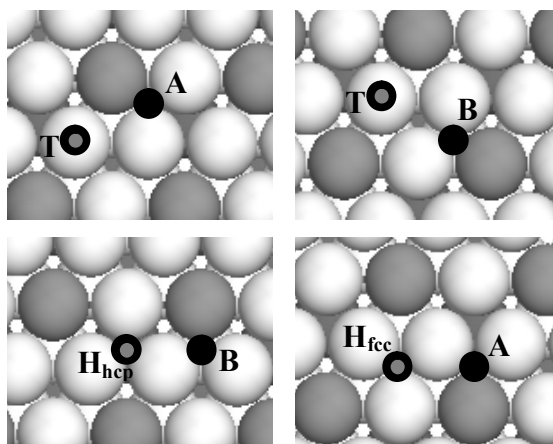


Figure 4.23. Ball model of $\text{Pt}_3\text{Sn}(111)$ surface from top and stable O+CO coadsorption sites. Small black and gray-over-black balls represent O and CO, respectively. Bigger dark and light balls at the sublayer represent Sn and Pt, respectively.

The calculations showed that the adsorption energy of CO is not affected from preadsorbed O to a great extent at the surface coverage of 0.25 ML, except for the cases where there is a bonding competition between the adsorbents. For the CO-atop Pt/O-fcc Pt_2Sn , and CO-atop Pt/O-hcp Pt_2Sn , the decrease in the adsorption strength due to coadsorption is 0.06 and 0.02 eV, respectively (Table 4.13). The only important change in adsorption energies occurs when the reactants share the same surface Pt atom(s) during adsorption. For example, for CO-hcp Pt_3 /O-hcp Pt_2Sn system, the adsorbed reactants share two Pt atoms between their corresponding adsorption sites (Figure 4.23). Consequently, the adsorption energy of coadsorbed species decreases by nearly 0.3 eV, due to bonding competition. We can conclude that, for stable CO coadsorption, O should adsorb either on fcc Pt_2Sn site or hcp Pt_2Sn site. Adsorption of O on fcc or hcp Pt_3 at 0.25 ML coverage means occupation of all surface Pt atoms by O atoms and CO should adsorb on a surface Pt atom which also binds O. The sharing of the same surface Pt atom by CO and O will

decrease the stability of CO as stated previously. Another factor for the stability of the coadsorbate structure is the distance between the two adsorbed species. As an example, when the CO-hcp Pt3/O-fccPt2Sn system is considered, the adsorption of CO becomes unstable, although hcp Pt3 is a stable site for CO adsorption; there, the diffusion from hcp Pt3 site to atop Pt site is observed since the adsorbed species are very close to each other. As the adsorption of O is stronger, at such unstable cases, diffusion of CO always occurs at the end.

Table 4.13. Calculated CO adsorption energies on O precovered surface and changes in the adsorption energy upon O+CO coadsorption on Pt₃Sn(111) (total surface coverage is 0.5 ML)

Site	Description	$E_{\text{ads}}^{\text{CO+O/slab}}$ (eV)*	$E_{\text{ads}}^{\text{CO/slab+O}}$ (eV)	$-\Delta E$ (eV)
T-A	CO-atop Pt/O-fcc Pt2Sn	-5.49	-1.57	0.06
T-B	CO-atop Pt/O-hcp Pt2Sn	-5.01	-1.62	0.02
H _{hcp} -B	CO-hcp Pt3/O-hcp Pt2Sn	-5.07	-1.67	0.30
H _{fcc} -A	CO-fcc Pt3/O-fcc Pt2Sn	-4.83	-0.91	0.49

*: total coadsorption energy calculated by using the alternative equation (4.11)

For the CO-atop Pt/O-fcc Pt2Sn structure, the decrease in the adsorption energy of CO is 0.06 eV at 0.25 ML coverage. This reminds Bleakley et al.'s assumptions that the interaction of CO and O is short range on monometallic Pt surface [154]. They had calculated a change in the adsorption energy by 0.04 eV with similar sites on Pt(111) upon coadsorption at the same surface coverage. However, Han et al. proved that on Pt(111), due to strain effects, there is a more pronounced interaction between CO and O than what was reported by Bleakley et al. [155]. According to Han et al., the Pt atom on which CO adsorbs is pulled out from the surface with respect to the bare Pt atoms during adsorption and this isolation of Pt atom from the surface strengthens the bond between Pt and CO. After O coadsorption, since O also pulls out the Pt atoms, the metal surface becomes flatter and the strength of CO adsorption decreases as a result of coadsorption (by 0.2 eV).

The coadsorption structure on Pt(111) was also analysed to make a comparison of coadsorption properties of Pt₃Sn(111) and Pt(111), by applying the same computational parameters used for Pt₃Sn. On Pt(111), we considered the most stable adsorbate structures,

i.e. the adsorption of CO atop Pt and O on fcc Pt₃ sites. Upon O coadsorption, the CO adsorption energy becomes -1.63 eV on Pt(111); the increase in the CO adsorption energy upon coadsorption is 0.13 eV, i.e. approximately 2 times bigger than it is on the alloy, which means the preadsorbed O has a more pronounced effect on the adsorption strength of CO on Pt(111) compared to that on Pt₃Sn(111).

In order to analyze the differences between Pt and Pt₃Sn alloy in this respect, we examined the surface relaxations during adsorption of CO and O and coadsorption of CO and O on both Pt(111) and Pt₃Sn(111) alloy. During surface relaxation of the clean alloy surface, due to size difference between Sn and Pt, Sn atom on the outermost layer protrudes outward from the surface with respect to the Pt atoms and the surface at the end is not as flat as clean Pt(111). After O adsorption, on Pt(111), O pulls out all 3 Pt atoms of fcc Pt₃ site at the same degree, whereas on Pt₃Sn(111), O only pulls out the Sn atom binded to it (O-Sn bond length is 2.06 Å, i.e. shorter than O-Pt bond length, which is 2.14 Å in average, as seen in Table 4.12), and the position of the Pt atoms at the fcc site essentially remain unchanged with respect to other atoms in the topmost layer. So, when CO is coadsorbed and pulls out the Pt atom under itself above the other surface Pt atoms (by 0.21 Å in the case of Pt₃Sn), the topmost layer is not as flat as it is on Pt(111). At the coadsorbate structure, Sn atom binded to O is also above the surface Pt atoms by 0.06 Å (Figure 4.24). In summary, while CO coadsorption on O-precovered Pt(111) surface causes strain affects due to the flatness of the surface, there is a more pronounced surface corrugation on Pt₃Sn alloy as a result of different Sn-O and Pt-O bond strengths, which reduces the strain caused by coadsorption. O adsorption on Pt₃Sn(111), in this respect, is similar to OH adsorption on Pt(111) reported by Han et al. where OH adsorbs at the top site of Pt and pulls out only one Pt atom. It is reported that, after O coadsorption, the surface corrugation is less than it is after OH coadsorption and, consequently, OH coadsorption on CO precovered surface reduces the adsorption strength of CO less than O coadsorption [155].

4.4.4. Effect of Surface Coverage on Coadsorption

It is interesting to analyze the changes in the adsorption energy of CO with coadsorption as a function of coverage (Table 4.14). At a surface coverage of 0.125 ML,

CO adsorption energy on clean and O precovered surface (surface coverage of O-fcc Pt₂Sn is also 0.13 as in Figure 4.25) is -1.76 eV and -1.56 eV. The decrease in the adsorption strength of CO due to O presence on the surface at this coverage is 0.21 eV, and is much greater (more than 3 times as much) than it is for a surface coverage of 0.25 ML (0.06 eV). When the O coverage is increased to 0.5 ML, CO adsorption strength increases and the adsorption energy becomes -1.66 eV (Figure 4.26). Thus, the second adsorbed O on the supercell has a positive effect on the adsorption strength of CO. A similar situation was reported by Stampfl and Scheffler [152] in a recent paper where they showed that increasing the surface O coverage and keeping the CO surface coverage constant on Ru(0001), there is a small increase in the adsorption strength of CO atop Ru site. They had attributed this increase to the destabilization of clean Ru atoms as the coverage of O increases at the neighboring sites and this destabilization make them more favorable for CO adsorption.

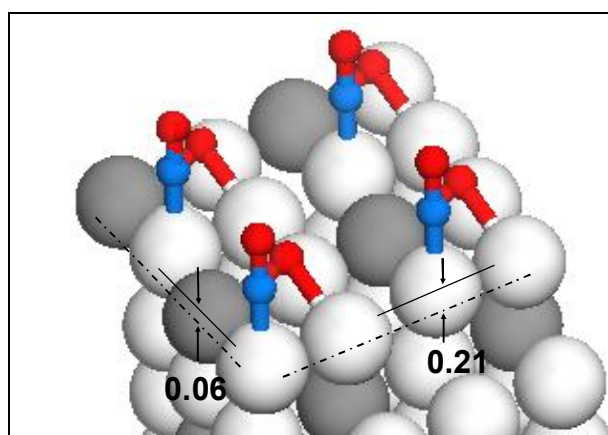


Figure 4.24. Surface structure at CO-atop Pt/O-fcc Pt₂Sn coadsorption on Pt₃Sn(111). The lines indicate the positions of the Pt atom under CO and Sn atom under O with respect to other two Pt atoms.

CO oxidation on transition metal surfaces generally follows the Langmuir-Hinshelwood mechanism, in which the initial step is adsorption of the reactants, CO and O, on the metal surface. Considering O₂ dissociation is easy on clean surfaces/at low surface coverages and the highest total surface coverage used in the current study is $\theta=0.5$, the coadsorption analysis in the current study is limited to involve atomic O and molecular CO coadsorbed on Pt₃Sn. For the CO oxidation reaction to proceed, the reactants should then be activated from the initial coadsorption structure to the transition state. The stability of

coadsorption structure, in this respect, would establish a barrier to activation and the fluctuations in the energy of coadsorption structures with changing CO and O coverages would probably effect the activation barrier of CO oxidation reaction. The experimental works on the kinetics of CO oxidation on Pt(111) clearly show that there is a change in the rate determining step (RDS) of CO oxidation depending on the surface CO coverage [161]; at high CO surface coverage, CO desorption is reported as RDS, on the other hand, as CO is consumed in the oxidation reaction and its coverage decreases, surface reaction between adsorbed CO and O becomes RDS. The change in the kinetics seems to be led by the relative weakness of O adsorption on monometallic surfaces as well as the need of two vacant sites for O atoms upon their dissociative adsorption [162]. Our co-adsorption studies give hints that on Pt₃Sn alloy surface, relative levels of CO and O coverages will play a major role on CO oxidation kinetics; when oxygen molecule is adsorbed dissociatively on CO precovered surface having a low CO coverage (i.e. 0.125 ML), the CO adsorption strength first decreases due to O coadsorption and then, as the O coverage increases, CO adsorption strength increases. On the other hand, if oxygen molecule dissociation occurs on CO precovered surface with a CO coverage of 0.25 ML, CO adsorption strength first decreases and then is not affected much from further O atom coadsorption. We believed that the reported change in CO adsorption energy as a response to O/CO ratio on the alloy surface is a significant contribution to catalysis research; that result should be considered in planning theoretical and experimental studies on CO oxidation -or other reactions- over alloy surfaces. Further research on CO oxidation reaction over Pt₃Sn surfaces is needed in order to shed light on this issue.

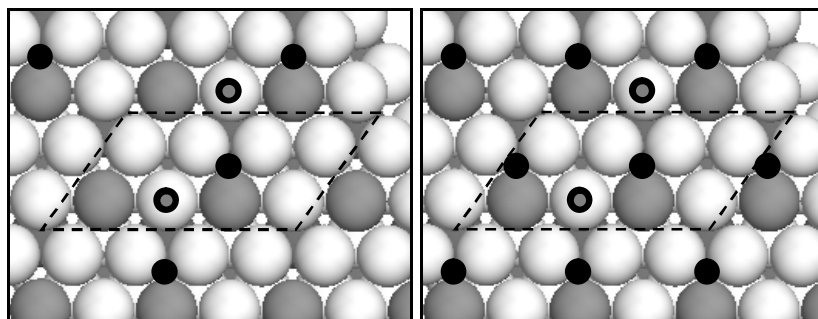


Figure 4.25. CO-atop Pt/O-fcc Pt₂Sn coadsorption structure at a total surface coverage of (a) 0.25 ML (CO+O) (b) 0.375 ML (CO+2O) Small black and gray-over-black balls represent O and CO, respectively. Bigger dark and light balls at the sublayer represent Sn and Pt, respectively.

Table 4.14. Calculated CO and O adsorption energies as a function of surface coverage (θ)

Description	θ_{CO}	θ_{total}	$E_{\text{ads}}(\text{eV})^*$	$E_{\text{ads}}(\text{eV})$	$\Delta E(\text{eV})$
CO-atop Pt (CO)	0.125	0.125	-1.76	-1.76	-
CO-atop Pt/O-fcc Pt2Sn (CO+O)	0.125	0.25	-5.65	-1.56	-0.21
CO-atop Pt/O-fcc Pt2Sn (CO+2O)	0.125	0.375	-9.49	-1.66	-0.11
CO-atop Pt/O-fcc Pt2Sn (2CO+2O)	0.25	0.5	-10.97	-1.57	-0.06
CO-atop Pt (2CO)	0.25	0.25	-3.27	-1.63	-
CO-atop Pt/O-fcc Pt2Sn (2CO+O)	0.25	0.375	-7.21	-1.56	-0.07

Total coadsorption energy as denoted by * in Table 4.14 of (mCO+nO) structure is calculated by using the equation:

$$E^{\text{mCO+nO+slab}} - (E^{\text{slab}} + mE_{\text{CO}}^{\text{free}} + nE_{\text{O}}^{\text{free}}) \quad (4.14)$$

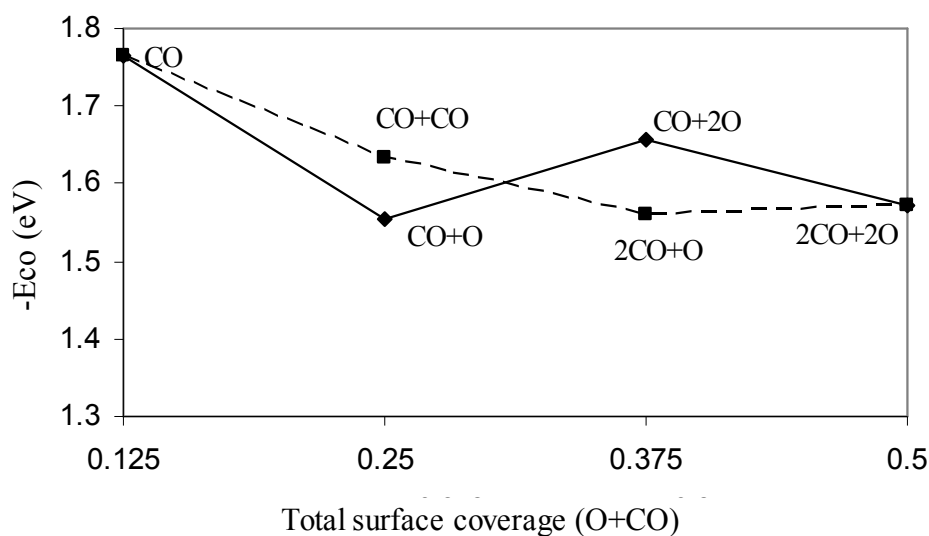


Figure 4.26. The adsorption energy of CO as a function of total coverage (CO+O)

4.4.5. Summary

Adsorption of CO and coadsorption of O and CO on Pt₃Sn(111) was studied using periodic DFT calculations. Calculations were performed on Pt(111) by using the same set of parameters and their results were used as reference basis. The calculations showed that the most stable configuration with the minimum energy for coadsorption of CO and O is

CO adsorbed atop Pt and O adsorbed on fcc Pt₂Sn hollow site and that the decrease in the adsorption strength of the system at a total surface coverage of 0.5 ML is by 0.06 eV as a result of coadsorption, with respect to the adsorption of one species individually. Results show that the interaction between the adsorbed CO and O is short range on PtSn alloy, contrary to that on pure Pt, and this is mainly related to stronger Sn-O bonds compared to Pt-O bonds which eventually reduce the surface strain at the coadsorption structure. There is a pronounced effect of total surface concentration on the adsorption energy of coadsorbed species; the adsorption strength is not directly proportional to the surface coverage but is also related to the distribution of the coadsorbed species on the surface.

5. CONCLUSIONS AND RECOMMENDATIONS

5.1. Conclusions

- i. Pt deposition onto Ni(111) substrate leads to Pt diffusion into Ni surface and formation of Pt-Ni mixed surface alloys. DFT calculations showed that there is an energy decrease led by Pt substitution of surface Ni atoms over the Ni(111) substrate. This energy decrease is related to the large surface tensile stress of Ni(111) which is reduced by Pt substitution. Additionally, the compression between lateral Pt-Pt bonds of Pt clusters adsorbed on Ni(111), caused by the size mismatch between the two elements, favor the Pt-Ni mixing.
- ii. Pt-Ni mixing in the bulk, rather than in the surface layer is not energetically favored unless the surface is under a great compressive stress, which may be caused by high Pt concentration in the surface or by oxygen chemisorption.
- iii. Oxygen chemisorption on Pt-Ni mixed surface alloy is not as strong as that on monometallic Ni(111) surface. Oxygen chemisorption is accompanied with electron transfer from surface metal atoms to oxygen adatom. Ni atoms supply these electrons from the valance s and p orbitals weakening the lateral metal-metal surface atoms. As monometallic Ni(111) surface is under tensile stress, the electron transfer to oxygen leads to stabilization of the surface, whereas compressive stress starts to be effective on Pt-Ni surface alloys and this decreases the stability of the chemisorption system.
- iv. DFT calculations confirm the experimental studies which showed that Pt-Ni mixing results in formation of surface alloys and these surface alloys have a tendency to preserve their metallic reduced state contrary to single crystal Ni surface under oxygen presence. The high oxygen affinity of monometallic Ni reduces its OSR activity in the presence of oxygen as it is easily oxidized and requires the use of high operating temperatures to stay in metallic form. Pt-Ni bimetallic catalyst, on the other hand, has higher activity in OSR because its oxygen affinity is lower and thus, Pt-Ni bimetallic catalyst keeps its reforming activity even at low temperature.

- v. The activation barrier of CH₄ dehydrogenation is smaller on the Pt-Ni bimetallic surface alloy than on the monometallic Ni(111) surface. On Pt-Ni alloy, the reaction proceeds on the Pt site and the adsorption energy of CH₃ on Pt is lower compared to that on Ni. As Pt sites are not as easily oxidized as Ni sites, these Pt atoms on the Ni surface may act as special agents to produce hydrogen. These hydrogen atoms are then used to reduce the NiO species via hydrogen spillover effect. The overall results confirm that Pt-Ni surface alloys can be reduced to metallic state at lower temperatures, compared to monometallic Ni, and this is one of the reasons of increased catalytic activity and enhanced stability of Pt-Ni bimetallic catalyst in the OSR of hydrocarbons.

- vi. CO adsorbs preferably with a linear structure on Pt(111) surface and, this is accompanied with a change in the electronic structure of the surface Pt atoms, not only those coordinated with CO but also the bare neighboring ones. This reconstruction in the electronic structure of bare Pt atoms seems to favor the atop-adsorption of CO as coverage increases and thus conducting to the formation a ($\sqrt{3} \times \sqrt{3}$)R30° pattern with all the CO are linearly adsorbed. Above 0.33 ML surface coverage, direct repulsive forces between adsorbed CO molecules start to be effective due to the decreased distance between CO molecules. Above that coverage limit, bridge site adsorption becomes more stable than atop adsorption, and only those bridge sites which increase the adsorbate-adsorbate distance and consequently decrease the direct repulsive forces become stable.

- vii. On Pt₃Sn(111), contrary to that on monometallic Pt, adsorbed CO does not cause any change in the electronic structure of neighbor bare surface atoms. This may be related to the narrower conduction band of the alloy due the presence of tin, which is an electron donor to Pt atoms. AER-DFT calculations give the site preference for CO adsorption in parallel to experimental studies, i.e. atop adsorption followed by multifold adsorption, which has not yet been proven previously by any computational studies. However, the difference between the adsorption energy of these sites is very small. On the contrary to the observation on Pt(111) surface, the flat potential energy surface, accompanied with the lack of a lateral adsorbate interaction, enables the occupation of multifold adsorption sites along with linear adsorption on Pt-Sn alloy.

- viii. The interaction of CO and O at a coadsorption structure of (CO+O) with a total surface coverage of 0.5 ML is weak on Pt₃Sn(111). Effect of coadsorption is less pronounced on Pt₃Sn(111) than it is on Pt(111). One of the reasons is that surface corrugation is more on the alloy surface even after coadsorption and this reduces the strain effect which weakens CO adsorption on Pt(111).
- ix. The most stable site for O adsorption on Pt₃Sn(111) is fcc Pt₂Sn site. O adsorption on this site is stronger than it is on the most stable site on Pt(111), i.e. fcc Pt₃ site, by 0.06 eV. Strong Sn-O bonds of fcc Pt₂Sn site on Pt₃Sn(111) is the reason of strong O adsorption on Pt₃Sn(111). As CO molecules do not adsorb on Sn sites, the competition between CO and O for the same adsorption sites are prevented. This is one of the reasons for increased activity of Pt-Sn alloys in the PROX reaction, especially at reduced temperatures.
- x. Adsorption energy of CO is not only a function of the number of adsorbed O atoms around in the neighborhood but also on the distribution of them and the relative surface concentrations of the species. A uniform distribution of adsorbed O around CO increases the magnitude of CO adsorption energy when the surface coverage of O is increased from 0.125 to 0.25 ML. As the activation barrier for CO oxidation reaction is dependent on the stability of the initial stage of the reaction, the changes in the coadsorption energy with different surface concentrations would eventually affect the rate of the reaction.

5.2. Recommendations

According to the results of the present study, the following points are thought to be beneficial for the future studies:

- i. The results of the current study has shown that Pt-Ni surface alloys have chemical properties that are suitable to enhance the catalytic activity in OSR. Oxygen adsorption is weaker on Pt-Ni alloys and methane dehydrogenation reaction proceeds on Pt sites, which are not easily oxidized. It is proposed that some of these properties are related to the low surface stress of Pt-Ni surface alloys. To explore this possibility

further, it is possible to analyze the reaction kinetics in a similar way on Pt-Ni bulk alloys, which may be in the form of Ni₃Pt composition. In contrary to surface alloys, Ni₃Pt alloy surface is under a large tensile stress and in this way, it may be possible to fully understand the influence of surface stress on the catalytic activity. However, it should be noted that formation of Pt-Ni bulk alloy has never been observed by the previous experimental studies.

- ii. Current developments in the computer technology has enhanced the efficiency of computational calculations. It has been possible to benefit from this enhancement for the last five years, throughout which the work forming the basis of the current thesis has been conducted. With the reduction of computational time, it has been possible to study more difficult models that are more realistic and resembling the physical conditions better. In the future work, with the development of computational power further, it is possible to take advantage of this advancement to study bimetallic active catalyst sites which have not been explored experimentally and, to use the knowledge obtained from the calculations as a starting point for future experimental work. For instance, depending on the work proposed in (i), it may be suitable to question the activity of Pt-Ni bulk alloys in OSR and investigate suitable catalyst preparation methods which would result in the formation of such alloy active sites on the catalyst surface. It is still a requirement to combine the computational and experimental findings to be able to reach sound conclusions.
- iii. It was proposed that weak surface stress on Pt-Ni surface alloys is a reason of decreased oxygen chemisorption strength on these surface structures. The smaller surface stress, on the other hand, is related to the larger metallic radius of Pt compared to Ni. Because Pd is a column 10 metal, like Pt and has a metallic radius closer to Pt, the work may be further expanded to include Pd-Ni alloys and additionally, similar studies may be conducted for other metals at different columns of the periodic table. For example, it is possible to study Au-Ag systems, or similar, although for different reasons, these systems might not show any catalytic activity in OSR. The aim here is to provide the fundamental knowledge which might be useful in the future for different reaction systems.

- iv. The changes in the chemisorption stability at different CO/O relative coverages hint that the reaction kinetics can be influenced by the presence of adsorbed reactants/species in the neighbourhood of the reaction sites, although these species do not enter the reaction directly. This may be especially important to understand the reaction kinetics with changing partial pressures of the reactants. So, CO oxidation reaction can be studied on monometallic Pt and Pt-Sn bimetallic alloys with different relative concentrations of CO and O adsorbed on the surface. The activation energy values found in this way may provide information on the changes in the reaction rate between O-precovered or CO-precovered catalyst surfaces. This is especially important for CO-precovered Pt(111) surface, as the results imply that the reaction can proceed only at the borders of CO clusters at low temperature.

APPENDIX A: TRANSITION STATE SEARCH FOR CH₄ DEHYDROGENATION

In this Appendix, the transition state (TS) calculations for the methane dehydrogenation reaction on Pt-Ni surface alloy is given as an example, to show the details of LST/QST transition state search method.

Starting from the initial guesses for the reactants and products, LST/QST method interpolates a reaction pathway to find the TS. After the TS is determined, TS Confirmation tool is used to verify that the TS calculated connects the reactant and product as expected. If there are any other stationary points between the TS and the reactant/product, then it is necessary to perform a geometry optimization to refine the geometry of these minima.

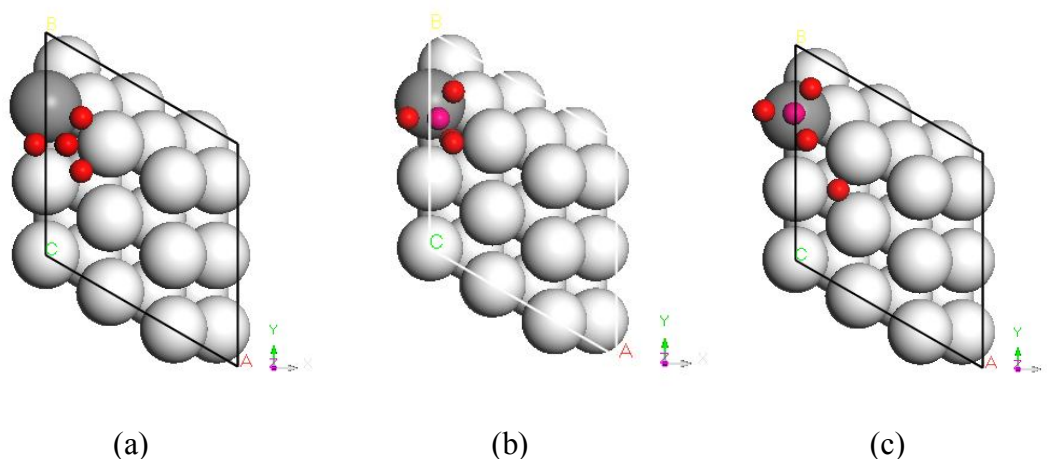


Figure A.1. (a) Initial guess for the reactant structure (b) the calculated transition state after the first LST calculation (c) Initial guess for the product structure.

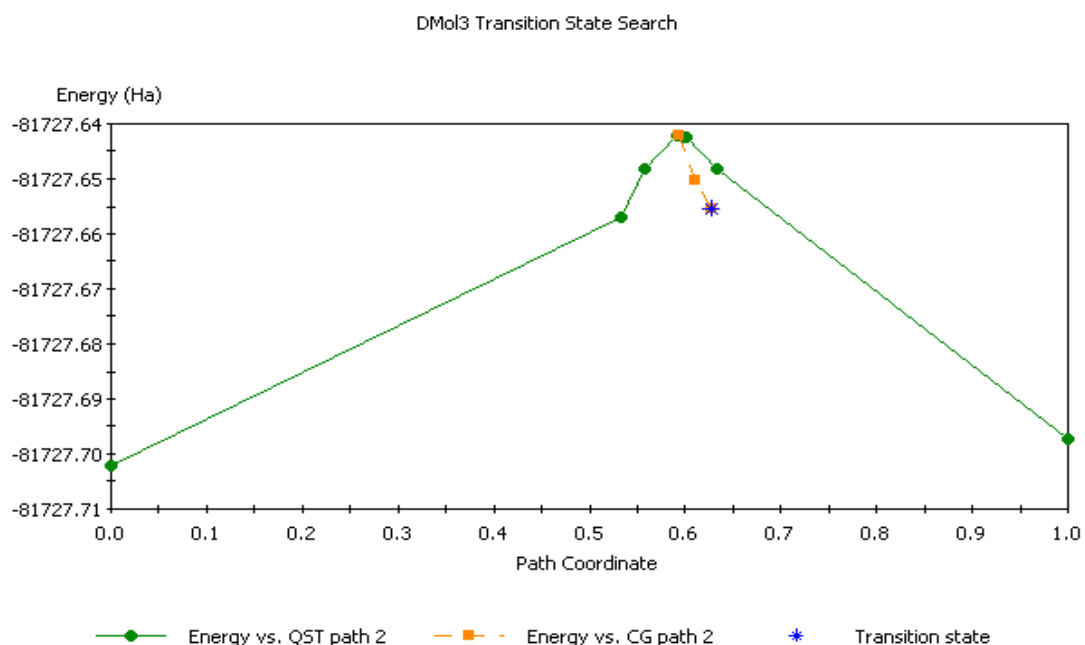


Figure A.2. The calculated energy versus reaction coordinate after the first LST/QST calculation

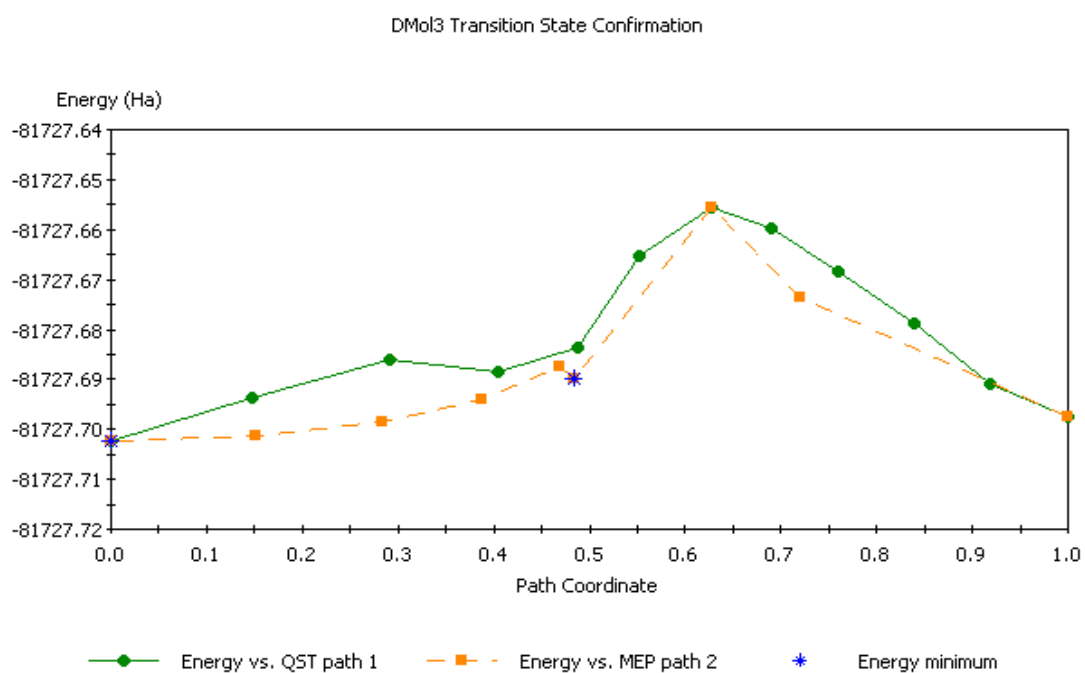


Figure A.3. The optimized reaction path by “TS Confirmation” tool. The energy minimum between the reactant structure and the product structure designates the fact that the reactant structure is not directly connected to the transition state and there is a need for a second LST/QST calculation.

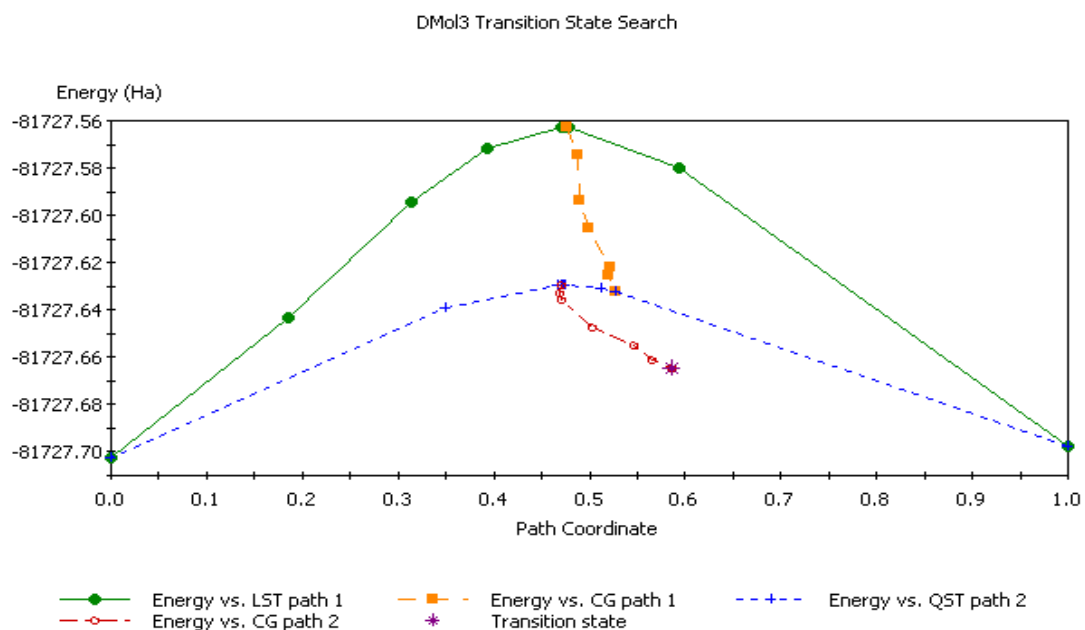


Figure A.4. The calculated energy versus reaction coordinate after the second LST/QST calculation. A new guess for the reactant structure is entered based on the results of TS Confirmation calculation.

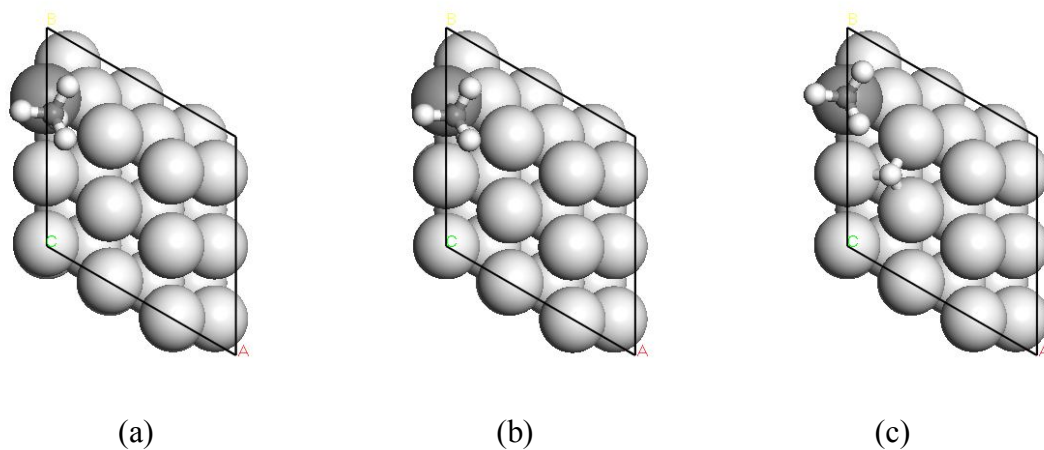


Figure A.5. The final optimized reaction path: (a) reactant structure (b) transition state (c) product structure

APPENDIX B: RELATIVISTIC EFFECTS ON CO ADSORPTION

In this Appendix, the influence of relativistic effects on the electronic and chemical properties of heavy transition metals is shown with an example. Pt(111) system is optimized with Dmol3 using two different core treatment methods, in series. One of these methods is "All Electron (AE)" which provides no special treatment of cores. The other one is "All Electron Relativistic (AER)" which introduces some scalar relativistic effects into the core.

Due to the relativistic effects, the s orbitals and additionally the p electrons of the Pt atoms shrunk, which causes the electronic distribution at these Pt atoms to concentrate at lower energy values (Figure B.1). During CO adsorption, the mixing between CO molecular orbitals and metal states increases. The metal-derived CO molecular orbitals are more stabilized as a result of scalar relativistic effects. At the end, the stabilization at CO molecular orbitals results in stronger CO adsorption on Pt(111). The difference between the CO adsorption strength on Pt(111) obtained with AER and AE calculations is as high as 0.77 eV, the initial being the higher (Figure B.2).

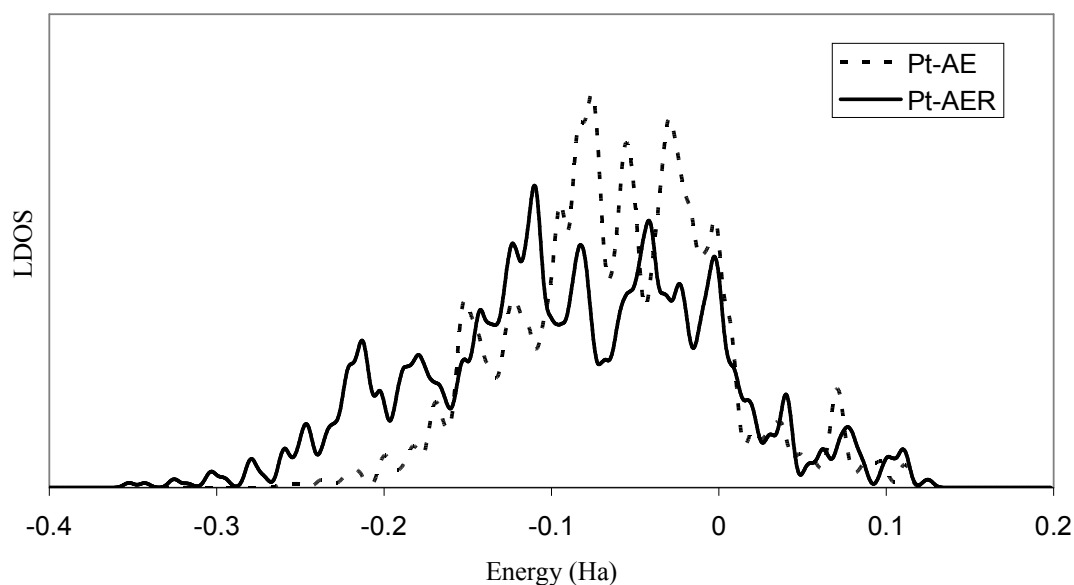


Figure B.1. LDOS at surface Pt atom of the Pt(111) system. Electron distribution obtained with AER calculations is concentrated at lower energy values, compared with those obtained with AE calculations.

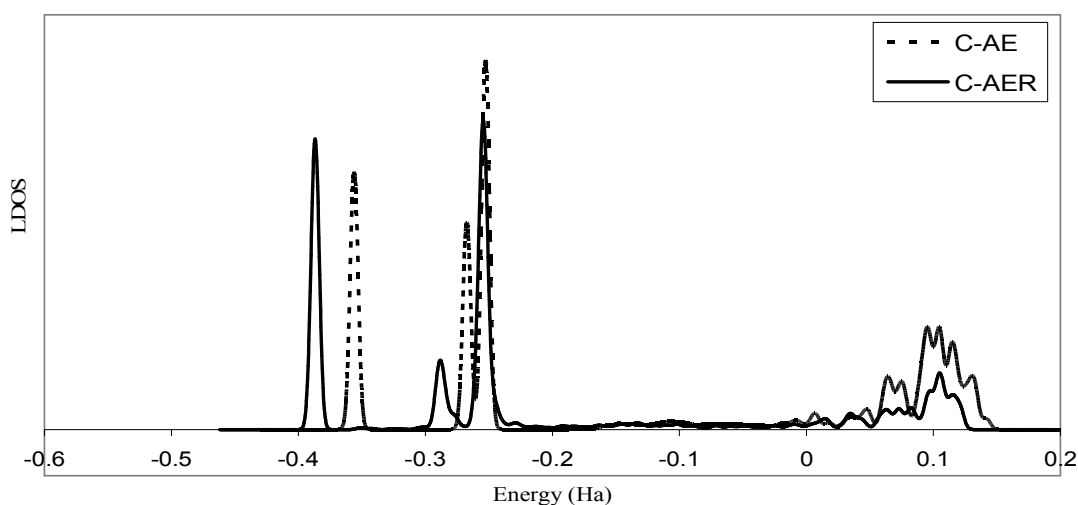


Figure B.2. LDOS at C atom for the CO/Pt(111) system. C molecular orbitals are at lower energy values for AER calculations, compared with those obtained with AE calculations.

Calculations using plane-wave basis sets with ultrasoft pseudopotentials generally result in a wrong site preference for CO adsorption on Pt and Pt-based alloys; the hollow sites are given to be the most favorable sites for adsorption, although experimentally it has been proven that linear adsorption is the most stable structure. Plane-wave calculations do not take into account the relativistic effects in an accurate way. As a result, the electron distribution obtained with this method is concentrated at higher energy values than that obtained with AER calculations (Figure B.3).

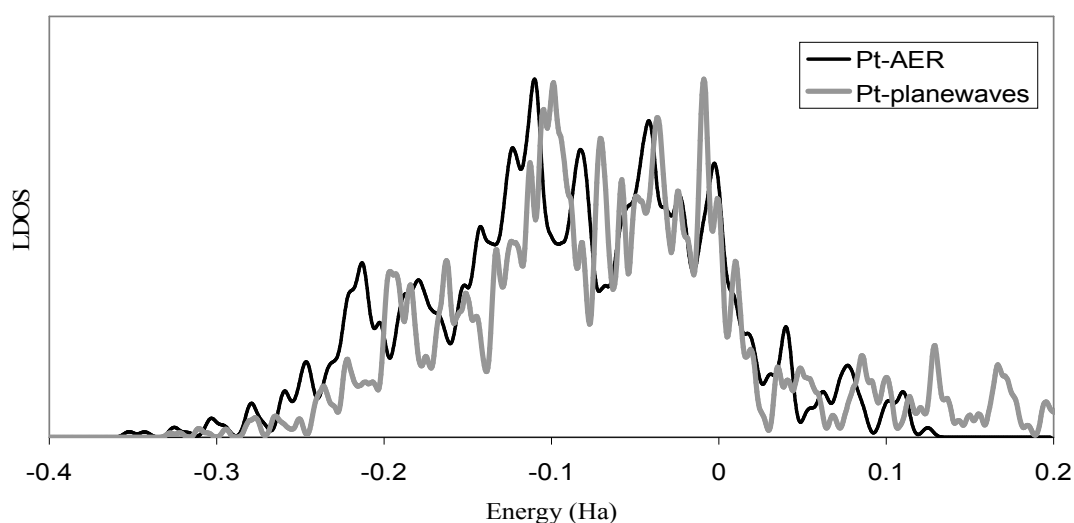


Figure B.3. LDOS at surface Pt atom of the Pt(111) system. Electron distribution obtained with AER calculations is concentrated at lower energy values, compared with those obtained with plane-wave basis sets and ultrasoft pseudopotentials.

REFERENCES

1. Franco, A. and A. R. Diaz, "The future challenges for, "clean coal technologies": Joining efficiency increase and pollutant emission control", *Energy*, Vol. 34, No. 3, pp. 348-354, 2009.
2. Ghenciu, A. F., "Review of fuel processing catalysts for hydrogen", *Opinion in Solid State and Materials Science*, Vol. 6, No. 5, pp. 389-399, 2002.
3. Kirubakaran, A., S. Jain and R.K. Nema, "A review on fuel cell technologies and power electronic interface", *Renewable and Sustainable Energy Reviews*, Vol. 13, No. 9, pp. 2430-2440, 2009.
4. Beér, M., "High efficiency electric power generation: The environmental role", *Progress in Energy and Combustion Science*, Vol. 33, No. 2, pp. 107–134, 2007.
5. *International Energy Outlook Report #:DOE/EIA-0484*, United States Department of Energy, 2009.
6. Andújar, J. M. and F. Segura, "Fuel cells: History and updating. A walk along two centuries", *Renewable and Sustainable Energy Reviews*, Vol. 13, No. 9, pp. 2309-2313, 2009.
7. *Hydrogen Program "Record 5020: Reduction in Fuel Consumption with FCVs,"* United States Department of Energy, http://www.hydrogen.energy.gov/program_records.html, 2009.
8. Rostrup-Nielsen, J. R., "Conversion of hydrocarbons and alcohols for fuel cells", *Physical Chemistry Chemical Physics*, Vol. 3, No.3, pp. 283-291, 2001.
9. Rostrup-Nielsen, J.R., I. Dybkjaer and T.S. Christensen, "Steam reforming of liquid hydrocarbons", *Studies in Surface Science and Catalysis*, Vol. 113, pp. 81-95, 1998.

10. Shu, Y., L. E. Murillo, J. P. Bosco, W. Huang, A. I. Frenkel and J. G. Chen, "The effect of impregnation sequence on the hydrogenation activity and selectivity of supported Pt/Ni bimetallic catalysts", *Applied Catalysis A: General*, Vol. 339, No. 2, pp. 169-179, 2008.
11. Nikolla, E., J. Schwank and S. Linic, "Comparative study of the kinetics of methane steam reforming on supported Ni and Sn/Ni alloy catalysts: The impact of the formation of Ni alloy on chemistry", *Journal of Catalysis*, Vol. 263, No. 2, pp. 220-227, 2009.
12. Egeberg, R. C., S. Ullmann, I. Alstrup, C. B. Mullins and I. Chorkendorff, "Dissociation of CH₄ on Ni(111) and Ru(0001)", *Surface Science*, Vol. 497, No. 1-3, Pages 183-193, 2002.
13. Cui, Y., H. Xu, Q. Ge, Y. Wang, S. Hou and W. Li, "Structure sensitive dissociation of CH₄ on Ni/ α -Al₂O₃: Ni nano-scale particles linearly compensate the E_a and ln A for the CH₄ pulse kinetics", *Journal of Molecular Catalysis A: Chemical*, Vol. 249, No. 1-2, pp. 53-59, 2006.
14. Bengaard, H. S., J. K. Nørskov, J. Sehested, B. S. Clausen, L. P. Nielsen, A. M. Molenbroek and J. R. Rostrup-Nielsen, "Steam Reforming and Graphite Formation on Ni Catalysts", *Journal of Catalysis*, Vol. 209, No. 2, Pages 365-384, 2002.
15. Abild-Pedersen, F., O. Lytken, J. Engbæk, G. Nielsen, I. Chorkendorff and J. K. Nørskov, "Methane activation on Ni(111): Effects of poisons and step defects", *Surface Science*, Vol. 590, No. 2-3, pp. 127-137, 2005.
16. Li, D., K. Nishida, Y. Zhan, T. Shishido, Y. Oumi, T. Sano and K. Takehira, "Superior catalytic behavior of trace Pt-doped Ni/Mg(AlO) in methane reforming under daily start-up and shut-down operation", *Applied Catalysis A: General*, Vol. 350, No. 2, pp. 225-236, 2008.
17. Li, B., S. Kado, Y. Mukainakano, T. Miyazawa, T. Miyao, S. Naito, K. Okumura, K. Kunimori and K. Tomishige, "Surface modification of Ni catalysts with trace Pt for

- oxidative steam reforming of methane”, *Journal of Catalysis*, Vol. 245, pp. 144-155, 2007.
18. Ladebeck, J. R. and J. P. Wagner, “Handbook of Fuel Cells – Fundamentals, Technology and Applications Vol. 3: Fuel Cell Technology and Applications”, in W. Vielstich, H. A. Gasteiger and A. Lamm (Eds), pp 190–201, John Wiley & Sons, West Sussex, 2003.
 19. Choudhary, T. V. and D. W. Goodman, “CO-free fuel processing for fuel cell applications”, *Catalysis Today*, Vol. 77, No. 1-2, Pages 65-78, 2002.
 20. Shore, L. and R. J. Farrauto “Handbook of Fuel Cells – Fundamentals, Technology and Applications Vol. 3: Fuel Cell Technology and Applications”, in W. Vielstich, H. A. Gasteiger and A. Lamm (Eds), pp. 211, John Wiley & Sons, West Sussex, 2003.
 21. Suh, D. J., C. Kwak, J. H. Kim, S. M. Kwon and T. J. Park, “Removal of carbon monoxide from hydrogen-rich fuels by selective low-temperature oxidation over base metal added platinum catalysts”, *Journal of Power Sources*, Vol. 142, No. 1-2, pp. 70–74, 2005.
 22. Panagiotopoulou P. and D. I. Kondarides, “Selective methanation of CO over supported noble metal catalysts: Effects of the nature of the metallic phase on catalytic performance”, *Applied Catalysis A: General*, Vol. 344, No. 1-2, pp. 45-54, 2008.
 23. Steininger, H., S. Lehwald and H. Ibach, “On the adsorption of CO on Pt(111)”, *Surface Science*, Vol. 123, No. 2-3, pp. 264-271, 1982.
 24. Hopster, H. and H. Ibach, “Adsorption of CO on Pt(111) and Pt 6(111) × (111) studied by high resolution electron energy loss spectroscopy and thermal desorption spectroscopy”, *Surface Science*, Vol. 77, No. 1, pp. 109-114, 1978.

25. Mieher, W. D., L. J. Whitman and W. Ho, "A time resolved electron energy loss spectroscopy study of CO on Pt(111): Adsorption site occupations versus coverage and temperature", *Journal of Chemical Physics*, Vol. 91, No. 5, pp. 3228-3240, 1989.
26. Pedersen, M. Ø., M. L. Bocquet, P. Sautet, E. Lægsgaard, I. Stensgaard and F. Besenbacher, "CO on Pt(111): binding site assignment from the interplay between measured and calculated STM images", *Chemical Physics Letters*, Vol. 299, No. 5, pp. 403-409, 1999.
27. Gülmen, M. A., A. Sümer and A. E. Aksoylu, "Adsorption properties of CO on low-index Pt₃Sn surfaces", *Surface Science*, Vol. 600, No. 21, pp. 4909-4915, 2006.
28. Feibelman, P.J., B. Hammer, J.K. Nørskov, F. Wagner, M. Scheffler, R. Stumpf, R. Watwe and J. Dumesic, "The CO/Pt(111) puzzle", *Journal of Physical Chemistry B*, Vol. 105, pp. 4018-4025, 2001.
29. Orita, H., N. Itoh and Y. Inada, "All electron scalar relativistic calculations on adsorption of CO on Pt(111) with full-geometry optimization: a correct estimation for CO site-preference", *Chemical Physics Letters*, Vol. 384, No.4-6, pp. 271-280, 2004.
30. Doll, K., "CO adsorption on the Pt(111) surface: a comparison of a gradient corrected functional and a hybrid functional", *Surface Science*, Vol. 573, No. 3, pp. 464-471, 2004.
31. Kresse, G., A. Gil and P. Sautet, "Significance of single-electron energies for the description of CO on Pt(111)", *Physical Review B*, Vol. 68, No. 7, pp. 073401-1 - 073401-8, 2003.
32. Liu, W., Y. F. Zhu, J. S. Lian and Q. Jiang, "Adsorption of CO on surfaces of 4d and 5d elements in group VIII", *Journal of Physical Chemistry C*, Vol. 111, No. 2, pp. 1005-1009, 2007.

33. Liu, X., O. Korotkikh and R. Farrauto, "Selective catalytic oxidation of CO in H₂: structural study of Fe oxide-promoted Pt/alumina catalyst", *Applied Catalysis A: General*, Vol. 226, No. 1-2 pp. 293-300, 2002.
34. Korotkikh, O. and R. Farrauto, "Selective catalytic oxidation of CO in H₂: fuel cell applications", *Catalysis Today*, Vol. 62, No. 2-3, pp. 249-260, 2000.
35. Aksoylu, A. E., M. M. A. Freitas and J. L. Figueiredo, "Bimetallic Pt-Sn catalysts supported on activated carbon. II. CO oxidation", *Catalysis Today*, Vol. 62, No. 4, pp. 337-346, 2000.
36. Aksoylu, A. E., M. M. A. Freitas and J. L. Figueiredo, "Bimetallic Pt-Sn catalysts supported on activated carbon: I. The effects of support modification and impregnation strategy", *Applied Catalysis A: General*, Vol. 192, No. 1, pp. 29-42, 2000.
37. Son, I. H. and A. M. Lane, "Promotion of Pt/ γ -Al₂O₃ by Ce for Preferential Oxidation of CO in H₂", *Catalysis Letters*, Vol. 76, No. 3-4, pp. 151-154, 2001.
38. Choi, J., C. B. Shin and D. J. Suh, "Co-promoted Pt catalysts supported on silica aerogel for preferential oxidation of CO Catalysis", *Communications*, Vol. 9, No. 5 pp. 880-888, 2008.
39. İnce, T., G. Uysal, A.N. Akın and R. Yıldırım, "Selective low-temperature CO oxidation over Pt-Co-Ce/Al₂O₃ in hydrogen-rich streams", *Applied Catalysis A: General*, Vol. 292, pp. 171-177, 2005.
40. Kwak, C., T.-J. Park and D. Jin Suh, "Effects of sodium addition on the performance of PtCo/Al₂O₃ catalysts for preferential oxidation of carbon monoxide from hydrogen-rich fuels", *Applied Catalysis A: General*, Vol. 278, No. 2, pp. 181-186, 2005.

41. Cho, S. H., J. S. Park, S. H. Choi and S. H. Kim, "Effect of magnesium on preferential oxidation of carbon monoxide on platinum catalyst in hydrogen-rich stream", *Journal of Power Sources*, Vol. 156, No. 2 pp. 260–266, 2006.
42. Liu, P., A. Logadottir, and J. K. Nørskov, "Modeling the electro-oxidation of CO and H₂/CO on Pt, Ru, PtRu and Pt₃Sn", *Electrochimica Acta*, Vol. 48, No. 25-26, pp. 3731-3742, 2003.
43. Liao, M. S., C. R Cabrera and Y. Ishikawa, "A theoretical study of CO adsorption on Pt, Ru and Pt–M (M=Ru, Sn, Ge) Clusters", *Surface Science*, Vol. 445, No. 2-3, pp. 267–282, 2000.
44. Paffett, M. T., S. C. Gebhard, R. G. Windham and B. E. Koel, "Chemisorption of carbon monoxide, hydrogen, and oxygen on ordered tin/platinum(111) surface alloys", *Journal of Physical Chemistry*, Vol. 94, No. 17, pp. 6831-6839, 1990.
45. Grass, K. and H. G. Lintz, "The Kinetics of Carbon Monoxide Oxidation on Tin(IV) Oxide Supported Platinum Catalysts", *Journal of Catalysis*, Vol. 172, No. 2, pp. 446–452, 1997.
46. Shubina, T. E. and M. T. M. Koper, "Quantum-chemical calculations of CO and OH interacting with bimetallic surfaces", *Electrochimica Acta*, Vol. 47, No. 22-23, pp. 3621-3628, 2002.
47. *Handbook on the Physics and Chemistry of Rare Earths*, in K.A. Gschneidner, Jr. and L. Eyring, V. Paul-Boncour, L. Hilare and A. Percheron-Guigan (eds.), Elsevier Science B. V, Vol. 29, Chapter 181, 2000.
48. Bardi, U., "The atomic structure of alloy surfaces and surface alloys", *Reports on Progress in Physics*, Vol. 57, No. 10, pp. 939-945, 1994.
49. Heid, R. and K. P. Bohnen, "Ab initio lattice dynamics of metal surfaces", *Physics Reports*, Vol. 387, No. 5-6, pp. 151–213, 2003.

50. Jia, Z., H. Jin, M. B. Sullivan, F. C. H. Lim and P. Wu, "Study of Pd-Au bimetallic catalysts for CO oxidation reaction by DFT calculations", *Physical Chemistry Chemical Physics*, Vol. 11, No. 9, pp. 1441–1446, 2009.
51. Ruban, A., B. Hammer, P. Stoltze, H. Skriver, and J. Nørskov, "Surface electronic structure and reactivity of transition and noble metals", *Journal of Molecular Catalysis A: Chemical*, Vol. 115, No. 3, pp. 421–429, 1997.
52. Kitchin, J. R., J. K. Nørskov, J. G. Chen, and M. A. Barteau, "Modification of the surface electronic and chemical properties of Pt(111) by subsurface 3d transition metals", *Journal of Chemical Physics*, Vol. 120, No. 21, pp. 10240–10250, 2004.
53. Miller, S. D. and J. R. Kitchin, "Relating the coverage dependence of oxygen adsorption on Au and Pt fcc(111) surfaces through adsorbate-induced surface electronic structure effects", *Surface Science*, Vol. 603, No. 5 pp. 794–801, 2009.
54. Greeley, J. and J. K. Nørskov, "A general scheme for the estimation of oxygen binding energies on binary transition metal surface alloys", *Surface Science*, Vol. 592, No. 1–3 pp. 104–111, 2005.
55. Hammer, B. and J. K. Nørskov, "Electronic factors determining the reactivity of metal surfaces", *Surface Science*, Vol. 343, No. 3, pp. 211–220, 1995.
56. Hammer, B. and J. K. Nørskov, "Theoretical surface science and catalysis—calculations and concepts", *Advances in Catalysis*, Vol. 45, pp. 71–129, 2000.
57. Bligaard, T. and J. K. Nørskov, *Electrochimica Acta*, Vol. 52, pp. 5512–5516, 2007.
58. Lopez, N. and J. K. Nørskov, "Synergetic effects in CO adsorption on Cu–Pd(111) alloys", *Surface Science*, Vol. 477, No. 1 pp. 59–75, 2001.
59. Bertolini, J. C., "Surface stress and chemical reactivity of Pt and Pd overlayers", *Applied Catalysis A: General*, Vol. 191, No. 1–2, pp. 15–21, 2000.

60. Gibbs, J. W., “The Scientific Papers of J Willard Gibbs”, London: Longmans Green, 1906.
61. Haiss, W., “Surface stress of clean and adsorbate-covered solids”, *Reports on Progress in Physics*, Vol. 64 pp. 591–648, 2001.
62. Fiorentini, V., M. Methfessel and M. Scheffler, “Reconstruction mechanism of fcc transition metal (001) surfaces”, *Physical Review Letters*, Vol. 71, No. 7, pp. 1051-1054, 1993.
63. Kollar, J. and L. Vitos, “Calculation of surface stress for fcc transition metals”, *Physical Review B*, Vol. 68, No. 24, pp. 245417-1 - 245417-5 2003.
64. Umeno, Y., C. Elsässer, B. Meyer, P. Gumbsch, M. Nothacker, J. Weissmüller, and F. Evers, “Ab initio study of surface stress response to charging”, *Europhysics Letters*, Vol. 78, pp. 13001-13006, 2007.
65. Feibelman, P. J., “First-principles calculations of stress induced by gas adsorption on Pt(111)”, *Physical Review B*, Vol. 56, No. 4, pp. 2175-2182, 1997.
66. Stepanyuk, V. S., D. I. Bazhanov and W. Hergert, “Effect of impurities on surface stress on an atomic scale”, *Physical Review B*, Vol. 62, No. 7, pp. 4257- 4260, 2000.
67. Pala, G. R. S. and F. Liu, “Nature of reactive O₂ and slow CO₂ evolution kinetics in CO oxidation by TiO₂ supported Au cluster”, *Journal of Chemical Physics*, Vol. 120, No. 14, 144714-144719, 2004.
68. Mavrikakis, M., B. Hammer, and J. K. Nørskov, “Effect of Strain on the Reactivity of Metal Surfaces”, *Physical Review Letters*, Vol. 81, No. 13, pp. 2819-2823, 1998.
69. Xu, Y., A. V. Ruban, and M. Mavrikakis, “Adsorption and Dissociation of O₂ on Pt–Co and Pt–Fe Alloys”, *Journal of the American Chemical Society*, Vol. 126, No. 14, pp. 4717-4725, 2004.

70. Kitchin, J. R., J. K. Nørskov, M. A. Barteau, and J. G. Chen, "Role of Strain and Ligand Effects in the Modification of the Electronic and Chemical Properties of Bimetallic Surfaces", *Physical Review Letters*, Vol. 93, pp. 156801-156808, 2004.
71. Sotelo, J. C. and J. M. Seminario, "Local reactivity of O₂ with Pt₃ on Co₃Pt and related backgrounds", *Journal of Chemical Physics*, Vol. 128, No. 20, pp. 204701-204709, 2008.
72. Hehre, W. J., *A Guide to Molecular Mechanics and Quantum Chemical Calculations*, Wavefunction Inc., 2003.
73. Payne, M. C., M. P. Teter, D. C. Allan, T. A. Arias and J. D. Joannopoulos, "Iterative minimization techniques for ab initio total-energy calculations: molecular dynamics and conjugate gradients", *Reviews of Modern Physics*, Vol. 64, No. 4, pp. 1045-1097, 1992.
74. Hohenberg, P. and W. Kohn, "Inhomogeneous Electron Gas", *Physical Review*, Vol. 136, pp. B864-B870, 1964.
75. Kohn, W. and L. Sham, "Self-Consistent Equations Including Exchange and Correlation Effects", *Physical Review*, Vol. 140, No. 4A, pp. A1133-A1138, 1965.
76. Clark, S. J., M. D. Segall, C. J. Pickard, P. J. Hasnip, M. J. Probert, K. Refson and M. C. Payne, "First principles methods using CASTEP", *Zeitschrift für Kristallographie*, Vol. 220, No. 5-6, pp. 567-570, 2005.
77. Delley, B., "An all-electron numerical method for solving the local density functional for polyatomic molecules", *Journal of Chemical Physics*, Vol. 92, No. 1, pp. 508-518, 1990.
78. Delley, B., "From molecules to solids with the DMol3 approach", *Journal of Chemical Physics*, Vol. 113, No. 18, pp. 7756-7762, 2000.

79. Dirac, P. A. M., "The quantum theory of the electron", *Proceedings of the Royal Society A*, Vol. 117, pp. 610-624, 1928.
80. Bond, G. C., "Relativistic effects in coordination, chemisorption and catalysis", *Journal of Molecular Catalysis A: Chemical*, Vol. 156, No. 1-2, pp. 1-20, 2000.
81. Halgren, T. A. and W. N. Lipscomb, "The synchronous-transit method for determining reaction pathways and locating molecular transition states", *Chemical Physics Letters*, Vol. 49, No. 2, pp. 225-232, 1977.
82. Govind, N., M. Petersen, G. Fitzgerald, D. King-Smith and J. Andzelm, "A generalized synchronous transit method for transition state location", *Computational Materials Science*, Vol. 28, No. 2, pp. 250-258, 2003.
83. Henkelman, G. and H. Jónsson, "Improved tangent estimate in the nudged elastic band method for finding minimum energy paths and saddle points", *Journal of Chemical Physics*, Vol. 113, No. 22, pp. 9978-9985, 2000.
84. Monkhorst, H. J. and J. D. Pack, "Special points for Brillouin-zone integrations", *Physical Review B*, Vol. 13, No. 12, pp. 5188-5192, 1976.
85. Perdew, J. P., K. Burke and M. Ernzerhof, "Generalized Gradient Approximation Made Simple", *Physical Review Letters*, Vol. 77, No. 18 pp. 3865-3872, 1996.
86. Mulliken, R. S., "Electronic Population Analysis on LCAO-MO Molecular Wave Functions", *Journal of Chemical Physics*, Vol. 23, No. 10, pp. 1833-1840, 1955.
87. Caglayan, B. S., A. K. Avcı, Z. I. Onsan and A. E. Aksoylu, "Production of hydrogen over bimetallic Pt-Ni/ δ -Al₂O₃: I. Indirect partial oxidation of propane", *Applied Catalysis A: General*, Vol. 280, No. 2 pp. 181-188, 2005.
88. Caglayan, B. S., Z. I. Onsan and A. E. Aksoylu, "Production of hydrogen over bimetallic Pt-Ni/ δ -Al₂O₃: II. Indirect partial oxidation of LPG", *Catalysis Letters*, Vol. 102, No. 1-2, pp. 63-71, 2005.

89. Gökaliler, F., B. A. Göçmen and A. E. Aksoylu, "Hydrogen production by autothermal reforming of LPG for PEM fuel cell applications", *International Journal of Hydrogen Energy*, Vol. 33, No. 4 pp. 1383-1391, 2008.
90. Cabeza, G. F., N. J. Castellani and P. Légaré,, "Adhesion and bonding of Pt/Ni and Pt/Co overlayers: Density functional calculations", *Journal of Physics and Chemistry of Solids*, Vol. 67, No. 4, pp. 690-697, 2006.
91. Wan, J., Y. L. Fan, D. W. Gong, S. G. Shen and X. Q. Fan, "Surface relaxation and stress of fcc metals: Cu, Ag, Au, Ni, Pd, Pt, Al and Pb", *Modelling and Simulation in Materials Science and Engineering*, Vol. 7, pp. 189-196, 1999.
92. Harrison, M. J., D. P. Woodruff and J. Robinson, "Surface alloys, surface rumpling and surface stress", *Surface Science*, Vol. 572, No. 2-3 pp. 309-317, 2004.
93. Van Hardeveld, R. and A. Van Montfoort, "Infrared spectra of nitrogen adsorbed on nickel-on-aerosil catalysts: Effects of intermolecular interaction and isotopic substitution", *Surface Science*, Vol. 17, No. 1, pp. 90-124, 1969.
94. Stuckless, J. T. and C. E. Wartnaby, "Oxygen chemisorption and oxide film growth on Ni{100}, {110}, and {111}: Sticking probabilities and microcalorimetric adsorption heats", *Journal of Chemical Physics*, Vol. 106, No. 5, pp. 2012-2030, 1997.
95. Pedio, M., L. Becker, B. Hillert, S. D'Addato and J. Haase, "Oxygen on Ni(111): A multiple-scattering analysis of the near-edge x-ray-absorption fine structure", *Physical Review B*, Vol. 41, No. 11, pp. 7462-7466, 1990.
96. Chen, M., S. P. Bates, R. A. van Santen and C. M. Friend, "The chemical nature of atomic oxygen adsorbed on Rh(111) and Pt(111): A density functional study", *Journal of Physical Chemistry*, Vol. 101, No. 48 pp. 10051-10057, 1997.
97. Van Santen, R. A. and M. Neurock, *Molecular Heterogeneous Catalysis: A Mechanistic and Computational Approach*, pp. 105, VCH-Wiley, 2006.

98. Menning, C. A., H. H. Hwu and J. G. Chen, "Experimental and theoretical investigation of the stability of Pt-3d-Pt(111) bimetallic surfaces under oxygen environment", *Journal of Physical Chemistry*, Vol. 110, pp. 15471-15477, 2006.
99. Jelic, J. and R. J. Meyer, "A DFT study of pseudomorphic monolayer Pt and Pd catalysts for NO_x storage reduction applications", *Catalysis Today*, Vol. 136, No. 1-2, pp. 76-83, 2008.
100. Gsell, M., P. Jakob and D. Menzel, "Effect of substrate strain on adsorption", *Science*, Vol. 280, pp. 717-720, 1998.
101. Hyman, M. P. and J. W. Medlin, "Effects of electronic structure modifications on the adsorption of oxygen reduction reaction intermediates on model Pt(111)-alloy surfaces", *Journal of Physical Chemistry C*, Vol. 111, No. 45, pp. 17052-17060, 2007.
102. Parizotto, N. V., D. Zanchet, K. O. Rocha, C. M. P. Marques and J. M. C. Bueno, "The effects of Pt promotion on the oxi-reduction properties of alumina supported nickel catalysts for oxidative steam-reforming of methane: Temperature-resolved XAFS analysis", *Applied Catalysis A: General*, Vol. 366, No. 1, pp. 122-129, 2009.
103. Wei, J. and E. Iglesia, "Isotopic and kinetic assessment of the mechanism of reactions of CH₄ with CO₂ or H₂O to form synthesis gas and carbon on nickel catalysts", *Journal of Catalysis*, Vol. 224, No. 2, pp. 370-383, 2004.
104. Wang, S. G., D. B. Cao, Y. W. Li, J. Wang and H. Jiao, "Reactivity of surface OH in CH₄ reforming reactions on Ni(111): A density functional theory calculation", *Surface Science*, Vol. 603, No. 16, pp. 2600-2606, 2009.
105. Wang, L. G. and A. Zunger, "Why are the 3d-5d compounds CuAu and NiPt stable, whereas the 3d-4d compounds CuAg and NiPd are not", *Physical Review B*, Vol. 67, No. 9, pp. 092103-1 - 092103-4, 2003.

106. Bronsted, J. N., "Acid and Basic Catalysis", *Chemical Reviews*, Vol. 5, pp. 231-338, 1928.
107. Evans, M. G. and N. Polanyi, "Further considerations on the thermodynamics of chemical equilibria and reaction rates", *Transactions of the Faraday Society*, Vol. 32, pp. 1333-1360, 1936.
108. Haroun, M. F., P. S. Moussounda and P. Legare, "Theoretical study of methane adsorption on perfect and defective Ni(1 1 1) surfaces", *Catalysis Today*, Vol. 138, No. 1-2, pp. 77-83, 2008.
109. Yang, Q. Y., K. J. Maynard, A. D. Johnson and S. T. Ceyer, "The structure and chemistry of CH₃ and CH radicals adsorbed on Ni(111)", *Journal of Chemical Physics*, Vol. 102, No. 19, pp. 7734-7749, 1995.
110. Watwe, R. M., H. S. Bengaard, J. R. Rostrup-Nielsen, J. A. Dumesic and J. K. Nørskov, "Theoretical Studies of Stability and Reactivity of CH_x Species on Ni(111)", *Journal of Catalysis*, Vol. 189, No. 1, pp. 16-30, 2000.
111. Wang, S. G., D. B. Cao, Y. W. Li, J. Wang and H. Jiao, "CH₄ dissociation on Ni surfaces: Density functional theory study", *Surface Science*, Vol. 600, No. 16, pp. 3226-3234, 2006.
112. Michaelides, A. and P. Hu, "Methyl chemisorption on Ni(111) and C-H-M multicentre bonding: a density functional theory study", *Surface Science*, Vol. 437, No. 3, pp. 362-376, 1999.
113. Kua, J. and W. A. Goddard III., "Chemisorption of Organics on Platinum. 2. Chemisorption of C₂H_x and CH_x on Pt(111)", *Physical Chemistry B*, Vol. 102, No. 47, pp 9492-9500, 1998.
114. Ford, D. C., Y. Xu and M. Mavrikakis, "Atomic and molecular adsorption on Pt(111)", *Surface Science*, Vol. 587, No. 3, pp. 159-174, 2005.

115. Garegin, P., J. K. Nørskov, and R. Hoffmann, “A comparative theoretical study of the hydrogen, methyl, and ethyl chemisorption on the Pt(111) surface”, *Journal of American Chemical Society*, Vol. 122, No. 17, pp 4129–4144, 2000.
116. Christmann, K., R. J. Behm, G. Ertl, M. A. van Hove, and W. H. Weinberg, “Chemisorption geometry of hydrogen on Ni(111): Order and disorder”, *Journal of Chemical Physics*, Vol. 70, No. 9, pp. 4168-4184, 1979.
117. Richter, L. J. and W. Ho, “Vibrational spectroscopy of H on Pt(111): Evidence for universally soft parallel modes”, *Physical Review B*, Vol. 36, No. 18, pp. 9797-9800, 1987.
118. Olsen, R. A., G. J. Kroes and E. J. Baerends, “Atomic and molecular hydrogen interacting with Pt(111)”, *Journal of Chemical Physics*, Vol. 114, No. 24, pp. 11155-11163, 1999.
119. Jacob, T. and W. A. Goddard, III, “Adsorption of atomic H and O on the, (111) surface of Pt₃Ni alloys”, *Journal of Physical Chemistry B*, Vol. 108, No. 24, pp 8311–8323, 2004.
120. Watson, G. W., R. P. K. Wells, D. J. Willock and G. J. Hutchings, “A comparison of the adsorption and diffusion of hydrogen on the {111} surfaces of Ni, Pd, and Pt from density functional theory calculations”, *Journal of Physical Chemistry B*, Vol. 105, No. 21, pp 4889–4894, 2001.
121. Pillay, D. and M. D. Johannes, “Comparison of sulfur interaction with hydrogen on Pt(111), Ni(111) and Pt₃Ni(111) surfaces: The effect of intermetallic bonding”, *Surface Science*, Vol. 602, No. 16, pp. 2752-2757, 2008.
122. Medlin, J. W. and M. D. Allendorf, “Theoretical study of the adsorption of acetylene on the, (111) surfaces of Pd, Pt, Ni, and Rh”, *Journal of Physical Chemistry B*, Vol. 107, No. 1, pp 217–223, 2003.

123. Cui, Y., H. Zhang, H. Xu and W. Li, "Kinetic study of the catalytic reforming of CH₄ with CO₂ to syngas over Ni/ α -Al₂O₃ catalyst: The effect of temperature on the reforming mechanism", *Applied Catalysis A: General*, Vol. 318, pp. 79–88, 2007.
124. Abild-Pedersen, F., J. Greeley and J. K. Nørskov, "Understanding the effect of steps, strain, poisons, and alloying: Methane activation on Ni surfaces", *Catalysis Letters*, Vol. 105, No.: 1-2, pp. 9-13, 2005.
125. Wang, S. G., X. Y. Liao, J. Hu, D. B. Cao, Y. W. Li, J. W. and H. Jiao, "Kinetic aspect of CO₂ reforming of CH₄ on Ni(111): A density functional theory calculation", *Surface Science*, Vol. 601, No. 5, pp. 1271-1284, 2007.
126. Özkara, Ş. and A. E. Aksoylu, "Selective low temperature carbon monoxide oxidation in H₂-rich gas streams over activated carbon supported catalysts", *Applied Catalysis A: General*, Vol. 251, No. 1 pp. 75-83, 2003.
127. Sümer, A. and A. E. Aksoylu, "CO and O coadsorption on Pt₃Sn studied by DFT: Changes in the adsorptive properties of the surface with alloying and coverage", *Surface Science*, Vol. 602, No. 9 pp. 1636-1642, 2008.
128. Sümer, A., M. A. Gülmen and A. E. Aksoylu, "A theoretical investigation on Pt₃Sn(1 0 2) surface alloy and CO–Pt₃Sn(1 0 2) system", *Surface Science*, Vol. 600, No. 10, pp. 2026-2039, 2006.
129. Blyholder, G., "Molecular Orbital View of Chemisorbed Carbon Monoxide", *Journal of Physical Chemistry*, Vol. 68, No. 10, pp. 2772 -&, 1964
130. Atrei, A., U. Bardi, G. Roviola, M. Torrini, E. Zanazzi and P. N. Ross, "Structure of the, (001)- and, (111)-oriented surfaces of the ordered fcc Pt₃Sn alloy by low-energy-electron-diffraction intensity analysis", *Physical Review B*, Vol. 46, No. 3, pp. 1649-1654, 1992.

131. Yeo, Y. Y., L. Vattuone and D. A. King, "Calorimetric heats for CO and oxygen adsorption and for the catalytic CO oxidation reaction", *Journal of Chemical Physics*, Vol. 106, No. 1, 392-402, 1997.
132. Abild-Pedersen, F. and M.P. Andersson, "CO adsorption energies on metals with correction for high coordination adsorption sites – A density functional study", *Surface Science*, Vol. 601, No. 7, pp. 1747-1753, 2007.
133. Watwe, R. M., B. E. Spiewak, R. D. Cortright and J. A. Dumesic, "Density functional theory (DFT) and microcalorimetric investigations of CO adsorption on Pt clusters", *Catalysis Letters*, Vol. 51, No. 3-4, pp. 139-147, 1998.
134. Brako, R. and D. Šokčević, "Adsorbate-induced substrate relaxation and the adsorbate–adsorbate interaction", *Surface Science*, Vol. 469, No. 2-3, pp. 185-195, 2000.
135. Sung, S. and R. Hoffmann, "How carbon monoxide bonds to metal surfaces", *Journal of American Chemical Society*, Vol. 107, No. 3, pp. 578-587, 1985.
136. Einstein, T. L., in Unertl W. N. (eds.) *Handbook of surface science*, Vol. I, Chapter 11, Elsevier, Amsterdam, 1996.
137. Jennison, D. R., P. A. Schultz and M. P. Sears, "Ab Initio Ammonia and CO Lateral Interactions on Pt(111)", *Physical Review Letters*, Vol. 77, No. 23, pp. 4828-4831, 1996.
138. Ogletree, D. F., M. A. van Hove and G. A. Somorjai, "LEED intensity analysis of the structures of clean Pt(111) and of CO adsorbed on Pt(111) in the $c(4 \times 2)$ arrangement", *Surface Science*, Vol. 173, No. 2-3, pp. 351-365, 1986.
139. Dupont, C., D. Loffreda, F. Delbecq and Y. Jugnet, "Vibrational Study of CO Chemisorption on the Pt₃Sn(111)-(2×2) Surface", *Journal of Physical Chemistry C*, Vol. 111, No. 24, pp. 8524-8531, 2007.

140. Wong, Y. T. and R. Hoffmann, "Chemisorption of carbon monoxide on three metal surfaces: nickel(111), palladium(111), and platinum(111): a comparative study", *Journal of Physical Chemistry*, Vol. 95, No. 2, pp. 859-867, 1991.
141. Buatier de Mongeot, F., M. Scherer, B. Gleich, E. Kopatzki and R. J. Behm, "CO adsorption and oxidation on bimetallic Pt/Ru(0001) surfaces – a combined STM and TPD/TPR study", *Surface Science*, Vol. 411, No. 3, pp. 249-262, 1998.
142. Chin, S. Y., O. S. Alexeev and M. D. Amiridis, "Structure and reactivity of Pt–Ru/SiO₂ catalysts for the preferential oxidation of CO under excess H₂", *Journal of Catalysis*, Vol. 243, No. 2, pp. 329-339, 2006.
143. Von Schenck, H., E. Janin, O. Tjernberg, M. Svensson and M. Göthelid, "CO bonding on tin modified Pt(1 1 0)-(1×2)", *Surface Science*, Vol. 526, No. 1-2, pp. 184-192, 2003.
144. Schubert, M. M., M. J. Kahlich, G. Feldmeyer, M. Hüttner, S. Hackenberg, H. A. Gasteiger and R. J. Behm, "Bimetallic PtSn catalyst for selective CO oxidation in H₂-rich gases at low temperatures", *Physical Chemistry Chemical Physics*, Vol. 3, No. 6, pp. 1123-1131, 2001.
145. Koper, M. T. M., "Electrocatalysis on bimetallic and alloy surfaces", *Surface Science*, Vol. 548, No. 1-3, pp. 1-3, 2004.
146. Zhang, C. J., R. J. Baxter, P. Hu, A. Alavi and M. H. Lee, "A density functional theory study of carbon monoxide oxidation on the Cu₃Pt(111) alloy surface: Comparison with the reactions on Pt(111) and Cu(111)", *Journal of Chemical Physics*, Vol. 115, No. 11, pp. 5272-5280, 2001.
147. Watwe, R. M., R. D. Cortright, M. Mavrikakis, J. K. Norskov and J. A. Dumesic, "Density functional theory studies of the adsorption of ethylene and oxygen on Pt(111) and Pt₃Sn(111)", *Journal of Chemical Physics*, Vol. 114, No. 10, pp. 4663-4671, 2001.

148. Schwegmann, S., H. Over, V. De Renzi and G. Ertl, "The atomic geometry of the O and CO + O phases on Rh(111)", *Surface Science*, Vol. 375, No. 1, pp. 91-106, 1997.
149. Jaworowski, A. J., A. Beutler, F. Strisland, R. Nyholm, B. Setlik, D. Heskett and J. N. Andersen, "Adsorption sites in O and CO coadsorption phases on Rh(111) investigated by high-resolution core-level photoemission", *Surface Science*, Vol. 431, No. 1-3, pp. 33-41, 1999
150. Krenn, G., "CO adsorption and CO and O coadsorption on Rh(111) studied by reflection absorption infrared spectroscopy and density functional theory", *Journal of Chemical Physics*, Vol. 124, No. 14, pp. 144703-144709, 2006.
151. Narloch, B., G. Held and D. Menzel, "Structural rearrangement by coadsorption: a LEED IV determination of the Ru(001)-p(2 × 2) (2O + CO) structure", *Surface Science*, Vol. 317, No. 1-2, pp. 131-142, 1994.
152. Stampfl, C. and M. Scheffler, "Energy barriers and chemical properties in the coadsorption of carbon monoxide and oxygen on Ru(0001)", *Physical Review B*, Vol. 65, No. 15, pp. 155417-155428, 2002.
153. Seitsonen, A. P., Y. D. Kim, S. Schwegmann, and H. Over, "Comprehensive characterization of the, (2×2)-O and the CO-induced overlayers on Pd(111)", *Surface Science*, Vol. 468, No. 1-3, pp. 176-186, 2000.
154. Bleakley, K. and P. Hu, "A Density Functional Theory Study of the Interaction between CO and O on a Pt Surface: CO/Pt(111), O/Pt(111), and CO/O/Pt(111)", *Journal of American Chemical Society*, Vol. 121, No.33, pp. 7644-7652, 1999.
155. Han, B. C. and G. Ceder, "Effect of coadsorption and Ru alloying on the adsorption of CO on Pt", *Physical Review B*, Vol. 74, pp. 205418-1 - 205418-8, 2006.
156. Dupont, C., Y. Jugnet, and D. Loffreda, "Theoretical Evidence of PtSn Alloy Efficiency for CO Oxidation", *Journal of American Chemical Society*, Vol. 128, pp. 9129-9136, 2006.

157. Lynch, M., P. Hu, "A density functional theory study of CO and atomic oxygen chemisorption on Pt(111)", *Surface Science*, Vol. 458, No. 1-3 pp. 1-14, 2000.
158. Yeo, Y. Y., L. Vattuone, D. A. King, "Calorimetric heats for CO and oxygen adsorption and for the catalytic CO oxidation reaction on Pt{111}", *Journal of Chemical Physics*, Vol. 106, No. 1, pp. 392-400, 1997.
159. Winkler, A., X. Guo, H. R. Siddiqui, P. L. Hagans and J. T. Yates Jr, "Kinetics and energetics of oxygen adsorption on Pt(111) and Pt(112)- A comparison of flat and stepped surfaces", *Surface Science*, Vol. 201, No. 3, pp. 419-443, 1988
160. Mortensen, K., C. Klink, F. Jensen, F. Besenbacher and I. Stensgaard, "Adsorption position of oxygen on the Pt(111) surface", *Surface Science Letters*, Vol. 220, No. 2-3, pp. L701-L708, 1989
161. Burnett, D. J., A. T. Capitano, A. M. Gabelnick, A. L. Marsh, D. A. Fischer and J. L. Gland, "In-situ soft X-ray studies of CO oxidation on the Pt(111) surface", *Surface Science*, Vol. 564, No. 1-3, pp. 29-37, 2004.
162. Zhang, C., P. Hu and A. Alavi, "A General Mechanism for CO Oxidation on Close-Packed Transition Metal Surfaces", *Journal of American Chemical Society*, Vol. 121, No. 34, pp. 7931-7932, 1999.